Alma Mater Studiorum – Università di Bologna

DOTTORATO DI RICERCA IN

CHIMICA

Ciclo 34

Settore Concorsuale: 03/B1 – FONDAMENTI DELLE SCIENZE CHIMICHE E SISTEMI INORGANICI

Settore Scientifico Disciplinare: CHIM/03 – CHIMICA GENERALE E INORGANICA

PHOTOPHYSICAL PROPERTIES OF SUPRAMOLECULAR ARRAYS BASED ON PORPHYRINS

Presentata da: Daniel Sánchez Resa

Coordinatore Dottorato

Prof. Domenica Tonelli

Supervisore

Dr. Barbara Ventura

Co-supervisori

Prof. Paola Ceroni

Esame finale anno 2022

Season 2, Episode 3, Minute 4:16.

Friends from college.

“Todos somos buenos y malos, mamá. Las dos cosas
a un tiempo. Lo que hay que desterrar es la hipocresía,
¿comprendes? Es preferible reconocerlo así que pasarnos
la vida inventándonos argumentos.”

Cinco horas con Mario, Miguel Delibes.

Index

Abstract

Supramolecular chemistry deals with molecular systems that enhance host-guest binding and can experience large and reversible changes in geometry, electronic or redox properties and in their photophysics upon chemical, redox or photonic stimuli. The great advantage of these systems is their easy functionalization that opens the way to design smart architectures with personalized properties depending on the desired application. A wide range of applications have been achieved thanks to the emerging synthesis of supramolecular systems like sensors devices, drug delivery systems, artificial molecular machines or functional supramolecular devices. Among all the building blocks available for designing new supramolecular architectures, porphyrins are highly attractive since this family of molecules is present in natural processes such as light harvesting, electron and energy transfer reactions, catalysis or as oxygen transporters. In addition, their aromatic core can be easily functionalized to tune their properties. Finally, they have very interesting photophysical and electrochemical properties.

In this PhD thesis, we aimed to characterize the photophysical properties of different supramolecular arrays based on porphyrins that have been prepared by Prof. Heitz's group (University of Strasbourg, France). This thesis is constituted by 5 different chapters that are detailed below:

Chapter 1 introduces the basic principles of photophysics, such as light absorption and emission from chromophores. Also, it discusses the nature of energy or electron transfer processes in supramolecular systems. In addition, a brief review on porphyrins and their applications is presented to highlight their importance in the design of new molecular cages or supramolecular arrays.

In Chapter 2, the photophysical properties of four flexible covalent cages composed by either two free-base porphyrins or one free-base porphyrin and one Zn(II)-metallated porphyrin decorated with triazole ligands, connected by flexible linkers (ethylenglycol (short) and diethylenglycol (long)), are detailed. The study revealed that the proximity of the two porphyrins within the structure provokes strong exciton interactions between the units, reflected in their absorption spectra. Besides, ultrafast luminescence measurements showed that the Zn-porphyrin fluorescence is quenched by a fast energy transfer that sensitizes the free-base emission in the Zn(II)-porphyrin containing cages.

In Chapter 3, the study of the complexation processes with Ag(I) of the four flexible covalent cages discussed in Chapter 2 is presented. The coordination of Ag(I) proved to

be a valid effector in opening the cavity of the cages, demonstrating their size-tunable capacity. The separation of the units in the opening process produced changes in absorption and emission spectra; it was thus possible to characterize spectroscopically the complexation event. The effective coordination of Ag(I) ions to the lateral triazole ligands occurred for all cages, except for the "long" cage composed by two free-base porphyrins. The unusual behavior of the long cage appears to be due to a metalation process of the porphyrin core that competes with Ag(I) complexation of the lateral triazole groups. Thanks to computational simulations, it has been proposed that the porphyrinic NH groups of this cage points towards the interior leaving exposed to the outside the reactive lone pair of the nitrogens enhancing its reactivity towards the binding of Ag(I). Furthermore, the ability of the short cages to function as hosts for the complexation of the ethionamide molecule was tested. The addition of ethionamide to the Ag(I)-complexes provoked an increase in the exciton coupling, probably due to the lower distance between the porphyrin planes induced by the complexation of ethionamide to the Ag(I) ions that leads to a more constricted conformation of the cages, accordingly to preliminary computational studies.

In Chapter 4, a new series of acridinium-porphyrin conjugates were studied. It was found that the acridinium units linked to the porphyrin behave as photoactive units that modify the properties of the arrays. Comparison of the absorption spectra of these arrays with those of their respective model compounds showed changes in the Soret band region. Theoretical calculations indicated that both porphyrin and acridinium centered transitions are responsible for these features. Concerning the emission properties, all arrays showed a strong fluorescence quenching of both the porphyrin and acridinium units, caused by an ultrafast photoinduced electron transfer process. Transient absorption analysis revealed that the formation of the charge separated state occurs in *ca*. 0.3 ps while its lifetime is *ca*. 1 ps.

Finally, Chapter 5 is dedicated to the description of the different photophysical techniques which were employed in the development of this PhD thesis: absorption and emission spectroscopy, gated sampling, streak camera measurements, time correlated single photon counting and ultrafast transient absorption spectroscopy.

Academic activities

Attendance to congresses and schools:

6th General Assembly & Annual Conference MSCAA, Vienna (Austria). Feb 2019. Poster presentation.

1st NOAH School, Tarragona (Spain). May 2019. Oral and poster presentations.

14th International Symposium on Macrocyclic and Supramolecular Chemistry, Lecce (Italy), Jun 2019. Poster presentation.

14th Italian Conference on Supramolecular Chemistry, Lecce (Italy), Jun 2019. Poster presentation.

UK-IT Joint Meeting on Photochemistry, Lipari (Italy). Jun 2019. Oral presentation.

Researchers' night, Bologna (Italy), Sept 2019. Oral presentation and activities.

2nd NOAH School, Bologna (Italy), Oct 2020. Oral and poster presentations.

1st SupraMat Conference, Spain, Feb 2021. Poster presentation.

"Il Linguaggio della Ricerca" outreach activity for schools, Istituto Ettore Majorana, Bologna (Italy), Mar 2021. Oral presentation and activities.

International Conference on Porphyrins and Phthalocyanines, Online event, June 2021. Poster presentation.

3rd NOAH School, Berlin (Germany), Sept 2021. Oral presentation.

Publications:

Daniel Sánchez-Resa, Laetitia Schoepff, Ryan Djemili, Stéphanie Durot, Valérie Heitz and Barbara Ventura: "Photophysical properties of porphyrinic covalent cages endowed with different linkers", *Journal of Porphyrins and Phthalocyanines*, **2019**, *23*, 841-849. DOI: 10.1142/S1088424619500925.

Amy Edo-Osagie, Daniel Sánchez-Resa, Dylan Serillon, Elisa Bandini, Christophe Gourlaouen, Henri-Pierre Jacquot de Rouville, Barbara Ventura and Valérie Heitz: "Synthesis, electronic and photophysical properties of a bisacridinium-Zn(II) porphyrin conjugate", *Compter Rendus Chimie*, **2021**, *24*, DOI: 10.5802/crchim.100.

Daniel Sánchez-Resa, Laura Zanettli-Polzi, Ryan Dejmili, Stéphanie Durot, Valérie Heitz, Isabella Dadione and Barbara Ventura: "Ag(I) complexation of porphyrinic covalent cages equipped with different flexible linkers". Under preparation.

Chapter 1: Introduction

1.1. Principles of photophysics

1.1.1. The nature of light

The interaction of light with matter, either in a natural or artificial way, crosses most branches of science.[1,2] Crucial processes such as photosynthesis depend on light: we can see thanks to a photochemical process occurring in our eyes, the technological world in areas like signal processing, storage, sensors and sensitizers are based on the interaction of light with matter and the generation of energy from solar power, an important resource nowadays, relies on photophysical and photochemical processes.[3,4]

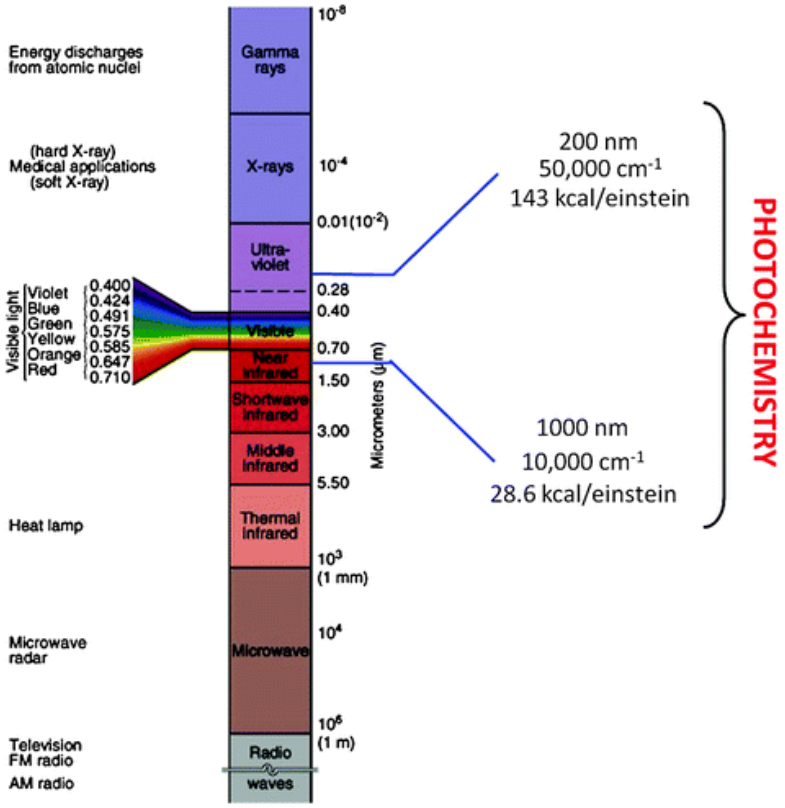

Figure 1.1. Electromagnetic spectrum, the region of interest for photochemistry is remarked. Reproduced with permission of © 2020 Springer Nature Switzerland AG.[5]

Light is understood as the electromagnetic radiation in the visible, near ultraviolet, and near infrared spectral range (Figure 1.1). In the wave model, the electromagnetic radiation is characterized by wavelength (λ), frequency (ν) and velocity (c). The c value is constant ($2.998 \cdot 10^8$ m·s^{-1} in vacuum), while the wavelength and the frequency cover a wide range of values, its relationship is defined by the following equation (1.1):

$$\lambda = \frac{c}{\nu} \tag{1.1}$$

The electromagnetic spectrum contains different types of radiation depending on their wavelength, the interesting range for photochemistry is comprised in the region from 200 to 1000 nm since the electronic transitions occurs within.

In the quantum model a stream of photons is considered a beam of radiation. The energy of the photon, *E*, related to the frequency of the radiation, *v*, is defined as described in equation (1.2):

$$E = h\nu \tag{1.2}$$

where *h* is Planck's constant ($6.63 \cdot 10^{-34}$ J·s).

When light interacts with a molecular system, an interaction between one molecule and one photon occurs (1.3):

$$A + h\nu \rightarrow {}^*A \tag{1.3}$$

where A represents the molecule in its ground state, h*v* the absorbed photon and *A the molecule in an electronically excited sate. The excited state must be considered as a new chemical species in comparison with the molecule in its ground state and can present different chemical and physical properties.

1.1.2. Potential energy surfaces[5]

Molecular systems present well-defined electronic states: ordinary chemistry is the one that deals with the ground electronic state whereas photochemistry is the chemistry of the electronic excited sates. This difference is based on the Born-Oppenheimer approximation that proposes the separation between the electronic and nuclear motions.[6] This approximation relies on the considerable difference in the masses of electrons and the nuclei. Considering the approximation, the electronic wavefunctions can be solved at fixed values of nuclear coordinates. For each geometry (*Q*) we can get a set of electronic wavefunctions ψ_k and energies E_k (where *k* is the electronic quantum number). For each *k*, the set of energy values obtained at different geometries defines a surface called the "adiabatic potential energy surface" of the k^{th} electronic state. This approximation is appliable when the electronic wavefunctions are slowly changing functions of the nuclear coordinates, nevertheless it is less valid if the electronic wavefunctions change drastically with nuclear motion.

Since a nonlinear N-atomic molecule has 3N-6 internal degrees of freedom, each electronic state is described by a potential hypersurface in a 3N-5 dimensional space. The

ground state hypersurface usually presents a deep minimum that belongs to the stable geometry of the molecule (Figure 1.2).

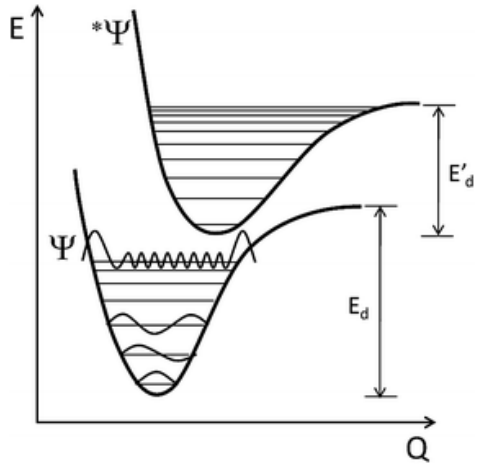

Figure 1.2. Potential energy curves for the ground (ψ) and the first excited state ($*\psi$). E_d and E'_d represent the corresponding dissociation energies. Reproduced with permission of © 2020 Springer Nature Switzerland AG.[5]

1.1.3. Electronic states and configurations[5]

Since molecules are multielectron systems, their approximate electronic wavefunctions can be set as products (which must be antisymmetrized) of one-electron wavefunctions where each one consists of an orbital and a spin part (1.4):

$$\psi_e = \phi S = \Pi_i \phi_i s_i \tag{1.4}$$

The ϕ_i are molecular orbitals (MO) and s_i is one of the two possible spin eigenfunctions, α or β. The orbital part of this multielectron wavefunction defines the electronic configuration.

1.1.4. Light absorption[5]

In order to promote a molecule from the ground electronic state to an electronically excited state, it is needed that the photon energy, hν, matches the energy gap between the ground and the excited state. In the case of common organic and inorganic molecules, this energy gap can be required in the visible and near ultraviolet regions. The probability of the transition when the energy gap is overcome, from the ground state ψ_i to the excited state ψ_f, is proportional to the square of the transition dipole moment M_{if} (1.5):

$$M_{if} = \langle \Psi_i | \mu | \Psi_f \rangle \tag{1.5}$$

where i and f stand for initial and final. μ is the electric dipole moment operator defined as $\sum e r_j$ with e representing the electron charge and r_j represents the position vector of the electron.

If the complete wavefunctions $\Psi = \Phi SX$, where Φ is the molecular orbital, S the spin eigenfunction and X the position vector of the electron, are substituted in equation (1.5), the transition moment splits into the product of three terms as shown in equation (1.6):

$$M_{if} = \langle \phi_i | \mu | \phi_f \rangle \langle S_i | S_f \rangle \sum_n \langle X_{i,0} | X_{f,n} \rangle \quad (1.6)$$

Taking into account the group theory,[7] the first term in equation (1.6) is annulled if the symmetry properties of the initial and final orbital functions are not appropriate (if the product $\phi_i \phi_f$ does not belong to the same irreducible representation of the point group of the molecule as μ). In these cases, the transition is *symmetry-forbidden* and it will appear with low intensity in the spectrum. The second term in (1.6) is expected to disappear due to the orthogonality of the spin wavefunctions when the initial and final states have different spin multiplicity, then the corresponding electronic transitions are denominated *spin-forbidden*. The last term is often called *Franck-Condon* term and can be discussed by considering that during electronic excitation the nuclear vibrational wavefunction remains nearly intact (*Franck-Condon principle*). If the change in equilibrium geometry upon excitation is small, the zero-zero transition between the two lowest vibrational levels of the two states is the most intense, and the others appear weak. If it is large, the zero-zero transition appears weak. In general, the peak of the absorption appears approximately at the energy of the so-called vertical transition, which corresponds to the difference between the energies of the initial and final states and the *Franck-Condon* term determines the shape of the absorption band.

1.1.5. Intramolecular excited state deactivation[5]

Vibrational relaxation

The light absorption can generate the excited state in a high vibrational level, and these vibrational excited molecules will tend to dissipate their excess vibrational energy (thermal) by interaction with surrounding molecules. This deactivation process is called vibrational relaxation.

Radiative deactivation

Electronically excited molecules can return to the ground state by emitting a quantum of light:

$$^*A \rightarrow A + h\nu' \quad (1.7)$$

This radiative transition is often known as spontaneous emission (not the same as stimulated emission). The same spin and symmetry selection rules discussed for

absorption are valid for the radiative deactivation. It is usual to refer to fluorescence when a spin-allowed emission ($S_1 \rightarrow S_0$ in organic molecules) takes place and phosphorescence when a spin forbidden emission ($T_1 \rightarrow S_0$ in organic molecules) occurs.

Radiationless deactivation

If the excited state is converted into the ground state (or lower excited state) without emission of radiation, a two-step mechanism operates:

i. Isoenergetic conversion of the electronic energy of an upper state into vibrational energy of the ground state (radiationless transition)
ii. Vibrational relaxation of the ground state.

The Jablonski's diagram of a generic organic molecule is illustrated in Figure 1.3. Experimental observations showed that internal conversion within each excited state of any given multiplicity ($S_n \rightarrow S_1$ and $T_n \rightarrow T_1$) is an ultrafast process (picosecond region). Intersystem crossing between the lowest excited states of any multiplicity ($S_1 \rightarrow T_1$) is in the range of sub-nanosecond to nanoseconds. Finally, radiationless deactivations from the lowest excited states of any multiplicity to the ground state are slower (nanoseconds to microseconds for $S_1 \rightarrow S_0$, and milliseconds to seconds for $T_1 \rightarrow S_0$). As detailed, radiationless decay of upper excited states to the lowest one of same multiplicity is very fast and that is why usually the emitting level of a given multiplicity is the lowest excited level of that multiplicity (Kasha's rule).[8]

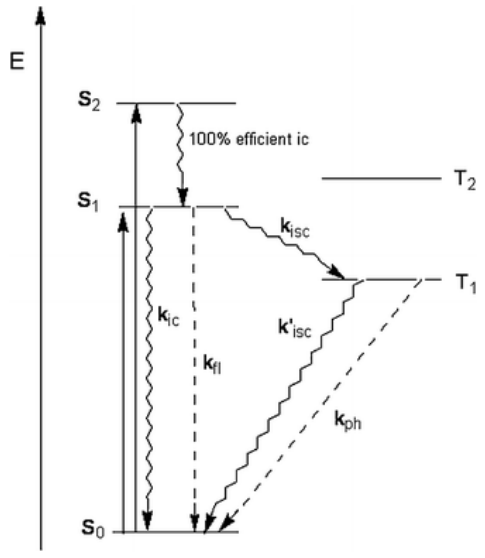

Figure 1.3. Schematic energy level diagram and deactivation processes for a generic organic molecule. Reproduced with permission of © 2020 Springer Nature Switzerland AG.[5]

Chemical Reaction

The processes described before are denominated photophysical processes since they do not provoke any chemical change in the light-absorbing molecule. But excited states can deactivate to the ground-state also by a variety of chemical processes.

Kinetic aspects

The three unimolecular processes: radiative deactivation, radiationless deactivation and intramolecular chemical reaction, compete for deactivation of any excited state of a molecule. Therefore, their rates are fundamental to determine the behavior of the excited state.

An excited state **A* will decay according to an overall first-order kinetics with a lifetime (τ(**A*)) given by (1.8):

$$\tau(\,^{*}A) = \frac{1}{k_r + k_{nr} + k_p} = \frac{1}{\Sigma_j k_j} \tag{1.8}$$

where k_r, k_{nr} and k_p are the rate constants of the three unimolecular processes: radiative or radiationless deactivation or chemical reaction, respectively. For each process of **A* deactivation, its efficiency η_i(**A*) can be defined as (1.9):

$$\eta_i(\,^{*}A) = \frac{k_i}{\Sigma_j k_j} = \; k_i \tau(\,^{*}A) \tag{1.9}$$

1.2. Supramolecular Photochemistry

Before stating what a supramolecular system is from the photophysical point of view, a definition of supramolecular chemistry should be presented:

In generally accepted terms, supramolecular chemistry deals with non-covalent interactions (hydrogen bonding, donor-acceptor, van der Waals…) between molecules that drive towards molecular recognition and self-assembly processes. Most non-covalent interactions are relatively weak and break with no need of activation barriers, then, most of supramolecular systems are under thermodynamic control. For a long time, supramolecular chemists focused on systems under thermodynamic control but recently kinetically controlled and far-from-equilibrium systems are being studied. We can define the different regimes as follows:

- Equilibrium assemblies: systems that persist thanks to their thermodynamic stability.
- Kinetically trapped assemblies: systems that are stable during a short time, trapped in a local minimum of the energy landscape. Time or activation energy are required to be converted into more stable structures.
- Far from equilibrium assemblies: these systems require a continuous supply of energy to persist.[9]

Considering these regimes, the self-organization that lead towards more complex systems can be:

- Passive. The self-assembled architecture has been created from components under thermal equilibrium conditions. It can be adaptive when external or internal stimuli/effectors take place.
- Active. It corresponds to the self-organization that is driven by time-dependent, non-equilibrium, dissipative physical and chemical processes. The system can adapt and evolve under non-equilibrium conditions.[10]

Ultimately, supramolecular chemistry explores molecular systems that enhance guest binding and can experience large and reversible geometrical, electronic, redox or luminescence modifications upon a chemical, redox or photonic stimulus. These systems should be easily functionalized, with the aim to produce functional devices that can act as sensors, drug delivery systems, artificial molecular machines, or functional supramolecular devices.[10–15] Supramolecular chemistry allows the synthesis of

functional structures that can present sizes near the nanoscopic dimensions. Nowadays, it is a mature field of science that frontiers with fields such as physics and biology. In conclusion, supramolecular chemistry has overcome the classical boundaries of science and represents a highly interesting field.[16]

1.2.1. Definition of a supramolecular system[17]

The difference between what is molecular and what supramolecular from a functional point of view can be determined from the degree of inter-component electronic interactions.[18] This concept can be illustrated as shown in Figure 1.4.

A – B represents a system of two units where "-" illustrates any type of bond that maintain the units together. This system can be affected by several stimuli, such as a photon, that can determine if it behaves as a supramolecular entity or as a large molecule. In the case of a photon stimulus, if light absorption leads to excited states that are localized in A or B or causes an energy or electron transfer from A to B, or vice versa, A-B can be considered a supramolecular structure.

In the case of an oxidation or reduction process, a supramolecular entity will undergo the oxidation or reduction of the specific units while these processes in a large molecule normally require that the hole or the electron are delocalized over the entire system.

In a general way, when the interaction energy between units is small compared to the other relevant energy parameters, the system can be considered as a supramolecular species, regardless of the nature of the bonds that link the units. The properties of each component of a supramolecular species can be known from the study of the isolated components or of suitable model compounds.

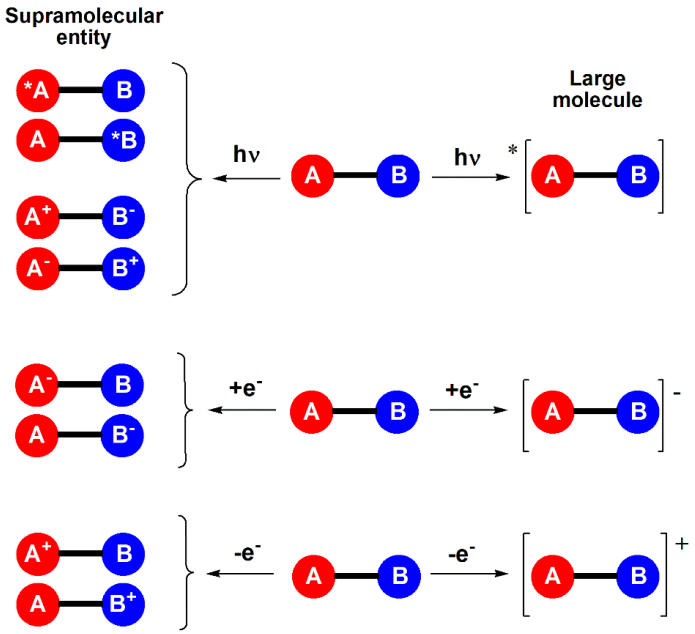

Figure 1.4. Schematic representation of the difference between a supramolecular system and a large molecule based on the effects caused by a photon or an electron input. Reproduced with permission of © 2020 Springer Nature Switzerland AG.[17]

1.2.2. Photoinduced energy and electron transfer in supramolecular systems[17]

If we consider an A-L-B type supramolecular system, where A is the light-absorbing molecular unit, B is the other molecular unit involved with A in the light induced processes and L is the connecting unit (bridge). In this type of system, electron and energy transfer can be described as follows:

$A – L – B + h\nu \rightarrow {}^*A – L – B$	Photoexcitation	(1.10)
${}^*A – L – B \rightarrow A^+ – L – B^-$	Oxidative Electron Transfer	(1.11)
${}^*A – L – B \rightarrow A^- – L – B^+$	Reductive Electron Transfer	(1.12)
${}^*A – L – B \rightarrow A – L – {}^*B$	Electronic Energy Transfer	(1.13)

Without chemical modifications, photoinduced electron transfer processes are followed by spontaneous back-electron transfer reactions that regenerate the starting ground state system. Similarly, photoinduced energy transfer is followed by radiative and/or non-radiative deactivation of the excited acceptor.

$A^+ – L – B^- \rightarrow A – L – B$	Back Oxidative Electron Transfer	(1.14)
$A^- – L – B^+ \rightarrow A – L – B$	Back Reductive Electron Transfer	(1.15)
$A – L – {}^*B \rightarrow A – L – B$	Excited State decay	(1.16)

1.2.3. Electron transfer processes[17]

Electron transfer processes involving excited states as well as those involving ground state molecules, kinetically, can be dealt within the frame of the Marcus Theory[19] and more novel models.[20]

Marcus Theory

The potential energy curves of an electron transfer reaction for the initial (*i*) and final (*f*) states of the system are represented by parabolic functions (Figure 1.5). The rate constant for an electron transfer reaction can be expressed as in (1.17):

$$k_{el} = \nu_n \kappa_{el} \exp\left(\frac{-\Delta G^{\neq}}{RT}\right) \tag{1.17}$$

where ν_n is the average nuclear frequency factor, κ_{el} is the electronic transmission coefficient, and $\Delta G^{\neq}$ is the free activation energy. This last term can be expressed by the Marcus quadratic relationship (1.18):

$$\Delta G^{\neq} = \frac{1}{4\lambda}(\Delta G^0 + \lambda)^2 \tag{1.18}$$

where ΔG^0 is the standard free energy change of the reaction and λ is the reorganization energy (Figure 1.5).

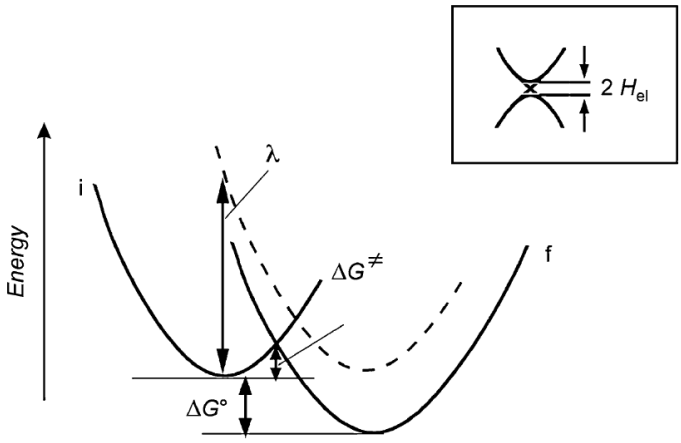

Figure 1.5. Profile of the potential energy curves of an electron transfer reaction: *i* and *f* indicate the initial and final states of the system. The dashed curve indicates the final state for a self-exchange (isoergonic) process. Reproduced with permission of © 2020 Springer Nature Switzerland AG.[17]

Equations (1.17) and (1.18) predict that for a homogeneous series of reactions a ln k_{el} versus ΔG^0 plot is a bell-shaped curve (Figure 1.6, solid line) involving:

- a normal regime for small driving forces ($-\lambda < \Delta G^0 < 0$) in which the process is thermally activated and ln k_{el} increases with increasing driving force

- an activationless regime (- $\lambda \approx \Delta G^0$) in which a change in the driving force does not cause large changes in the reaction rate
- an "inverted" regime for strongly exergonic processes (- $\lambda > \Delta G^0$) in which ln k_{el} *decreases* with increasing driving force.[18]

The reorganizational energy λ can be expressed as the sum of two independent contributions corresponding to the reorganization of the "inner" (λ_i, bond lengths and angles within the two reaction partners) and "outer" (λ_o solvent reorientation around the reacting pair) nuclear modes (1.19):

$$\lambda = \lambda_i + \lambda_o \tag{1.19}$$

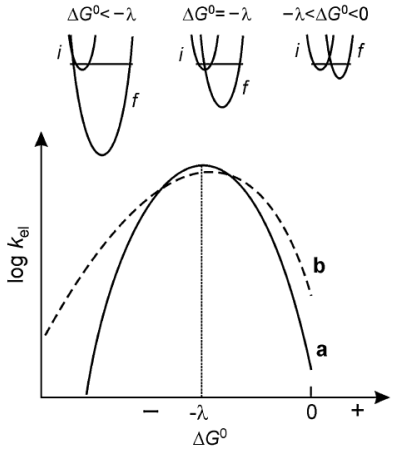

Figure 1.6. Free energy dependence of electron transfer rate (*i*, initial state; *f*, final state) according to Marcus (a) and quantum mechanical (b) treatments. The three kinetic regimes (normal, activationless, and "inverted") are shown schematically in terms of Marcus parabola). Reproduced with permission of © 2020 Springer Nature Switzerland AG.[17]

The outer-sphere reorganizational energy, which is often the predominant term in electron transfer processes, can be estimated, to a first approximation, by the expression (1.20):

$$\lambda_o = e^2\left(\frac{1}{\varepsilon_{op}} - \frac{1}{\varepsilon_s}\right)\left(\frac{1}{2r_A} + \frac{1}{2r_B} - \frac{1}{r_{AB}}\right) \tag{1.20}$$

where e is the electronic charge, ε_{op} and ε_s are the optical and static dielectric constants of the solvent, r_A and r_B are the radii of A and B and r_{AB} is the inter reactant center-to-center distance. Equation (1.20) shows that λ_0 is large for reactions in polar solvents between reaction partners which are separated by a large distance.

Quantum Mechanical Theory

The photoinduced and back-electron transfer processes can be considered as

radiationless transitions between different weakly interacting electronic states of the supramolecule A-L-B, from a quantum mechanical viewpoint. The rate constant is given by Fermi "golden rule" (1.21):

$$k_{el} = \frac{4\pi^2}{h}(H^{el})^2 FC^{el} \tag{1.21}$$

where the electronic H^{el} and nuclear FC^{el} factors are the electronic coupling term and the Franck-Condon density of states, respectively. In the absence of any intervening medium (through-space mechanism), the electronic factor decreases exponentially with increasing distance (1.22):

$$H^{el} = H^{el}(0)\exp[-\frac{\beta^{el}}{2}(r_{AB} - r_0)] \tag{1.22}$$

where r_{AB} is the donor-acceptor distance, $H^{el}(0)$ is the interaction at the "contact" distance r_0, and β^{el} is an appropriate attenuation parameter. The 1/2 factor arises because originally β^{el} was defined as the exponential attenuation parameter for rate constant rather than for electronic coupling (1.23):

$$k_{el} \propto \exp(-\beta^{el} r_{AB}) \tag{1.23}$$

For donor-acceptor components separated by vacuum, β^{el} is estimated to be in the range 2-5 $Å^{-1}$.

The FC^{el} term of equation (1.24) is a thermally average Franck-Condon factor connecting the initial and final states. It contains a sum of overlap integrals between the nuclear wave function of initial and final states of the same energy. The general expression of FC^{el} is complex and an approximation can be made when the temperature limit ($h\nu < k_B T$) is reached, this is valid for many room temperature processes. If we apply it, the nuclear factor takes the simple form:

$$FC^{el} = (\frac{1}{4\pi\lambda k_B T})^{1/2}\exp[-\frac{(\Delta G^0 + \lambda)^2}{4\pi\lambda k_B T}] \tag{1.24}$$

where λ is the sum of the inner (λ_i) and outer (λ_0) reorganizational energies. The exponential term of (1.24) is the same as the predicted by the classical Marcus model based on parabolic energy curves for the initial and final states. The quantum mechanical model contains the important prediction of three distinct kinetic regimes, depending on the driving force of the electron transfer process. The quantum mechanical model, however, predicts a practically linear decrease of ln k_{el} with increasing driving force in the inverted region (Figure 1.6, dashed line).

1.2.4. Energy transfer processes[17]

The thermodynamic ability of an excited state to intervene in energy transfer processes is related to its zero-zero spectroscopic energy, E^{00}. From a kinetic point of view, bimolecular energy transfer processes involving encounters can formally be treated using a Marcus type approach: equation (1.17) and (1.18). With $\Delta G^0 = E_A{}^{00} - E_B{}^{00}$ and $\lambda \sim \lambda_i$.[21]

The energy transfer process in supramolecular systems can be considered as a radiationless transition between two localized, electronic excites states. Hence, the rate constant can be obtained by a "golden rule" expression (1.25):

$$k_{en} = \frac{4\pi^2}{h}(H^{en})^2 FC^{en} \qquad (1.25)$$

where H^{en} is the electronic coupling between the two excited states inter-converted by the energy transfer process and FC^{en} is an appropriate Franck-Condon factor. In quantum mechanical terms, the *FC* factor is a thermally averaged sum of vibrational overlap integrals. Experimental information on this term can be obtained from the overlap integral between the emission spectrum of the donor and the absorption spectrum of the acceptor.

The electronic factor H^{en} is a two-electron matrix element involving the HOMO and LUMO of the energy-donor and energy-acceptor components. By following arguments,[20] this factor can be split into two additive terms, a *coulombic* term and an *exchange* term. The two terms depend differently on the parameters of the system (spin of ground and excited states, donor-acceptor distance). Because each of them can become predominant depending on the specific system and experimental conditions, two different mechanisms can occur, whose orbital aspects are schematically represented in Figure 1.7.

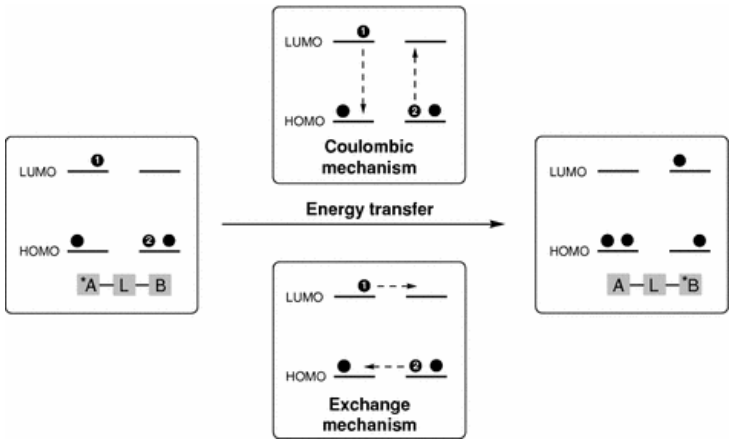

Figure 1.7. Pictorial representation of the coulombic and exchange energy transfer mechanisms. Reproduced with permission of © 2020 Springer Nature Switzerland AG.[17]

Coulombic Mechanism

The coulombic mechanism, also called Föster-type, is a long-range mechanism that does not require physical contact between donor and acceptor. It can be shown that the most important term within the coulombic interaction is the dipole-dipole term,[22,23] that obeys the same selection rules as the corresponding electric dipole transitions of the two partners (*A → A and B → *B, Figure 1.7).

Coulombic energy transfer is expected to be efficient in systems in which the radiative transitions connecting the ground and the excited state of each partner have high oscillator strength. The rate constant for the dipole-dipole coulombic energy transfer can be expressed as a function of the spectroscopic and photophysical properties of the two molecular components and their distance (1.26) and (1.27):

$$k_{en}^{F} = \frac{9000 \ln 10}{128\pi^5 N} \frac{K^2 \phi}{n^4 r_{AB}^6 \tau} J_F = 8.8\, x\, 10^{-25} \frac{K^2 \phi}{n^4 r_{AB}^6 \tau} J_F \qquad (1.26)$$

$$J_F = \frac{\int \frac{F(\bar{\nu})\varepsilon(\bar{\nu})}{\bar{\nu}^4} d\bar{\nu}}{\int F(\bar{\nu})\, d\bar{\nu}} \qquad (1.27)$$

where K is an orientation factor which takes into account the directional nature of the dipole-dipole interaction ($K^2 = 2/3$ for random orientation), Φ and τ are, respectively, the luminescence quantum yield and lifetime of the donor, n is the solvent refractive index, r_{AB} is the distance in Å between donor and acceptor, and J_F is the Förster overlap integral between the luminescence spectrum of the donor, $F(\bar{\nu})$, and the absorption spectrum of the acceptor, $\varepsilon(\bar{\nu})$, on an energy scale (cm^{-1}). With good spectral overlap integral and appropriate photophysical properties, the $1/r_{AB}^6$ distance dependence allows energy transfer to occur efficiently over distance that exceeds the molecular diameters. The typical example of an efficient coulombic mechanism is that of single-singlet energy transfer between large aromatic molecules, a process that takes place in nature in the antenna systems of the photosynthetic apparatus.

Exchange mechanism

The rate constant for the exchange (also called Dexter-type[24]) mechanism can be expressed by (1.28):

$$k_{en}^{D} = \frac{4\pi^2}{h} (H^{en})^2 J_D \qquad (1.28)$$

where the electronic term H^{en} is obtained from the electronic coupling between donor and acceptor, exponentially dependent on distance:

$$H^{en} = H^{en}(0) \exp\left[-\frac{\beta^{en}}{2}(r_{AB} - r_0)\right] \quad (1.29)$$

The nuclear factor J_D is the Dexter overlap integral between the emission spectrum of the donor and the absorption spectrum of the acceptor:

$$J_D = \frac{\int F(\bar{\nu})\varepsilon(\bar{\nu})d\bar{\nu}}{\int F(\bar{\nu})d\,\bar{\nu} \int \varepsilon(\bar{\nu})d\bar{\nu}} \quad (1.30)$$

The exchange interaction can be regarded (Figure 1.7) as a double electron process, one-electron moving from the LUMO of the excited donor to the LUMO of the acceptor, and the other from the acceptor HOMO to the donor HOMO. This important insight is illustrated in Figure 1.8, from which is clear that the attenuation factor β^{en} for exchange energy transfer should be approximately equal to the sum of the attenuation factors of two separated electron transfer processes, i.e. β^{el} for electron transfer between the LUMOs of the donor and acceptor (1.23), and β^{ht} for the electron transfer between the HOMOs (superscript ht for hole transfer from the donor to the acceptor).

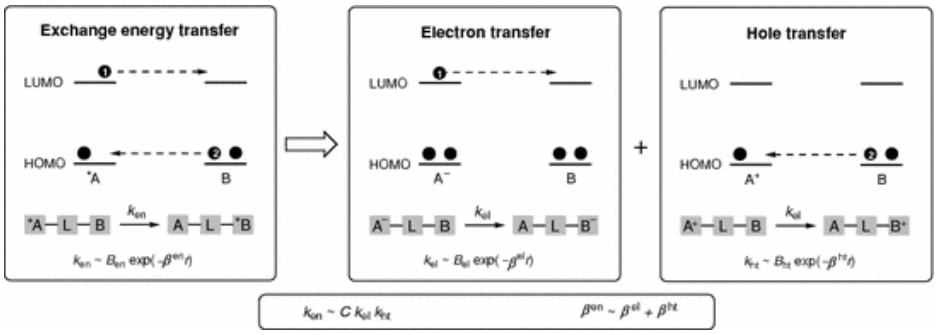

Figure 1.8. Analysis of the exchange energy transfer mechanism in terms of electron- and hole-transfer processes. The relationships between the rate constants and the attenuation factors of the three processes are also shown. Reproduced with permission of © 2020 Springer Nature Switzerland AG.[17]

The spin selection rules for this type of mechanism arise from the need to obey spin conservation in the reacting pair as a whole. This allows the exchange mechanism to be operative in many instances in which the excited states involved are spin forbidden in the usual spectroscopic sense. Thus, the typical example of an efficient exchange mechanism is that of triplet-triplet energy transfer (1.31):

$$^*A(T_1) – L – B(S_0) \rightarrow A(S_0) – L - {}^*B(T_1) \quad (1.31)$$

Although the exchange mechanism was originally formulated in terms of direct overlap between donor and acceptor orbitals, it can be extended to coupling mediated by an intervening medium (bridge).

1.2.5. The role of the bridge in supramolecular systems[17]

The connecting units (bridges) play an important role in mediation of electron- and energy transfer processes between donor and acceptor components in supramolecular structures.[18] Bridges can be "molecular wires" with "conducting properties". In the superexchange mechanism, the bridge levels are always higher in energy than those of donor and acceptor and the electron exchange in this case is mediated by the connecting bridge *via* an electron tunneling process (Figure 1.9).[25] Sometimes, the energy level of the bridge is so low that it becomes intermediate between the initial and final states. As a result, electron or energy hopping occurs and the bridge is directly involved in the process.

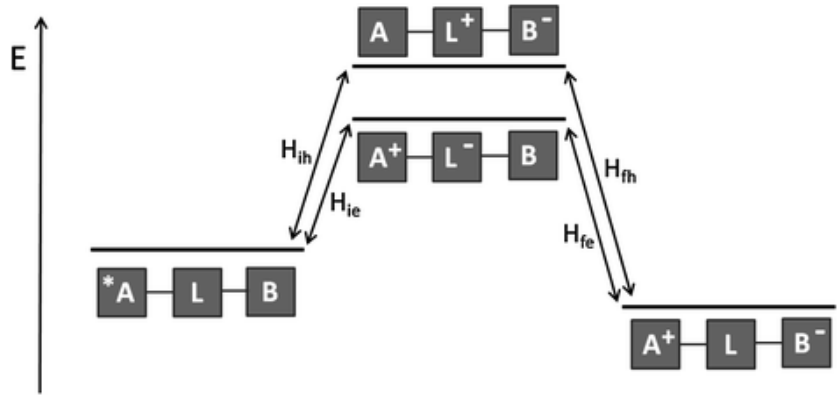

Figure 1.9. State diagram illustrating superexchange interaction between an excited state electron donor (*A) and an electron acceptor (B) through a bridge (L). Reproduced with permission of © 2020 Springer Nature Switzerland AG.[17]

When such a hopping-type mechanism is operative, very small distance dependence of the rate constant is expected.[18] If there is complete mixing among the donor/bridge/acceptor orbitals (large coupling limit) the bridge acts as an incoherent molecular wire and the system is expected to behave according to an ohmic regime where the rate varies inversely with bridge length.

1.3. Porphyrin derivatives

Porphyrins are aromatic macrocycles constituted by four pyrrole units connected through methine bridges. Their derivatives are dyes that abound in nature, integrated in biosystems where they take crucial roles for life in earth.[26] The photosynthetic antenna complex, that performs the light harvesting process, fundamental for our life on earth, is composed of porphyrin-derivative-associated protein arrays.[27,28] Several enzymes include porphyrin derivatives as prosthetic groups that constitute the catalytic center of the enzymatic reaction. For instance, an iron porphyrin derivative, hematoporphyrin, is part of the hemoglobin protein which reversibly binds oxygen molecules and allow their delivery into the tissues.[29]

The important roles that porphyrins play in nature comes from their functional versatility. Their expanded π-aromatic core enables light absorption in the visible region. Besides, they can act as host compounds that can form coordination complexes with various metal ions enabling new functionalities such as redox properties.[30–33] In addition, if the porphyrin core is metalated, it can coordinate ligands, which makes porphyrins ideal building blocks for supramolecular chemistry,[34,35] thanks also to their flat and symmetric molecular architectures.[36–39]

Taking into account all of these features, porphyrins can be useful in a number of applications, such as components of synthetic receptors, chromophores involved in the light harvesting process, units forming supramolecular assemblies or having biological activity.[26]

Regarding the optical properties of porphyrins, their intensity of absorption and color come from their conjugated π-electronic system that yields their characteristic UV-visible spectrum that is formed by two regions, one in the near ultraviolet and the other in the visible spectrum. The substituents that decorate these structures or their metalation can modify their UV/Vis absorption properties. The absorption bands in porphyrinic systems are due to transitions between two HOMOs and two LUMOs, hence, the metalation of the ring or the substituents affect the relative energies of these transitions. The HOMOs correspond to a_{1u} and a_{2u} orbitals, whereas the LUMOs are a degenerate set of e_g orbitals. Two states are split by orbital mixing, yielding a higher energy state with high oscillator strength that originates the Soret band, and a lower energy state with reduced oscillator strength that gives origin to the Q-bands.

The electronic absorption spectrum of a typical porphyrin is thus divided in two regions. The first one, provoked by the transition from the ground state to the second excited state ($S_0 \rightarrow S_2$), is characterized by a band called the Soret band. The range is comprised between 380-500 nm, depending on the type of substitution of the porphyrin (β or *meso*). The second region consists in a weak transition to the first excited state ($S_0 \rightarrow S_1$) in the range 500-750 nm (the Q-bands). These features are possible thanks to the conjugation of 18 π- electrons and enable the monitoring of guest-binding process by UV-visible spectroscopic methods.

The peripheral substituents of the porphyrin ring can vary in a minor way the intensity and wavelength of the absorption features, but the protonation of two of the inner nitrogen atoms or the insertion and/or change of metal atoms into the macrocycle normally change drastically the visible absorption spectrum. When it is the case, the protonated or metalated porphyrin adopts a more symmetrical situation than the free base which produces a simplification of the Q bands pattern with the formation of two Q bands.[40]

1.4. Porphyrins' applications

1.4.1. Host-guest systems for molecular recognition

Host-guest systems are of great interest in supramolecular chemistry. If we take a look into nature, chemical reactions in biosystems such as enzymes only occur when the substrates bind selectively to the molecular recognition sites. This kind of recognition process can be artificially mimed through the use of several building blocks such as calix[4]arenes[41] or crown ethers.[42] Porphyrins can be included in these types of receptors since they can yield coordination complexes with almost any metal ion and their aromatic skeleton induce the metal ions to adopt square planar coordination geometries that can be further stabilized by the axial coordination of ligands. Hence, porphyrin complexes can provide a stabilized building block for the construction of supramolecular receptors.[35] Moreover, the axial coordination of ligands varies the absorption properties of the porphyrins providing an easy way to follow the formation of the complex.[43]

In this context, Jang *et al*. have reported several examples of porphyrin-based receptors. In one example, a picket-fence-type triazole-bearing zinc porphyrin could strongly coordinate several anionic species through C-H hydrogen bonding and coordination interactions. The different affinities could be elucidated thanks to the variation in absorption spectra due to the mentioned axial coordination (Figure 1.10).[44]

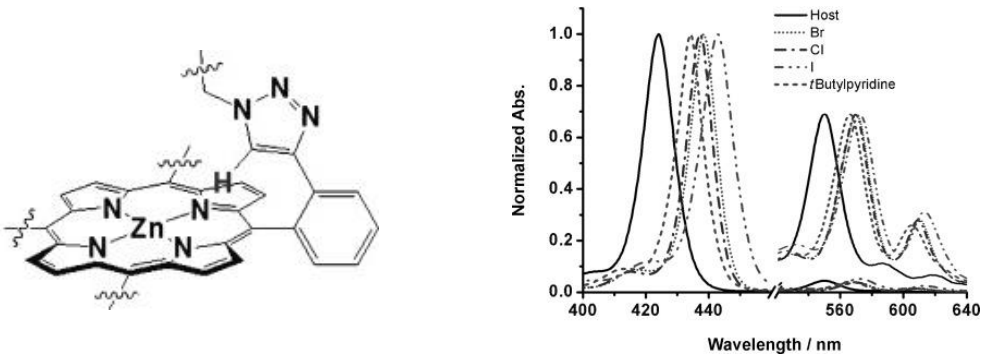

Figure 1.10. Structure of picket-fence-type triazole bearing zinc porphyrin and changes in absorption due to the coordination of anionic species. Reproduced with permission of © 1999-2921. John Wiley & Sons, Inc.[44]

The same group also reported a tweezer receptor for the DABCO molecule that could be linked thanks to an allosteric effect. It is composed of by two zinc porphyrins linked by a bis-indole spacer which has the capacity to link anions, such as chloride, to force a *cis* conformation by establishing bond interactions with the NHs of the indole and the CHs form the *meso*-phenyl substituents of the porphyrin units. The *cis* conformation induces a co-facial orientation of the two porphyrins, and this new orientation can link a

ditopic ligand such as DABCO (Figure 1.11).[45] In this example, we can appreciate how external stimuli can govern the receptor properties of supramolecular entities that have the capacity to act as guests.

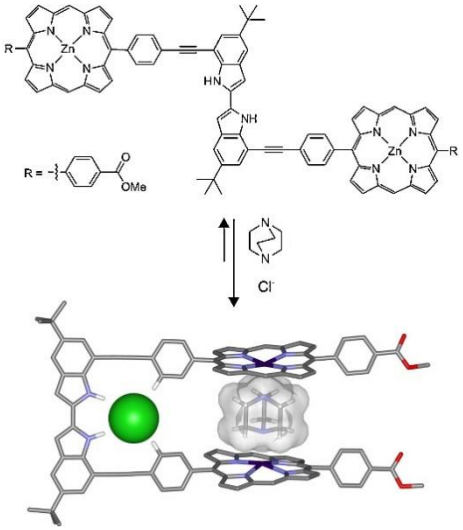

Figure 1.11. Allosteric bis-porphyrin receptor triggered by Cl^- for the DABCO molecule. Reproduced with permission of © 2013 Elsevier B.V.[45,46]

1.4.2. Light harvesting processes

Nature transforms light through photosynthesis to obtain the chemical energy required to maintain cell cycles. The photosynthesis process starts in the light-harvesting complexes located in chloroplasts in plant cells. These complexes contain porphyrin-based multichromophore arrays that efficiently absorb photons, perform vectorial energy transfer, charge separation and electron transfer.[47,48] These systems are highly attractive since their mimicry of natural systems can lead to efficiently capture light and its transformation into clean energy for industrial and human consumption in an eco-friendly manner. Some relevant examples are reported below.

Hunter *et al*. reported the self-assembly of a free-base porphyrin decorated with four pyridyl groups with two bis-zinc porphyrins, that coordinate through the bonding of the pyridine dicarboxylic amide groups with the Zn-metal centers. When the Zn-porphyrins were selectively excited, the free-base porphyrin emitted fluorescence. The rate of energy transfer, k_{ENT}, was $2 \cdot 10^9$ s^{-1} and an efficiency of 73% for the process was found (Figure 1.12).[49]

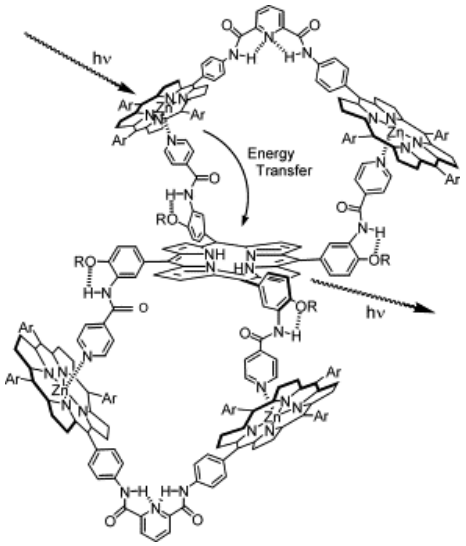

Figure 1.12. Energy transfer process in the self-assembly reported by Hunter *et al*. Reproduced with permission of © 1999-2921. John Wiley & Sons, Inc.[49]

Liu *et al*. synthesized a wirelike host-guest system formed by BODIPY (4,4-difluoro-4-bora-3a,4a-diaza-*s*-indacene) units that link two permethyl-*β*-cyclodextrins acting as host for a phenylsulfonated free-base porphyrin. Several energy transfer processes occurred in the complex with a high efficiency of 94%. This high yield can be explained by the perfect matching of the spectra between the BODIPY donor and porphyrin acceptor, the ideal separation between the two units mediated by the cyclodextrins, and the fact that the cyclodextrins hamper the *π*-*π* stacking of the donor-acceptor chromophores, hence, preventing charge-transfer reactions to occur. In addition, the wire-like system favored the energy transfer rather than the 1:1 complex (Figure 1.13). This example shows a non-covalent nanoarchitecture with highly effectiveness for light-harvesting applications.[50]

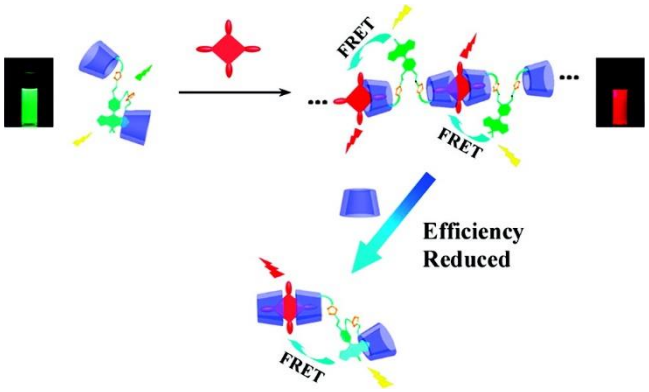

Figure 1.13. Fluorescence resonance energy transfer (FRET) in BODIPY-cyclodextrin conjugate and porphyrin host-guest system, both in 2:1 and 1:1 ratio. Reproduced with permission of © 2021 American Chemical Society.[50]

Jang *et al* prepared a porphyrin dendrimer (Figure 1.14) constituted by eight zinc porphyrin wings connected to a central free-base porphyrin that act as light energy collector. The excitation energy of the zinc porphyrin was successfully conveyed to the free-base porphyrin with a 94% excitation energy transfer efficiency.[51,52]

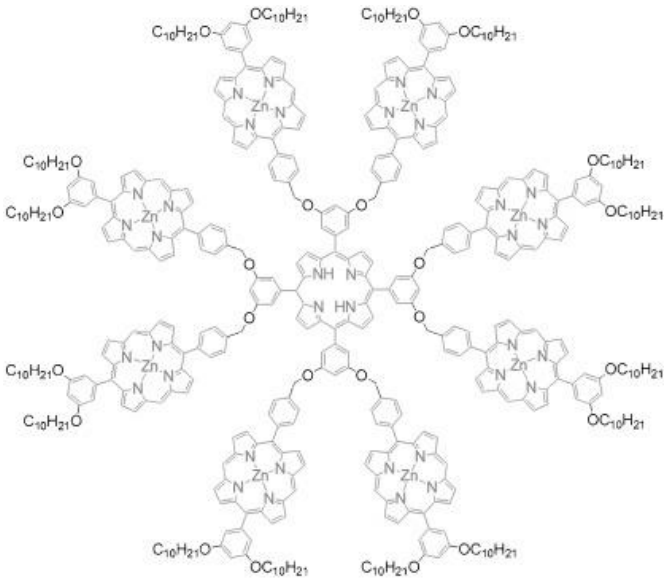

Figure 1.14. Porphyrin dendrimer employed in light harvesting by Jang *et al*. Reproduced with permission of © 1999-2921. John Wiley & Sons, Inc.[51]

1.4.3. Photovoltaics

Solar energy is a highly attractive renewable energy source due to its infinite supply, the light-to-current transformation can be carried out by a photovoltaic device.[53] The typical devices to transform this energy into electricity are based on silicon semiconductors that have high production costs and low flexibility.[54,55] Then, a new generation of solar cells have been developed capable of providing high energy conversion efficiency, ease of production and eco-friendly properties. In these new solar cells we can find DSSCs (dye-sensitized solar cells) and BHJ OSCs (bulk heterojunction organic solar cells).[33] Porphyrins, due to their photophysical and electrochemical properties, have been explored for their use in photovoltaics systems. [56,57] Below are two examples on this topic.

Zhu *et al*. prepared an acceptor-π-porphyrin-π-acceptor system with 2,5-dihexylthiophenylene π-linkage (Figure 1.15) that had the ability to undergo supramolecular self-assembly to form *J*-aggregates in the acceptor composite film of an Organic Solar cell. This assembly afforded a photovoltaic performance with high power conversion efficiency of 8.04%.[58]

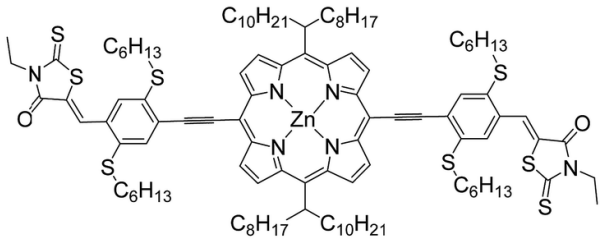

Figure 1.15. Acceptor-π-porphyrin-π-acceptor system synthesized by Zhu *et al*. Reproduced with permission of © The Royal Society of Chemistry 2018.[58]

Fukuzumi *et al*. synthesized clusters of porphyrin dendrimers (Figure 1.16) that acted as donors and fullerenes acting as acceptors assembled on SnO_2 electrodes. The resulting nanoclusters absorbed light over the entire spectrum of visible light. The photovoltaic system had high charge-separation efficiency between porphyrin radical cation and fullerene radical anion as well as the efficient hole and electron transport.[59]

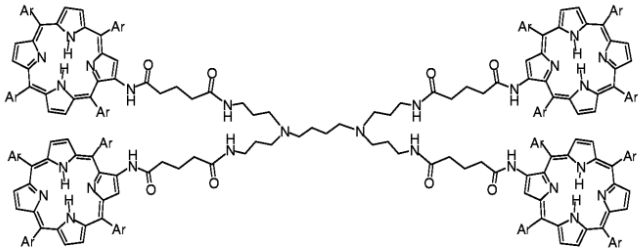

Figure 1.16. One example from Fukuzumi *et al*. on the preparation of porphyrin dendrimers for photovoltaic applications. Reproduced with permission of © 2021 American Chemical Society.[59]

1.4.4. Biomedical applications

Photodynamic therapy (PDT) is a promising cancer treatment due to its spatiotemporal specific controllability, non-invasiveness and high anticancer performance.[60,61] PDT involves the employment of oxygen, light and photosensitizers (PSs) that are activated by specific light at a suitable wavelength[62] and can generate cytotoxic reactive oxygen species (ROS) such as singlet oxygen or superoxide radicals that will cause tumor death.[63,64] In order to treat the tumors with this technique, the PS has to be accumulated in the tissue. Porphyrins have been used as conventional PSs, but they easily aggregate in aqueous media thanks to their π-π interactions and hydrophobic nature resulting in the self-quenching of the involved the excited states.[26] Therefore, some modifications must be made to avoid these problems, here some examples are presented:

Král *et al*. reported several multifunctional porphyrin building blocks linked with cyclodextrins that could offer two mechanisms for combined cancer treatment: drug delivery and PDT. The strategy used was to take advantage of the capability of cyclodextrins to encapsulate cytostatic agents such as doxorubicin and the ability of the porphyrins to act as photosensitizers (Figure 1.17).[65]

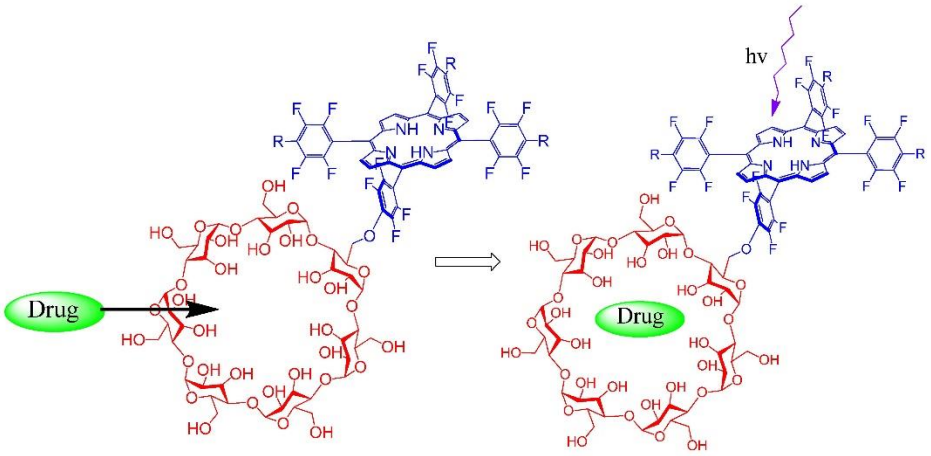

Figure 1.17. Combined chemotherapy and photodynamic therapy by cyclodextrin-porphyrin conjugate reported by Král *et al*. Reproduced with permission of © 1996-2021 MDPI.[66]

Kataoka *et al*. synthesized a dendrimer porphyrin where large poly(benzylether) dendrons were decorating a central porphyrin (Figure 1.18). The charged peripheral carboxylate groups made the system highly soluble in aqueous media. Besides, these peripheral groups could form micelles through electrostatic interactions that showed an excellent photodynamic efficacy in several models of animal diseases.[67]

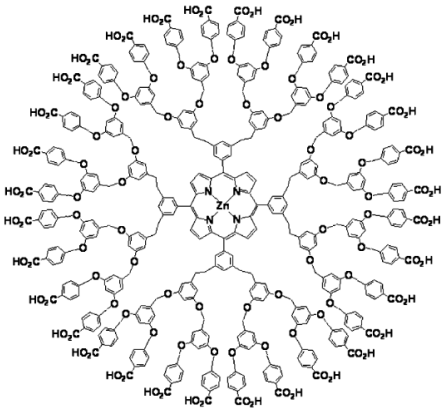

Figure 1.18. Dendrimer porphyrin employed in PDT by Jang *et al*. Reproduced with permission of © 2021 American Chemical Society.[67]

1.5. Conclusions

In summary, this brief review on the different applications of porphyrins in supramolecular chemistry aims to highlight their relevant role. Their suitability to be employed as building blocks in the construction of larger systems due to their aromaticity and geometry together with their ease to be decorated with different moieties that modulate their physico-chemical properties make porphyrins essential in the understanding and development of future supramolecular entities valid for a wide range of applications.

Chapter 2: Photophysical Properties of four Porphyrinic Covalently linked Cages equipped with different flexible linkers

2.1. Introduction

2.1.1. Porphyrinic Cages

The design of molecular cages as functional systems has received great interest in nanochemistry due to their capacity to work as nanoreactors, molecular recognition systems or drug carries, as they provide a three-dimensional confined environment that enhances molecular reactivity and catalysis.[16,68,69]

Among all the possibilities in the design of molecular cages, porphyrin derivatives and their metallated forms have caught the attention of many researchers since they are used in the mimicry of natural processes for light harvesting, electron and energy transfer reactions, catalysis, or as oxygen transporter as explained in Chapter 1. Besides, their stable aromatic core can be functionalized on *meso* or pyrrolic β positions and the inserted metal can modify their chemical, electronic and photophysical properties.[68]

Porphyrins have been used in lots of different molecular architectures for a variety of applications such as artificial photosynthesis,[70–91] catalysis,[92–102] therapy,[103–106] and surface engineering.[107–115] The inclusion of a porphyrin component in molecular cages that function as host systems provides several attractive opportunities: as a large structural element that delineates the molecular cavity; as an active component, since its large π-delocalized core can stabilize π-conjugated guest molecules inside the cavity, while its metallated form can coordinate various ligands within the cage; as a redox and photoactive component, it can participate directly into the reactivity performed inside the structure.[68]

The resemblance of porphyrins to natural chromophores[68,72,73,77,80,88,91,116–126] explains why they are used in artificial photosynthesis. The conversion of light into chemical energy that happens in this natural crucial process relies on efficient multistep energy transfer processes between natural chromophores closely related to porphyrins (chlorophyll or bacteriochlorophyll molecules) organized in antennas than convey the energy towards the reaction center where the first electron transfer step towards a free-base porphyrin analogous occurs.[28,127–133] The efficiency of this process is conditioned by the distance and mutual arrangement of these chromophores. Hence, light-responsive

cages are highly attractive due to their ability to perform and control energy transfer processes with the aim to mimic the natural process described.[72,121,124,134]

Several porphyrinic host-guest systems have been investigated by our group in the past years. As an example, in collaboration with Prof. Ballester and Prof. Hunter, it was reported the self-assembly of a cage based on trimeric Zn-porphyrin platforms by their coordination to bispyridyl functionalized perylene bisimide units that act as pillars through the coordination to Zn(II) ions fixing the planes of the porphyrins in a nearly co-facial orientation (prism-like structure). The fully assembled aggregate (2·porphyrin/3·ligands) and the partial one (2·porphyrins/2·ligands) were found to be in equilibrium in solution. The strong quenching observed in the mixture for the luminescence of both the ligands and the porphyrins was ascribed to an efficient photoinduced electron transfer from the Zn-porphyrins to the coordinated bisimides taking place upon excitation for both components within the assemblies.[135]

In the frame of the collaboration with Ballester's group, the study of two complexes formed by two cyclic Zn-bisporphyrins, differing in the saturation degree of the hydrocarbon linkers that connect their porphyrin units, and the fullerenes C_{60} and C_{70} was carried out (Figure 2.1). Absorption and fluorescence titration experiments revealed the formation of inclusion complexes stabilized by π-π interactions between the cyclic bisporphyrins and the fullerenes. Upon complexation, the cyclic bisporphyrins adopted distinct conformations. Charge-transfer absorption bands were observed, pointing to ground-state interactions, and quenching of the porphyrin component luminescence indicated fast reactivity in the excited states. Energy transfer and HOMO-HOMO and LUMO-LUMO electron transfer processes took place within the complexes. Charge-separated states characterized by a reduced fullerene and an oxidized porphyrin radical, with lifetimes in the order of several hundred picoseconds, were detected.[122]

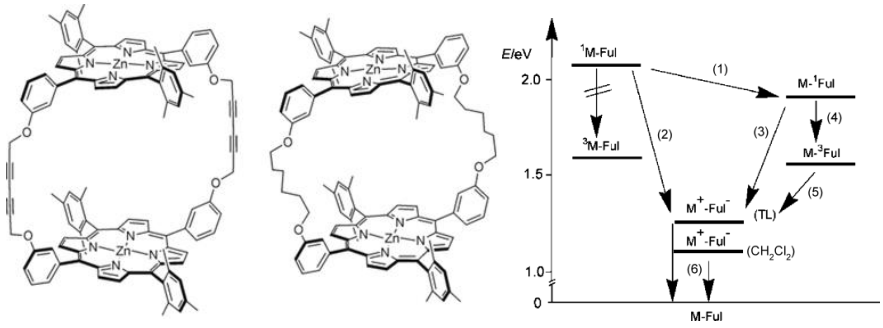

Figure 2.1. Bisporphyrin cages and energy level diagram for a generic supramolecular inclusion complex cage-fullerene. Reproduced with permission of ©1999-2021 John Wiley & Sons, Inc.[122]

In collaboration with the group of Prof. Heitz, several examples were reported regarding self-assembled and covalently linked porphyrinic systems.

The self-assembly of a gable-like Zn-bisporphyrin with a free-base porphyrin functionalized with pyridyl groups, that can coordinate to the Zn ions, was reported (Figure 2.2). The assembly displayed unusual photoinduced processes. Energy transfer occurred from the Zn-bisporphryin towards the pyridyl free-base porphyrin, but its fluorescence was quenched instead of enhanced. This was ascribed to a competing process depleting the excited state or to a perturbation of the tetrapyridil porphyrin engaged in the assembly. The formation of Zn-pyridine coordination bonds proved to be an efficient tool in the construction of large multicomponent assemblies.[136]

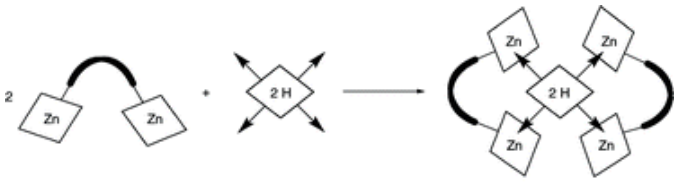

Figure 2.2. Visual representation of the self-assembly of a gable-like Zn-bisporphyrin with a free-base porphyrin decorated with four pyridyl groups. Reproduced with permission of © 2021 American Chemical Society.[136]

With further analysis on the assembly described in the previous paragraph, it was concluded that a HOMO-HOMO electron transfer process occurs from the zinc porphyrin towards the free-base upon excitation of the latter within the complex. Excitation of the Zn-porphyrin led predominantly to energy transfer to the free-base component, but also, parallel and less efficient LUMO-LUMO electron transfer. The unusual electron-transfer in this systems is possible by the easier oxidation of the Zn-porphyrin when coordinated with pyridyl residues and the more facile reduction of the tetrapyridyl free-base porphyrin with respect to the tetraaryl or dipyridyl homologue.[137]

In another study,[123] the formation of two coordination cages was achieved through the coordination of Ag(I) ions to the pyridyl moieties that decorate either two free-base or Zn-metallated porphyrins (Figure 2.3). It was concluded that the formation of the cages depends strongly on the stoichiometry between the porphyrins and the silver ions, through spectral changes observed by absorption and emission spectroscopy. The addition of two equivalents of silver(I) with respect to the porphyrin led to the formation of the cages whereas an excess of it, provoked side reactions that depended specifically on the nature of the porphyrin (free-base or Zn-metallated porphyrin). The free-base porphyrin underwent a metalation reaction, forming an [$Ag(I)_2$·porphyrin] complex, while the Zn-

metallated one experienced an oxidation process with the formation of a stable radical cation. These processes also took place in the reference compounds, porphyrins without pyridyl groups but containing triflate and methoxy groups. The common moieties among the cages and the references compounds where the *meso*-*ortho*-dimethylphenyl substituents, which should be responsible of such side reactions.[138]

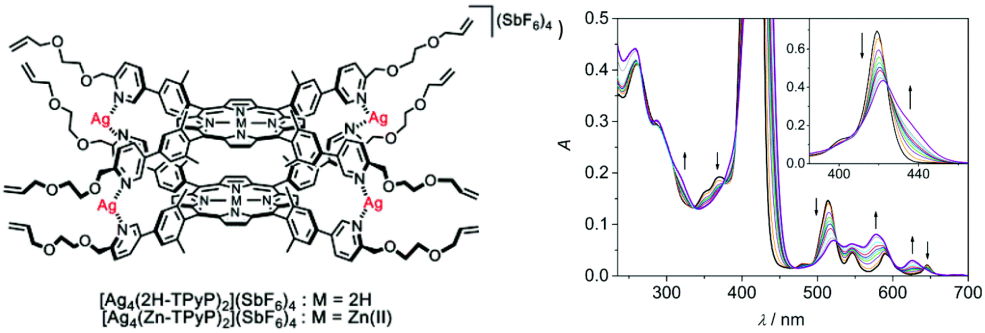

Figure 2.3. Chemical structure of the coordination cages based on 3-pyridyl appended porphyrins and Ag(I) ions (left) and absorption spectral changes of a solution of 2H-TPyP upon addition of excess of silver(I) (right). Reproduced with permission of © Royal Society of Chemistry 2021.[138]

Advancing in the study of the relationship between porphyrins and Ag(I) ions, Prof. Heitz's group synthesized two flexible covalent cages consisting of two Zn(II)-metallated porphyrins connected by linkers of different lengths incorporating two 1,2,3-triazolyl ligands,[139] with the objective to function as allosteric receptors. The reversible coordination/decoordination of Ag(I) triggers a large conformational change that opens the cavity and activates the receptor that can thus host two different guests: a pyrazine ligand and a π-acceptor NDI molecule (Figure 2.4). This work achieved the reversible *on/off* control of a guest inside the structure, which constitutes the basis to develop highly selective molecular sensors upon addition of a suitable effector.[140]

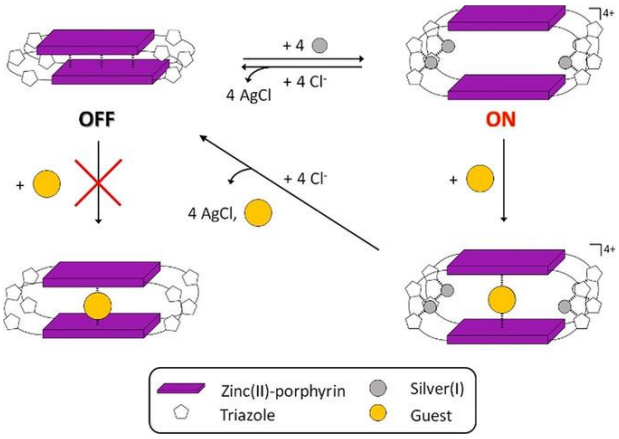

Figure 2.4. Schematic representation of the allosteric control of guest binding in flexible molecular cage receptors. Reproduced with permission of © 1999-2021 John Wiley & Sons, Inc.[140]

A spectroscopic and computational study of the Ag (I) complexation of the two covalent cages presented in the previous paragraph[140] was performed. The complexation process was followed by absorption and emission spectroscopy and a computational MD-PMM (Molecular Dynamics-Perturbed Matrix Method) analysis allowed to reproduce the features of the experimental Soret bands and to characterize the molecular interactions responsible for the changes in the absorption spectra. Upon Ag(I) complexation, it was observed that the spectral features and the intensity of the Soret band of both cages converged to those of the monomeric reference due to a reduction in the exciton coupling between the units. The reason is that the binding of Ag(I) ions opens the flattened structures and locks the two porphyrins in a face-to-face disposition (Figure 2.5).[141]

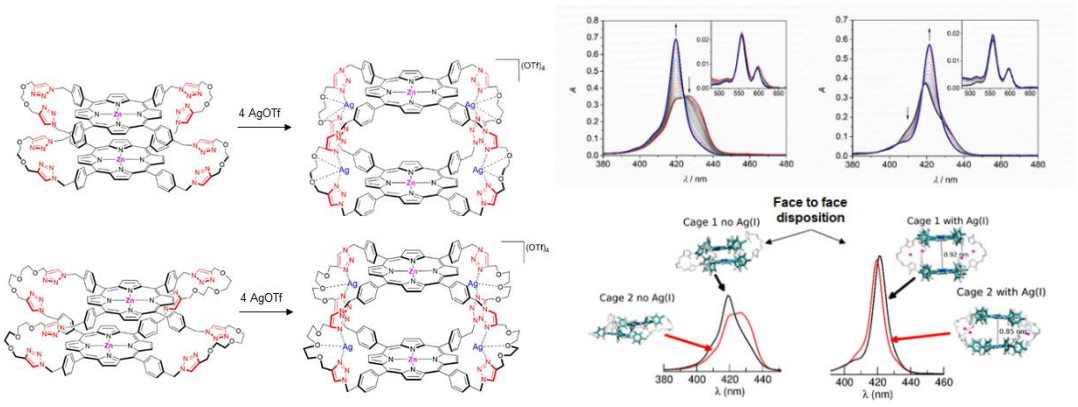

Figure 2.5. Representation of the opening process of bis-Zn-porphyrinic cages upon addition of Ag(I) (left). Experimental absorption titrations of the cages with Ag(I) and the computational modelling of the Soret band changes (right). Reproduced with permission of © 2021 American Chemical Society.[141]

In this chapter we report on the photophysical properties of four bis-porphyrinic cages constituted by either two free-base porphyrins or one Zn(II) porphyrin and one free-base porphyrin, connected by four flexible connectors that incorporate two 1,2,3-triazole ligands linked with either an ethyleneglycol unit or a diethyleneglycol unit. The ethyleneglycol units confer different lengths to the connectors, leading to different possible conformations of the systems. Hence, the four cages are different in terms of composition and lengths of the linkers. The study of the photophysical properties of these porphyrin cages is of importance regarding their potential as optical sensors or hosts for guest inclusion, as reported for similar systems.[135,142]

The photophysical investigation has been carried out by means of steady-state and time-resolved absorption and emission spectroscopies and the photoinduced processes

occurring within the porphyrin components were explained in relation to the porphyrin nature and the structural differences between the systems.

The study reported in this chapter was published in 2019: *"Photophysical properties of porphyrinic covalent cages endowed with different linkers",* D. Sánchez-Resa, L. Schoepff, R. Djemili, S. Durot, V. Heitz, B. Ventura, *Journal of Porphyrins and Phthalocyanines,* **2019**, *23*, 842-840.[142]

2.2. Results and discussion

The four porphyrinic cages are described as follows: two of them are composed by two free-base porphyrins and connected with either and ethylenglycol unit (*Short*: S) or diethyleneglycol unit (*Long*: L), these are named as **2H-S-2H** and **2H-L-2H**; the other two are composed by one Zn(II) porphyrin and one free-base porphyrin and the same connectors mentioned before, these are referred as **Zn-S-2H** and **Zn-L-2H** (Figure 2.6).

2.2.1. Synthesis

The synthesis of the cages has been carried out by Prof. Heitz's group.* The synthesis of the analogous cages formed by two free-base or two Zn(II) porphyrins connected with *short* linkers[139] and with *long* linkers[143] has been reported previously as well as that of the model compounds **2H-alkyne** and **Zn-alkyne** (Figure 2.6).[141]

Zn(II)-monometallated cages, **Zn-S-2H** and **Zn-L-2H**, were prepared from cages incorporating two free-base porphyrins following the procedure shown in Figure 2.6. They were reacted with 1.1 equivalents of $Zn(OAc)_2 \cdot 2H_2O$ in a mixture of $CHCl_3$/MeOH or CH_2Cl_2/MeOH.[139,143] From the mixture of the cages (Zn(II)-monometallated cages, Zn(II) dimetallated cage and bis(free-base porphyrin cage) obtained, the Zn(II) monometallated cages were isolated in 31% and 26% yield respectively, by preparative silica thin layer chromatography.

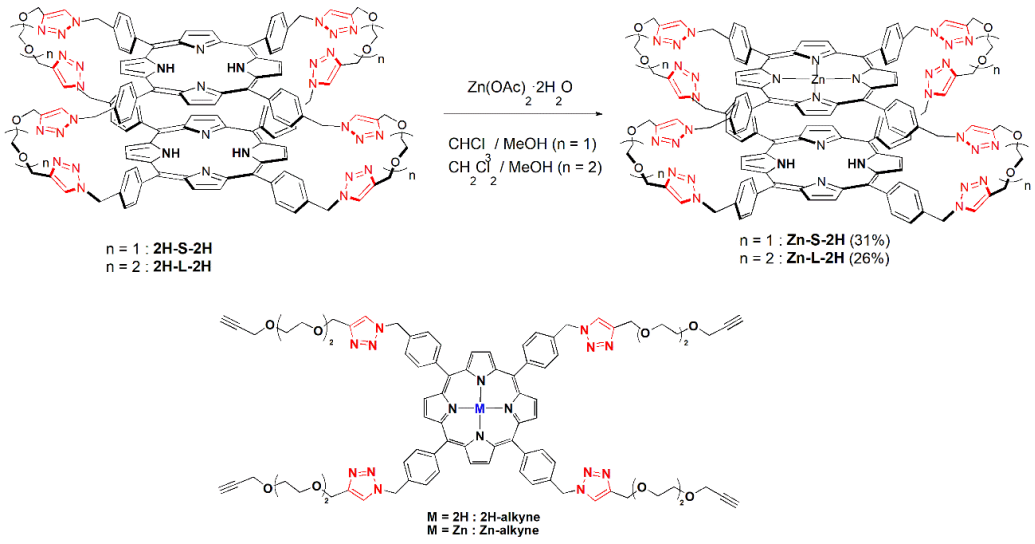

Figure 2.6. Synthesis of Zn(II)-monometallated porphyrin cages **Zn-S-2H** and **Zn-L-2H** from the parent free-base porphyrin cages **2H-S-2H** and **2H-L-2H** and structure of the models (**2H-alkyne**, **Zn-alkyne**).[142]

2.2.2. Photophysical Characterization

The photophysical features of the four cages and the models (**2H-alkyne**, **Zn-alkyne**), studied for comparison purposes, were analyzed in CH_2Cl_2/MeOH (9:1).

Absorption properties:

The cages formed by two free-base porphyrins, **2H-S-2H** and **2H-L-2H**, present similar absorption spectra, where the Soret band is slightly split and broadened compared with the sum of two spectra of the monomeric model **2H-alkyne** (Figure 2.7 and Figure 2.8 for the spectrum of the model). This split can be due to exciton coupling within the porphyrin units which are placed in close proximity in the cages, also observed before for the corresponding bis Zn(II)-porphyrin cages.[141] The different lengths of the linkers slightly affect the absorption spectra of the cages, the integrated molar absorption coefficients are similar for the two cages ($1.18 \cdot 10^9$ $M^{-1} \cdot cm^{-2}$ and $1.17 \cdot 10^9$ $M^{-1} \cdot cm^{-2}$ for **2H-S-2H** and **2H-L-2H**, respectively) and close to twice the integrated absorption coefficient of the monomer **2H-alkyne** ($4.02 \cdot 10^8$ $M^{-1} \cdot cm^{-2}$).

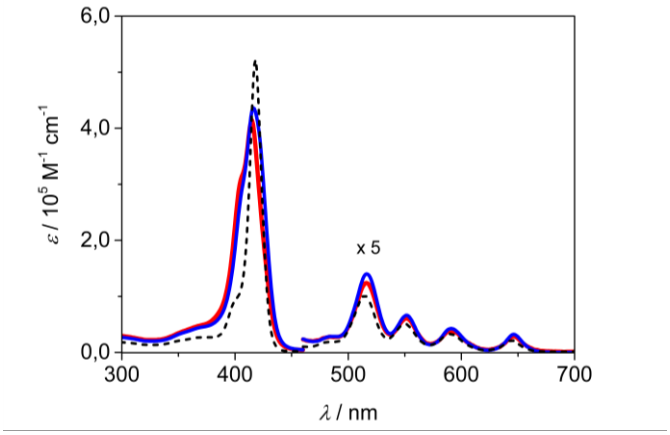

Figure 2.7. Absorption spectra of **2H-S-2H** (red), **2H-L-2H** (blue) and twice the absorption spectrum of **2H-alkyne** (black dashed) in CH_2Cl_2/MeOH (9:1). Absorption in the 460-700 nm region is amplified by a factor of five.[142]

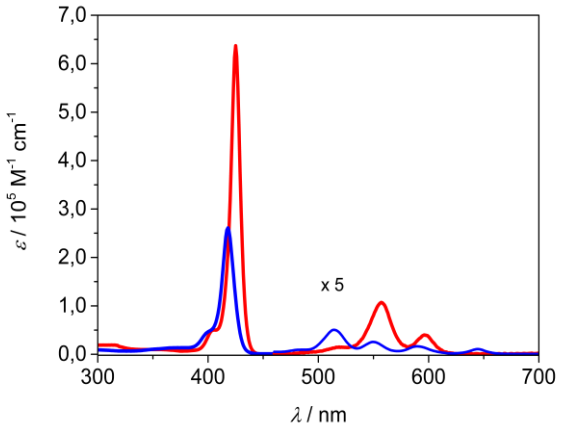

Figure 2.8. Absorption spectra of **2H-alkyne** (blue) and **Zn-alkyne** (red) in CH_2Cl_2/MeOH (9:1). Absorption in the 460-700 nm region is amplified by a factor of five.[142]

The analogous Zn(II)-monometallated cages, **Zn-S-2H** and **Zn-L-2H**, present absorption spectra which are shown in Figure 2.9 compared to the sum of the absorption spectra of models **2H-alkyne** and **Zn-alkyne**. The Soret bands of the cages evidence inter-porphyrinic interactions, with a more pronounced exciton coupling in the cage with longer linkers, **Zn-L-2H**. These features agree with a more slipped displacement of the porphyrins in **Zn-L-2H** with respect to a cofacial disposition favored in the cage with shorter and more rigid linkers, **Zn-S-2H**. These features related to molecular geometry were already observed with their analogous compounds, composed by two Zn(II)-metallated porphyrins.[141] Integrated molar absorption coefficients of $1.32 \cdot 10^9$ $M^{-1} \cdot cm^{-2}$ and $1.29 \cdot 10^9$ $M^{-1} \cdot cm^{-2}$ were calculated for **Zn-S-2H** and **Zn-L-2H**, respectively, which are similar to the sum of the integrated coefficients for **2H-alkyne** and **Zn-alkyne** ($1.06 \cdot 10^9$ $M^{-1} \cdot cm^{-2}$).

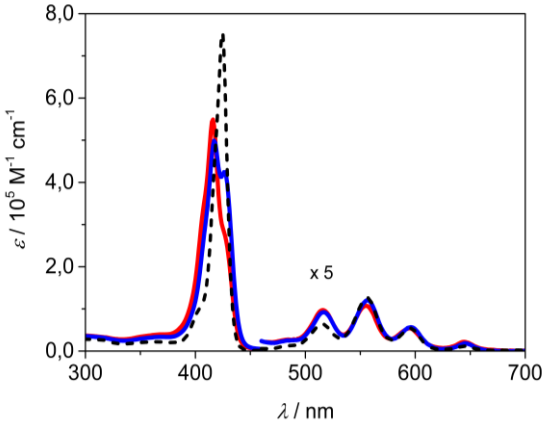

Figure 2.9. Absorption spectra of **Zn-S-2H** (red), **Zn-L-2H** (blue) and the sum of the absorption spectra of **2H-alkyne** and **Zn-alkyne** (black dashed) in CH_2Cl_2/MeOH (9:1). Absorption in the 460-700 nm region is amplified by a factor of five.[142]

To gain insights about the coupling interactions, the spectra of the monometallated cages were compared to the sum of half the spectra of the cages containing two identical porphyrins (bis free-base: **2H-S-2H** and **2H-L-2H**, presented in this chapter and dimetallated Zn(II) cages: **Zn-S-Zn** and **Zn-L-Zn**, from previous work).[141] Figure 2.10 shows the comparison for **Zn-S-2H** and **Zn-L-2H** with the sum of the respective free-base and Zn "half cages". The sum overlaps with a good approximation to the experimental spectrum of the monometallated cage in both cases, even in the Soret band region which is more affected by interporphyrinic exciton coupling. These data allow us to consider that the "homo" cages are better models, from a photophysical point of view, for the monometallated cages than the monomeric units **2H-alkyne** and **Zn-alkyne**, due to the strong interactions experienced by the porphyrins within these cages.

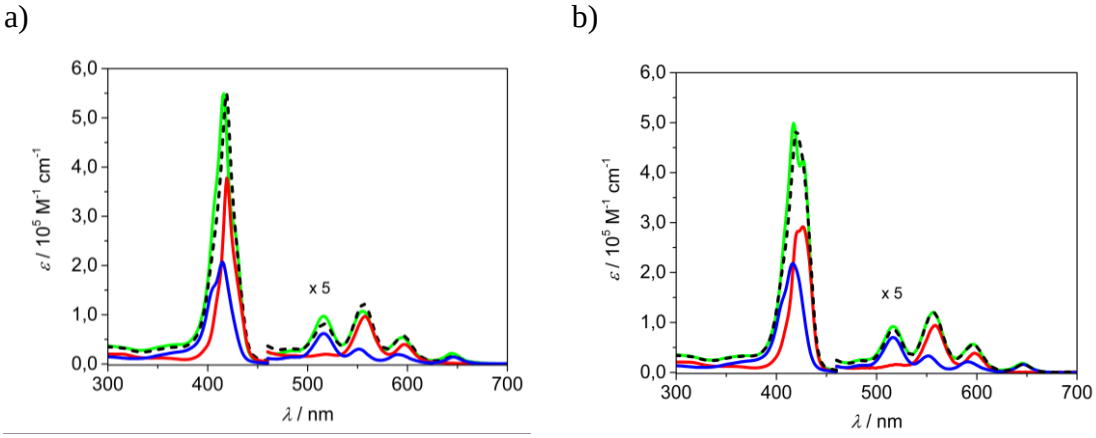

Figure 2.10. Absorption spectra of a) **Zn-S-2H** (green) and the sum (black dashed) of half the spectrum of **2H-S-2H** (blue) and half the spectrum of **Zn-S-Zn** (red); b) **Zn-L-2H** (green) and the sum (black dashed) of half the spectrum of **2H-L-2H** (blue) and half the spectrum of **Zn-L-Zn** (red); in CH_2Cl_2/MeOH (9:1). Absorption in the 460-700 nm region is amplified by a factor of five.[142]

Luminescence properties:

Luminescence measurements were carried out both at room temperature in CH_2Cl_2/MeOH (9:1) and at 77 K in a frozen CH_2Cl_2/MeOH (1:1) matrix.

Free-base porphyrins cages, **2H-S-2H** and **2H-L-2H**, display emission features resembling those of the respective model **2H-alkyne**, with maxima at 652 and 718 nm, fluorescence quantum yields close to 0.080 and excited state lifetimes on the order of 9.0 ns at room temperature (Figure 2.11, Table 2.1), indicating that the conformation of the cages does not affect the emission properties of the free-base porphyrin components. On the contrary, the selective excitation of the free-base component at 630 nm in the monometallated cages **Zn-S-2H** and **Zn-L-2H** lead to lower quantum yields of 0.047 and 0.068 respectively (Table 2.1), which is correlated with reduced lifetimes of 6.7 and 7.6

ns, respectively. This indicates that the Zn-porphyrin counterpart present in these cages perturbs the emission properties of the free-base component. This can be explained due to the close proximity of the Zn-center of the metallated porphyrin to the core of the free-base partner that can lead to a change in molecular symmetry or to an increased intersystem crossing rate in the latter.[141,144,145]

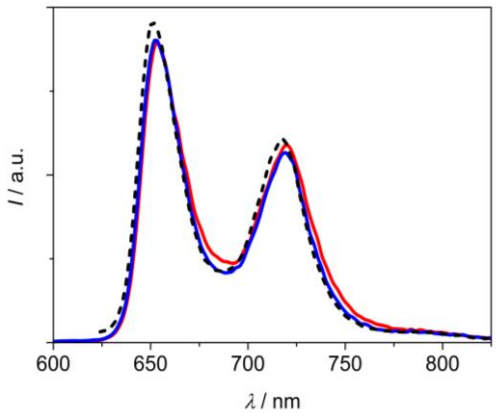

Figure 2.11. Corrected emission spectra at room temperature of **2H-S-2H** (red), **2H-L-2H** (blue) and **2H-alkyne** (black dashed) in CH_2Cl_2/MeOH (9:1). The spectral areas are proportional to the emission quantum yields. λ_{exc} = 550 nm.[142]

To demonstrate that the quenching observed in the free-base porphyrin within the **Zn-S-2H** cage was provoked by proximity of the Zn-porphyrin counterpart in the monometallated cages, an equimolecular mixture of the models **2H-alkyne** and **Zn-alkyne** was analyzed. Figure 2.12 displays absorption and emission spectra of the mixture in comparison to the sum of the spectra of the single compounds. The emission spectrum of the mixture matches the sum of the spectra of the models (Figure 2.12b), confirming that there is no interaction between them in solution.[1] Furthermore, the emission of **2H-alkyne** yielded a lifetime of 8.6 ns at 720 nm in the mixture, identical to the one of the model alone (Table 2.1).

[1] The emission contribution from the model **Zn-alkyne** in the mixture upon excitation at 630 nm is not negligible at the concentration used, which is optimized for the free-base porphyrin excitation.

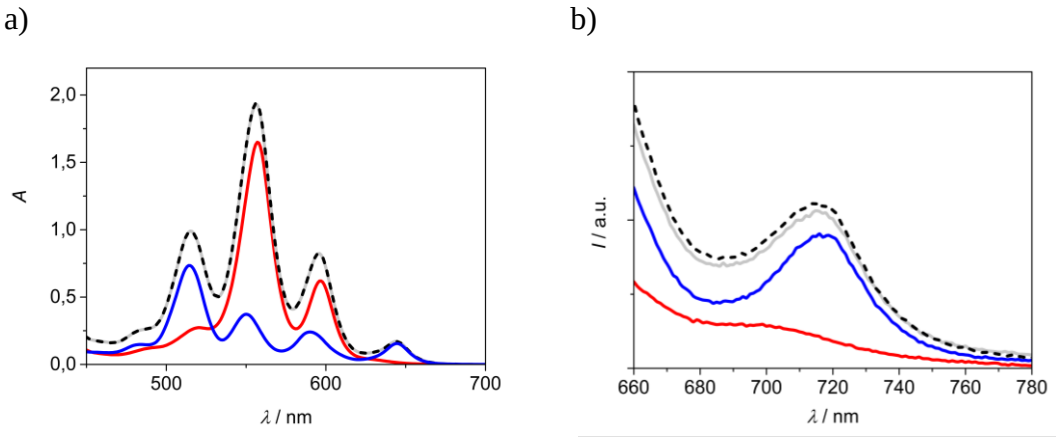

Figure 2.12. a) Absorption spectra of an equimolecular mixture of **2H-alkyne** and **Zn-alkyne** in CH_2Cl_2/MeOH (9:1) (grey, [**2H-alkyne**] = [**Zn-alkyne**] = $7.5 \cdot 10^{-5}$ M) and of solutions of the single compounds at the same concentration (blue: **2H-alkyne**, red: **Zn-alkyne**). The sum of the spectra of the single compounds is reported for comparisons purpose (black dashed). b) Corrected emission spectra obtained from the solutions in a) upon excitation at 630 nm (same color code).[142]

Excitation of both Zn(II)- and free-base porphyrin components led to observation of luminescence dominated by the bands of the free-base unit, while the Zn-porphyrin emission only appears as a weak band at *ca.* 608 nm, indicating a strong quenching of the Zn-porphyrin component in both cages (Table 2.1, Figure 2.13). To assess the extent of this quenching, the emission of **Zn-S-2H** and **Zn-L-2H** has been compared to that of optically matched solutions of the model cages with two free-base units or two Zn-porphyrins, and the results are shown in Figure 2.13. The excitation wavelength was selected according to the absorption comparison previously described (Figure 2.10), pointing to a major excitation of the Zn-porphyrin component in the monometallated cages (from 60% to 80% of the absorbed photons). Considering the portion of absorption of the Zn-porphyrin unit in each cage in solution and comparing the intensity of the residual Zn-porphyrin emission at 608 nm with the intensity at the same wavelength of the bis Zn-porphyrin model, it follows that the Zn-porphyrins components are quenched by over 90% in **Zn-S-2H** and **Zn-L-2H**. This strong quenching can be due to an energy transfer process from the Zn-metallated unit to the free-base porphyrin. Indeed, it is accompanied by a full recovery of the free-base porphyrin emission (Figure 2.13): the bands at 652 and 718 nm recover to *ca*. 65% and 80% those of the free-base porphyrin model for **2H-S-2H** and **Zn-S-Zn**, respectively, mirroring the ratios between the quantum yield of the free-base porphyrin unit in the monometallated cages and that of the same unit in the models (Table 2.1).

Table 2.1. Luminescence data at room temperature and 77 K, in CH_2Cl_2/MeOH (9:1) and (1:1), respectively.[142]

		RT			77 K		
		λ_{max}/nm[a]	ϕ_{fl}[b]	τ/ns[c]	λ_{max}/nm[a]	τ/ns[c]	E/eV
2H-alkyne	^{1}2H	652, 718	0.083	8.5	648, 716	11.4	1.91
Zn-alkyne [f]	^{1}Zn	606, 658	0.040	1.7	599, 656	2.1	2.07
	^{3}Zn				782	$19.2\cdot10^6$	1.59
2H-S-2H	^{1}2H-2H	654, 720	0.078	9.0	648, 716	12.8	1.91
2H-L-2H	^{1}2H-2H	652, 719	0.082	9.0	647, 715	11.5	1.92
Zn-S-2H	Zn-^{1}2H	652, 717	0.047[d]	6.7	645, 713	11.5	1.92
	^{1}Zn-2H	606, —	—	0.010[e]	601, —	—	2.06
	^{3}Zn-2H				788	$15.0\cdot10^6$	1.57
Zn-L-2H	Zn-^{1}2H	652, 718	0.068[d]	7.6	644, 712	11.2	1.93
	^{1}Zn-2H	608, —	—	0.007[e]	602, —	—	2.06
	^{3}Zn-2H				787	$17.9\cdot10^6$	1.58

[a]From corrected emission spectra. [b]Fluorescence quantum yields, measured with reference to **TPP** (*meso*-tetraphenylpophyrin) in aerated toluene as a standard. [c]Fluorescence and phosphorescence lifetimes, excitation at 465 nm and 420 nm, respectively. [d]Upon selective excitation of the free-base component at 630 nm. [e]Fluorescence lifetimes measured with a streak camera apparatus (time resolution: 1 ps), excitation at 560 nm. [f] From reference[141].

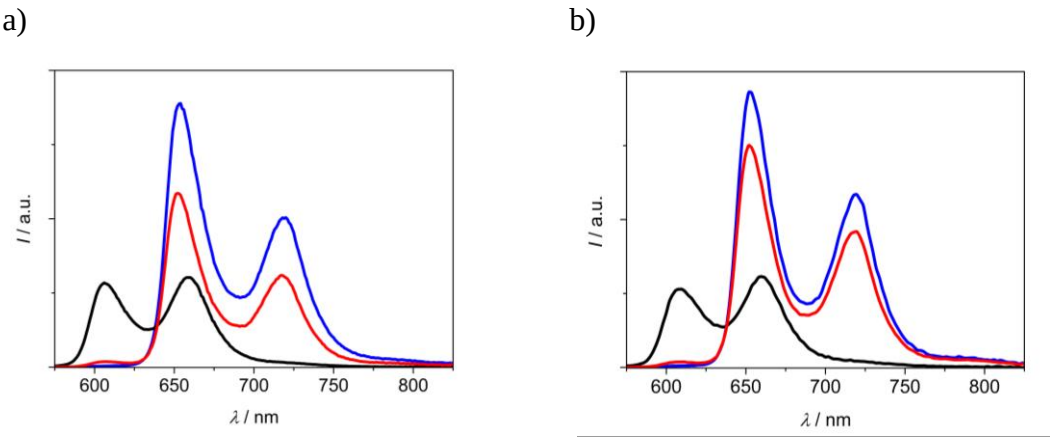

Figure 2.13. Corrected emission spectra at room temperature of iso-absorbing solutions of (a) **Zn-S-2H** (red) and models **2H-S-2H** (blue) and **Zn-S-Zn** (black), excitation at 557 nm (80% of the photons absorbed by the Zn unit in **Zn-S-2H**), A_{557} = 0.067; (b) **Zn-L-2H** (red) and models **2H-L-2H** (blue) and **Zn-L-Zn** (black), excitation at 537 nm (60% of the photons absorbed by the Zn unit in Zn-L-2H), A_{537} = 0.046; in CH_2Cl_2/MeOH (9:1).[142]

Another evidence of an almost complete Zn→2H energy transfer process comes from the good superimposition of excitation spectra, collected for both **Zn-S-2H** and **Zn-L-2H**

at 720 nm where only the free-base porphyrin unit emits, and absorption spectra (Figure 2.14d and e), indicating that whatever is the excited unit, the energy is conveyed to the lowest singlet excited state of the free-base porphyrin component.

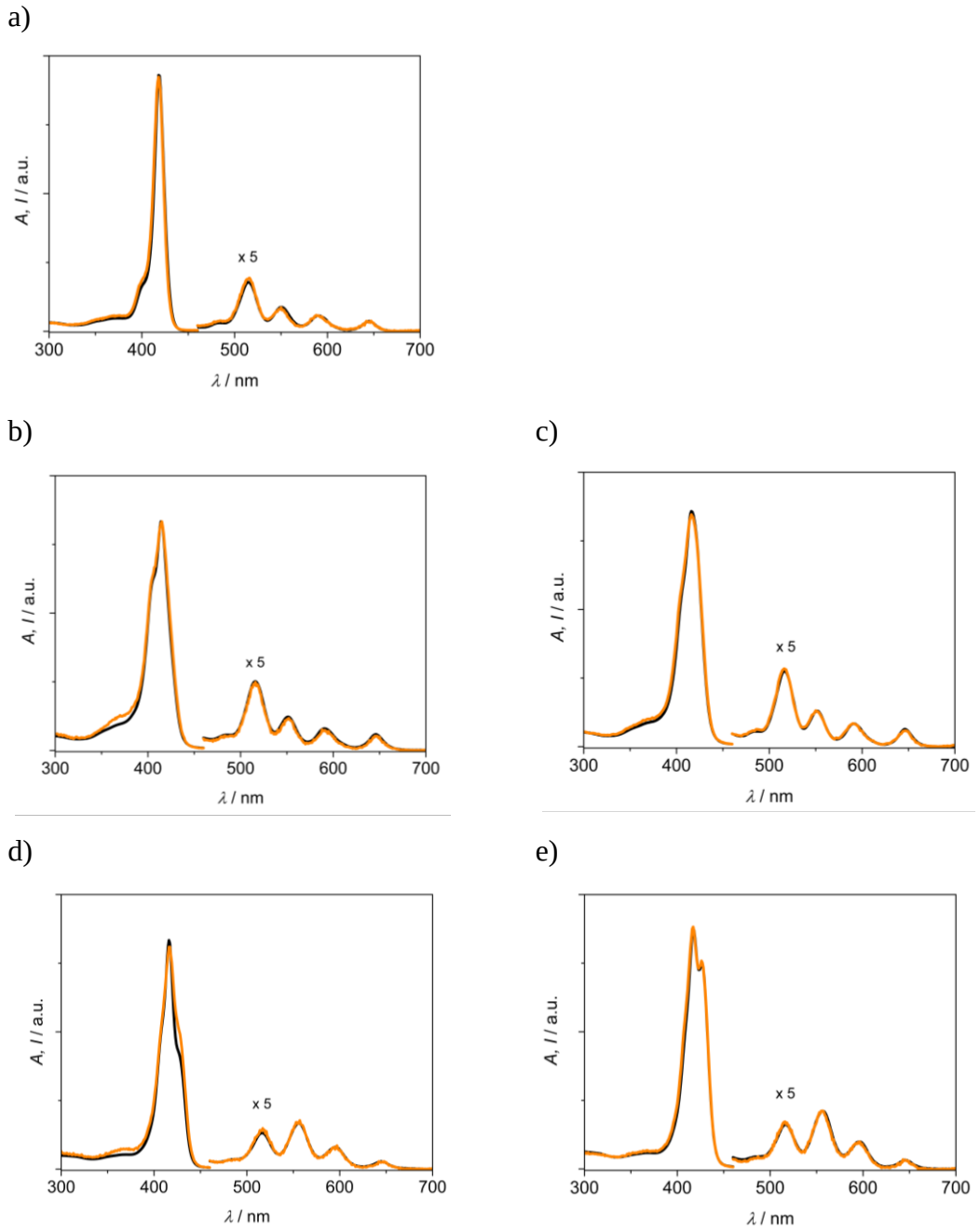

Figure 2.14. Corrected excitation spectra collected at 720 nm (orange) and arbitrary scaled absorption spectra (black) of a) **2H-alkyne**, b) **2H-S-2H**, c) **2H-L-2H**, d) **Zn-S-2H** and e) **Zn-L-2H** in CH_2Cl_2/MeOH (9:1). The good superimposition of excitation and absorption spectra confirm the genuineness of the emission and, in the monometallated cages, the high efficiency of the energy transfer process from the Zn-porphyrin unit to the free-base counterpart.[142]

To exclude the possibility that the energy transfer process is occurring in the monomers in solution, an equimolecular mixture of **2H-alkyne** and **Zn-alkyne** (Figure 2.15a) was excited at 557 nm, producing an emission spectrum perfectly matched with

the sum of the spectra of the models (Figure 2.15b), proving that there is no quenching of the Zn-porphyrin bands. Besides, 1.7 ns is measured as the fluorescence lifetime for the mixture at 610 nm, correspondent to the emission lifetime of **Zn-alkyne** (Table 2.1).

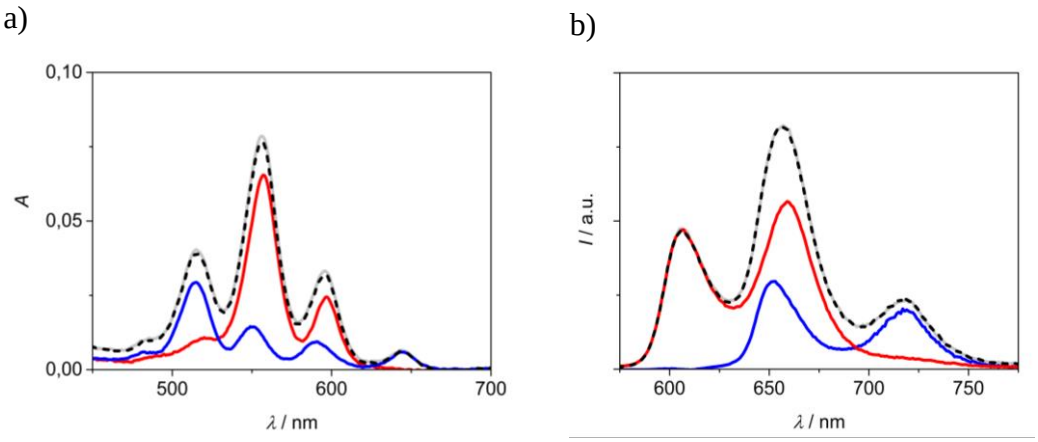

Figure 2.15. a) Absorption spectra of an equimolecular mixture of **2H-alkyne** and **Zn-alkyne** in CH_2Cl_2/MeOH (9:1) (grey, [**2H-alkyne**] = [**Zn-alkyne**] = $3.0 \cdot 10^{-6}$ M) and of solutions of the single compounds at the same concentration (blue: **2H-alkyne**, red: **Zn-alkyne**). The sum of the spectra of the single compounds is reported for comparison purposes (black dashed). b) Corrected emission spectra obtained from the solutions a) upon excitation at 557 nm (same color code).[142]

Emission measurements at low temperature (77 K) in CH_2Cl_2/MeOH (1:1) glassy mixture allowed the definition of singlet excited state energy levels for all porphyrin components of the four cages and triplet excited state levels for the Zn-porphyrins in the monometallic cages, where phosphorescence was observed in gated mode. Luminescence spectra are shown in Figure 2.16 and Figure 2.17 and the relevant data are summarized in Table 2.1. It can be noticed that, in the monometallated cages, the Zn-porphyrin fluorescence is suppressed similarly to the room temperature case (Figure 2.17), confirming the high efficiency of the quenching process operative within these cages.

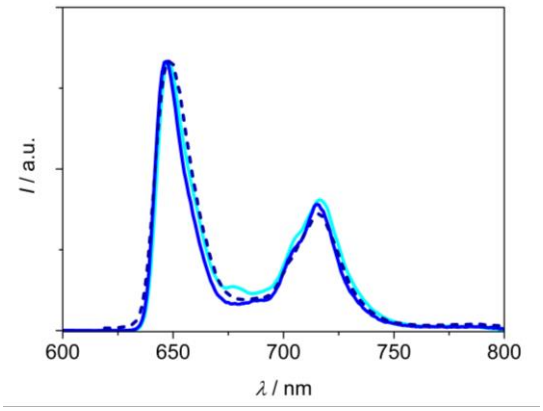

Figure 2.16. Normalized corrected emission spectra of **2H-S-2H** (cyan), and **2H-L-2H** (blue full) and **2H-alkyne** (blue dashed) in CH_2Cl_2/MeOH (9:1) glassy matrices at 77 K. λ_{exc} = 550 nm.[142]

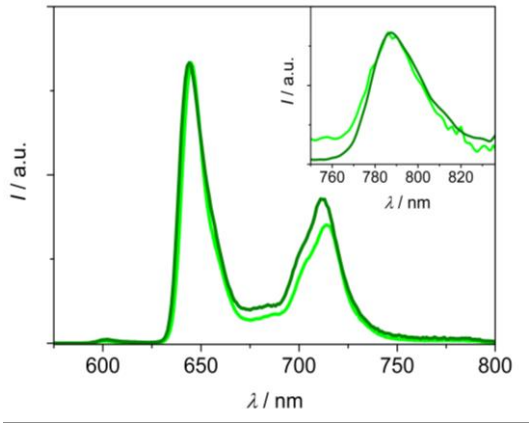

Figure 2.17. Normalized corrected fluorescence and phosphorescence (inset) spectra of **Zn-S-2H** (light green) and **Zn-L-2H** (olive) in CH_2Cl_2/MeOH (1:1) glassy matrices at 77 K. Gating parameters; delay: 1 ms, gate: 5ms. λ_{exc} = 420 nm for phosphorescence spectra.[142]

Time-resolved luminescence experiments:

To characterize the photoinduced process occurring in **Zn-S-2H** and **Zn-L-2H**, time-resolved luminescence experiments in the picosecond range were conducted. The measurements have been performed upon excitation at 560 nm, where the Zn-porphyrin component is excited prevalently, with a 100-fs pulsed laser and acquiring luminescence images with a streak camera apparatus (time resolution: 1 ps). Low laser power and fast image acquisition in analog integration mode were used (see 2.4. Experimental for details) to prevent photo-degradation of the compounds. The images identify the existence of a fast process, where a decay in the emission region of the Zn-porphyrin (600-620 nm) is accompanied by a rise in the 700-750 nm spectral region, where only emission from the free-base component is observable (Figure 2.18 and Figure 2.19). The decay of the Zn-porphyrin luminescence can be fitted with a bi-exponential function where the main component has a lifetime of 10 ps in **Zn-S-2H** and 7 ps and **Zn-L-2H** (Figure 2.18). The longer component (accounting for *ca*. 10% of the decay) can be attributed to a tail of the free-base porphyrin emission or a minor presence of a photo-product. A precise fitting of the rise time of the free-base signal is difficult but is compatible with the lifetime of the quenched Zn-porphyrin emission (Figure 2.19), confirming the sensitization of the free-base singlet excited state upon energy transfer from the Zn-porphyrin component.

The difference between the quenched lifetimes of the Zn-porphyrin component in the two cages is minimal but significant and indicates that the energy transfer process is faster in **Zn-L-2H** than in **Zn-S-2H**. The energy transfer rate, in fact, is $(1.0 \pm 0.1)\cdot10^{11}$ s^{-1} and $(1.4 \pm 0.2)\cdot10^{11}$ s^{-1} for **Zn-S-2H** and **Zn-L-2H**, respectively (see 2.4. Experimental for

details). It follows that the process occurs with an efficiency close to 100% in both cages. To better analyze the nature of the energy transfer process, the data have been treated according to the Föster-type mechanism, which is usual between porphyrin chromophores. The overlap integral (J^F) between the emission spectrum of the donor (the bis Zn-porphyrin model) and the absorption spectrum of the acceptor (half the absorption spectrum of the bis free-base porphyrin cage) has been calculated to be $1.96 \cdot 10^{-14}$ $cm^3 \cdot M^{-1}$ and $1.88 \cdot 10^{-14}$ $cm^3 \cdot M^{-1}$ for **Zn-S-2H** and **Zn-L-2H**, respectively. An estimation of the geometrical factor K^2 (see 2.4. Experimental for details) gives values of 0.09 for the cage with short linkers and 1.88 for the cage with longer linkers (by considering $\theta_D = \theta_A = 40° \div 90°$ in **Zn-S-2H** and $\theta_D = \theta_A = 15° \div 40°$ in **Zn-L-2H** and ϕ varying from 0° and 60°, according to the geometrical parameters derived for similar cages).[141]

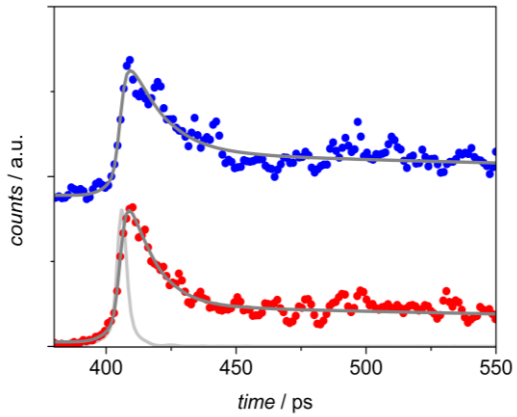

Figure 2.18. Normalized luminescence decays in the 600-620 nm spectral region for **Zn-S-2H** (blue) and **Zn-L-2H** (red). The bi-exponential fittings are reported as grey lines. The excitation profile is shown in light grey. Excitation at 560 nm (26 µJ/pulse).[142]

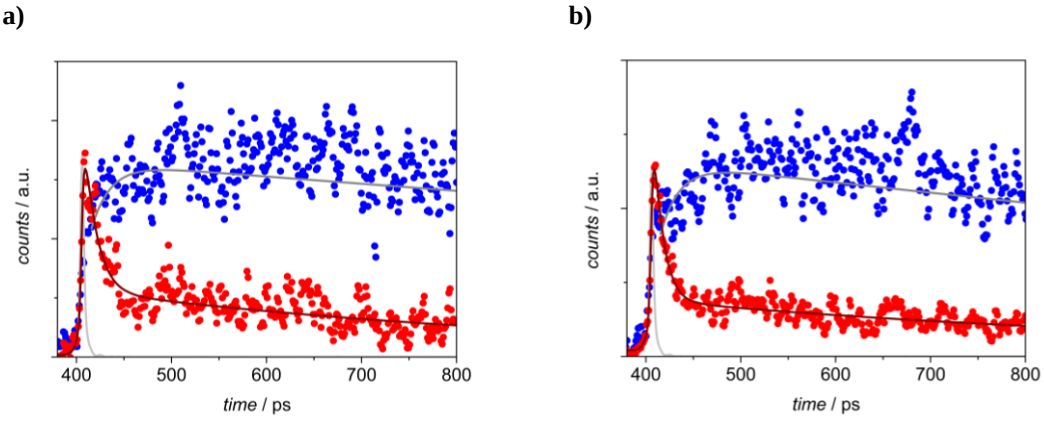

Figure 2.19. Arbitrary scaled luminescence profiles in the 600-620 nm spectral region (red dots) and in the 700-750 nm spectral region (blue dots) for a**) Zn-S-2H** and b) **Zn-L-2H** in CH_2Cl_2/MeOH (9:1). The bi-exponential fittings are reported as lines. The excitation profile is shown as light grey. Excitation at 560 nm (26 µJ/pulse).[142]

With these parameters and considering the fluorescence quantum yield and the lifetime of the donor in both cases, it is possible to evaluate the donor-acceptor distances that should result in the experimental rate constants based on a Föster-type energy-transfer mechanism. The obtained distances are 6.6 Å and 11.0 Å for **Zn-S-2H** and **Zn-L-2H**, respectively. While the first value is in good agreement with the distance between the two porphyrins estimated in the parent system (7 Å), the second value is not reasonable for a system where the long linker allow for a closer interaction between the porphyrins. Although the estimation of K^2 for these systems involves approximations, in the case of **Zn-L-2H** a possible deviation from the classical Föster treatment can be envisaged, with a weaker short-range dependence of the rate constant, as already observed for closely spaced π systems.[146] At a supposed interplanar distance of 4 Å, estimated for the parent cage,[141] we cannot also exclude a contribution from an electron exchange (Dexter) mechanism, that has been found to be operative at very short (<5-6 Å) donor-acceptor distances in cofacial porphyrinic systems.[147,148]

2.3. Conclusions

The photophysical properties of the four flexible covalent cages composed by either two free-base porphyrin or one free-base porphyrin and one Zn(II)- porphyrin, connected by flexible linkers of different lengths, has been performed by means of steady-state and time-resolved spectroscopic studies.

The proximity of the two porphyrins within the structure of the cages provokes strong exciton interactions, observable in the absorption spectra. Regarding the emission properties of the cages, they depend on the composition and/or on the lengths of the linkers: the free-base units display perturbed fluorescence quantum yield and lifetime only in the monometallated cages, where the Zn counterpart influences their radiative features, with a stronger impact in the cage with shorter linkers.

The Zn-porphyrins are quantitatively quenched by a fast energy transfer process that sensitizes the free-base emission in both monometallated cages. This photoinduced process is slightly faster in the cage with longer linkers, probably because of the very short interplanar distance between the porphyrins in this cage, supposed to be *ca*. 4 Å.

This outcome underlines the role of the linkers and of the arrangement of the components in affecting the photophysical properties of covalent porphyrinic cages.

2.4. Experimental

Spectroscopic grade CH_2Cl_2 and MeOH were from Merck and used as received.

Absorption spectra were recorded with Perkin–Elmer Lambda 650 UV-vis and Perkin–Elmer Lambda 950 UV-VIS-NIR spectrophotometers. Integrated absorption coefficients were calculated by plotting molar absorption coefficients as a function of absorption energy (in wavenumbers) and calculating the area under the curves.

Emission spectra were collected with an Edinburgh FLS920 fluorimeter, equipped with a Peltier-cooled Hamamatsu R928 PMT (280–850 nm), and corrected for the wavelength-dependent phototube response. Corrected excitation spectra were recorded with the same fluorimeter. Emission quantum yields were evaluated from the area of the luminescence spectra, corrected for the photomultiplier response, with reference to *meso*-tetraphenylporphyrin in aerated toluene (ϕ_{fl} = 0.11).[149] Measurements at 77K were performed with the same fluorimeter, making use of Pyrex tubes dipped in liquid nitrogen in a quartz Dewar. Gated emission spectra were acquired by using a time-gated spectral scanning mode and a μF920H Xenon flash lamp (pulse width < 2 μs, repetition rate between 0.1 and 100 Hz) as excitation source. Spectra were corrected for the wavelength dependent photomultiplier response. Triplet excited state lifetimes were measured with the same apparatus in the multichannel scaling mode.

Fluorescence lifetimes in the nanosecond range were detected by using an IBH Time Correlated Single Photon Counting apparatus with Nano-LED excitation at 465 nm. Analysis of the decay profiles against time was performed using the Decay Analysis Software DAS6 provided by the manufacturer.

Fluorescence lifetimes in the ps regime were measured by means of a Hamamatsu synchroscan streak-camera apparatus (C10910-05 main unit and M10911-01 synchroscan unit) equipped with an ORCA-Flash 4.0 V2 charge-coupled device (CCD) and an Acton spectrograph SP2358. As excitation source, a Newport Spectra Physics Solstice-F-1K-230 V laser system, combined with a TOPAS Prime (TPR-TOPAS-F) optical parametric amplifier (pulse width: 100 fs, 1 kHz repetition rate)[150] was used, tuned at 560 nm. To reduce photo-degradation, the pump energy on the sample was reduced to 26 μJ/pulse. Emission from the sample, collected at a right angle with a 1 mm slit, was focused by means of a system of lenses into the spectrograph slit. Streak images were taken in analogous integration mode (100 exposures, exposure time: 2 s). The decays were measured over emission spectral ranges of 20–40 nm. HPD-TA 9.3 software from

Hamamatsu was used for data acquisition and analysis. The overall time resolution of the system after deconvolution procedure was 1 ps.

The energy transfer rate in the monometallic cages was calculated as $k_{en} = 1/\tau - 1/\tau_0$, in which τ is the lifetime of the quenched donor unit and τ_0 the lifetime of the unquenched unit, *i.e.* the lifetime of the reference model (the Zn-component in the bis Zn-porphyrin cages): 1.7 ns for **Zn-S-Zn** and 1.6 ns for **Zn-L-Zn**.[141] The error for the energy transfer rate value has been estimated according to the partial derivative methods and by taking the temporal resolution of the measuring system as uncertainty on the lifetime value (1 ps for τ, measured with the streak camera apparatus, and 0.2 ns for τ_0, measured with the Time Correlated Single Photon Counting equipment). The energy transfer efficiency is defined as $\eta_{en} = k_{et}/(k_{et} + \tau_0^{-1})$.

The calculation of the energy-transfer rate constant according to the Förster theory was performed by using equation (2.1)[151], where d_{DA} is the distance between the centers of mass of the donor and acceptor, ϕ and τ_0 are the emission quantum yield and lifetime of the donor, J^F the overlap integral, n the refractive index of the solvent and K^2 the orientation factor, calculated according to equation (2.2),[152] where θ_D and θ_A are the angles formed between the line connecting the donor and acceptor centers and the transition moments of the donor and acceptor, respectively, and ϕ is the angle between the projections of the transition moments on a plane perpendicular to the line connecting the centers of the donor and the acceptor.

$$k_{en}^{F} = \frac{8.8 \cdot 10^{-25} K^2 \phi}{n^4 \tau_0 d_{DA}^6} J^f \tag{2.1}$$

$$K^2 = (sin\theta_D sin\theta_a cos\phi - 2cos\theta_D cos\theta_A)^2 \tag{2.2}$$

Estimated errors are 10% on lifetimes, 20% on quantum yields, 20% on molar absorption coefficients and 3 nm on emission and absorption peaks.

Chapter 3: Ag(I) Complexation of Porphyrinic Covalent Cages equipped with flexible linkers and study of their Host-Guest inclusion Properties

3.1. Introduction

As it has been previously introduced in Chapter 2, the use of Ag(I) as an effector allowed the reversible *on/off* control of the inclusion of the guest NDI into the bis-Zn(II)-porphyrin cage.[140] The use of silver(I) is highly attractive as effector due to its versatile coordination sphere and coordination numbers ranging from 2 to 6. This second row transition metal has been largely employed in supramolecular chemistry thanks to the labile bonds that silver-ligand form allowing for the thermodynamic product to be reached by self-correction. Besides, it is also easy to decoordinate by using a compatible anion such as chloride.[123,153]

Following this precedent, in the first section of this Chapter, the study of the complexation upon Ag(I) addition of the four cages **2H-S-2H**, **2H-L-2H**, **Zn-S-2H** and **Zn-L-2H** introduced in Chapter I, is performed by means of absorption and emission spectroscopy, time-correlated single photon counting and ultrafast luminescence measurements.

The encapsulation process of guest molecules into the cavity of three-dimensional host structures is of great interest in supramolecular chemistry. It allows to isolate the guest from the bulk medium and to establish new interactions with the host structure that can modify its physical and chemical properties.[154] To achieve a host-guest complex, a fine electronic and geometrical match has to take place.[155,156] Fortunately, the inclusion of the guest can be controlled with external stimuli such as protons,[157–163] electrons[164–166] or chemical entities[41,167–171] that interact with specific sites of the host, far from the binding site of the guest and provokes large and reversible modifications on the host structure. This control is equivalent to the allosteric one, used in biological systems.[172,173]

One example of a photoresponsive cage was reported by Huang *et al*., the cage was an azo-benzene-bridged cryptand that can be controlled between *cis* and *trans* isomer by UV/Vis irradiation. The cage presents an on/off capacity on binding with 2,7-diazapyrenium derivatives which can be encapsulated when the *cis* isomer form is in solution (Figure 3.1).[157]

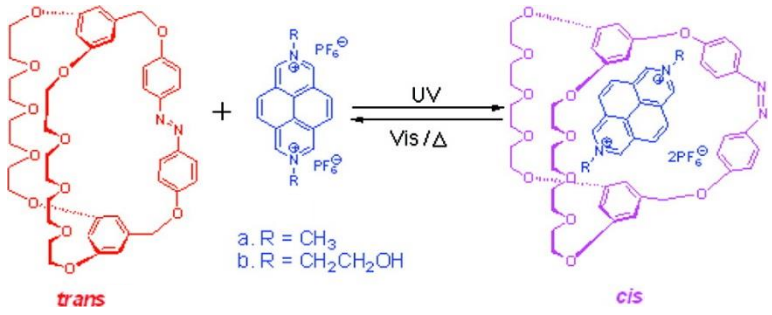

Figure 3.1. Schematic photo *trans-cis* isomerization and encapsulation properties of the azo-benzene cryptand. Reproduced with permission of © 2021 American Chemical Society.[157]

As mentioned before, if a fine electronic and geometrical match takes place and also, once the complex is formed, an external stimulus can reverse the complexation of the guest into the supramolecular entity, that system would be ideal for drug delivery applications. Drug delivery aims to make drug treatments more effective, trying to release the pharmaceutical in the place of action and also to control its release through a specific mechanism such as light, a change of the pH, etc… From this area of study we can conclude that all carriers designed for this application have advantages and limitations, one of the challenges is to enlarge the available options to deliver insoluble or toxic drugs.[174]

One example employing porphyrin-gold nanostructures was reported by Maiti *et al*. They designed a nanochemotherapeutic system composed by tetrasodium salt of *meso*-tetrakis-(4-sulfonatedphenyl)porphyrin linked to gold nanoparticles (Figure 3.2). These nanocarriers were capable of discriminating positively towards tumor cells to internalize within them and deliver the antitumor drug doxorubicin in the nucleus of the affected cells thanks to the lowered pH of the environment.[175]

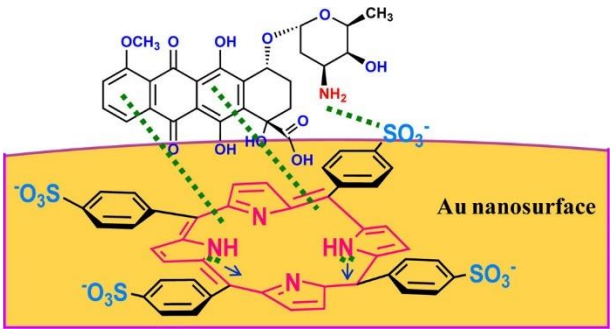

Figure 3.2. Representation of the *meso*-tetrakis-(4-sulfonatedphenyl)porphyrin coordinated to the antitumor drug (doxorubicin) attached to the surface of the gold nanoparticles through coordination of the pyrrolic nitrogen atoms with gold. Reproduced with permission of © 2021 American Chemical Society.[175]

Following the work on the encapsulation process of NDI into the Zn(II) porphyrin based cages mentioned before, MD simulations showed that upon NDI complexation the two porphyrins get closer with an optimized face-to-face orientation, suggesting an induced fit mechanism through π-π interactions with the NDI aromatic cycle. A photoinduced electron transfer reaction takes place between the host and the guest, confirmed by ultrafast transient absorption experiments.[176]

Therefore, in the second part of this Chapter, the encapsulation process of ethionamide (ETH) as guest is studied for cages **2H-S-2H** and **Zn-S-2H**, in their "open" conformation. ETH has been chosen as a model of a drug that can interact with the porphyrin of the cages, thanks to its coordination sites on nitrogen and sulfur atoms and its aromatic ring (see Figure 3.21 below). These experiments thus aim to bring a proof of concept for a future drug delivery system.

Regarding the guest, ethionamide is a nicotinamide derivative that possesses antibacterial activity, it is often used in combination with other drugs to treat drug-resistant tuberculosis. Nevertheless, the precise mechanism of action in cells is unknown, it might inhibit the synthesis of mycolic acid, a saturated fatty acid found in the cell wall, but also ethionamide would block the bacteria wall synthesis. This blockage leads to bacterial cell wall disruption and cell lysis.[177]

Two manuscripts reporting the work presented in this Chapter are currently under preparation for future submission.

3.2. Results and discussion

3.2.1. Photophysical characterization of the complexation process with Ag(I) in solution

The complexation experiments for the four cages have been performed in 5-8·10^{-7} M CH_2Cl_2/MeOH (9:1) solutions by adding Ag(OTf) (silver trifluoromethanesulfonate) salt diluted in the same solvent mixture as Ag(I) ions source.

Free-base porphyrin cages:

Addition of increasing amounts of Ag(I) to a **2H-S-2H** (7.5·10^{-7} M) solution in the range of 0-45 equivalents causes major absorption changes as displayed in Figure 3.3a. The Q-bands region is only slightly affected but the Soret band shows important changes. The peak at 415 nm increases in intensity and the original splitting, due to exciton coupling between the porphyrin units, disappears (Figure 3.3a). The resulting Soret band resembles that of the reference compound **2H-alkyne**.[142] This result suggests that a cage opening process, due to the coordination of the Ag(I) ions to the lateral triazoles, occurs since the larger distance between the porphyrin planes in the open conformation reduces the extent of the exciton coupling.

The emission spectrum of the cage, collected upon excitation at 409 nm (isosbestic point of the absorption titration), is slightly affected by the addition of silver(I). Just a small increase in intensity followed by a decrease is observed (Figure 3.3b).

Regarding the excited state lifetime, measured by TC-SPC, at the end of the titration it was slightly reduced with respect to that of the uncomplexed cage (8.4 *vs* 9.0 ns).[142]

a) b)

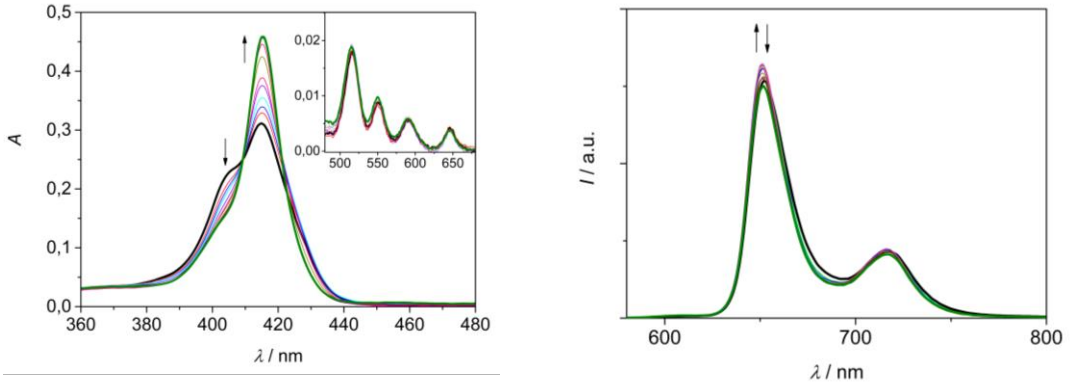

Figure 3.3. Absorption (a) and uncorrected emission spectra (λ_{exc} = 409 nm, isosbestic point) (b) of CH_2Cl_2/MeOH (9:1) solutions containing **2H-S-2H** (7.5·10^{-7} M) and increasing amounts of Ag(OTf) (0-45 equivalents). Inset of (a): amplification of the Q-bands region (480-680 nm).

The absorption and emission data have been analyzed with the software ReactLab Equilibria 1.1[178] by using a 1:4 (cage:Ag^+) binding model and considering Ag^+ as a non-absorbing and non-emissive specie. The fitting converges and the simulated spectra generated from the software belonging to the [(**2H-S-2H**)Ag_4]$^{4+}$ complex matches the experimental ones obtained at the end of the titration (Figure 3.4). The average binding constant, expressed in log(K_a/M^{-4}), is (18.94 ± 0.02).

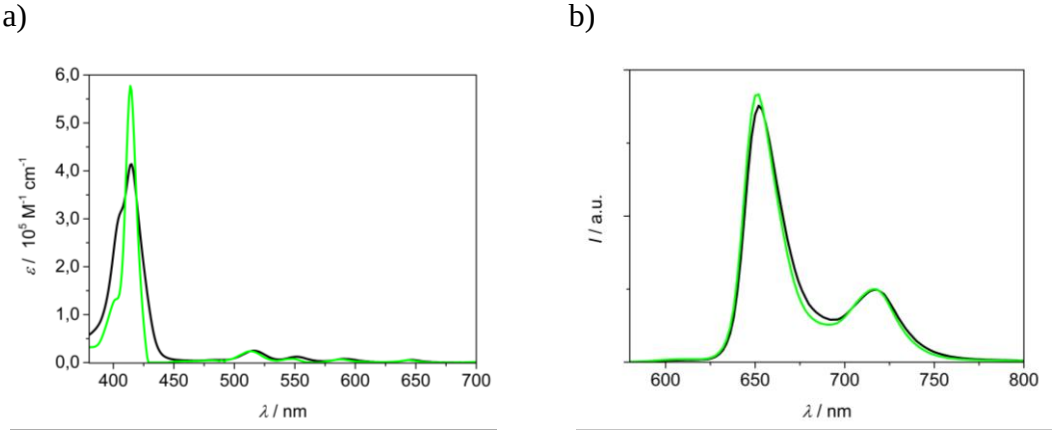

Figure 3.4. a) Experimental absorption spectrum of **2H-S-2H** (black, imposed in the fitting) and fitted absorption spectrum of the complex [(**2H-S-2H**)Ag_4]$^{4+}$ (green) in CH_2Cl_2/MeOH (9:1). b) Fitted emission spectrum of **2H-S-2H** (black) and [(**2H-S-2H**)Ag_4]$^{4+}$ (green). The fitting was performed with the software ReactLab Equilibria[178] by using a 1:4 (cage:Ag^+) binding model and Ag^+ as a non-absorbing and non-emissive species.

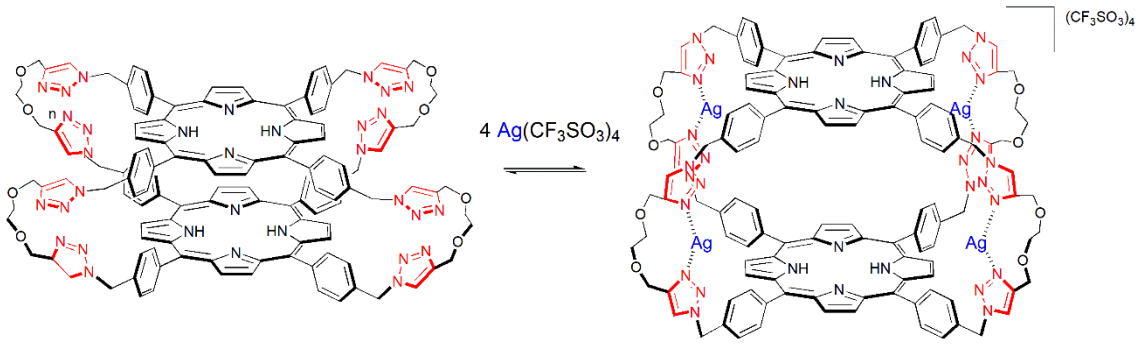

Figure 3.5. Schematic illustration of the complexation process of **2H-S-2H** with silver(I).

The behavior of the long **2H-L-2H** cage ($5.6 \cdot 10^{-7}$ M), upon increasing additions of Ag(I) in the range of 0-30 equivalents, well differs from that of its *short* version. Both absorption and emission spectra display drastic changes.

In absorption (Figure 3.6a), the Soret band at 416 nm nearly disappear while a new band at 445 nm increases, the spectra displaying an isosbestic point at 434 nm. In the Q-bands region, the original bands at 516, 550, 592 and 546 nm convert into two new bands at 623 and 654 nm (isosbestics at 503, 565, 580 and 599 nm). The changes described suggest that a metalation process of the core of the free-base porphyrins occurs (Figure

3.9). The features observed for the Ag(I) complexation of **2H-L-2H** differ from those of the species that forms in the bis-Ag(I) metalation of a monomeric free-base porphyrin,[138] and can be tentatively ascribed to the formation of a cage where both porphyrins are monometallated by comparison with the spectral characteristics reported for [**TPP**·Ag]$^{+}$ obtained by electrochemical reduction from [**TPP**·Ag]$^{2+}$ (bands at 457, 616 and 667 nm).[179] This unusual reactivity towards Ag(I) ions could be interpreted with the help of theorical calculations (explained below).

The emission titration, upon excitation at the isosbestic point at 434 nm, displays a progressive decrease in fluorescence intensity of the cage (Figure 3.6b), which supports the formation of metalated porphyrins since they are weakly emissive with respect to their free-base counterparts.[180]

The emission decay of the cage corresponding to the end of the titration, fitted by a double exponential, yields lifetime values of 6.0 and 0.5 ns (90% and 10% in pre-exponential ratio, respectively), therefore reduced with respect to the 9.0 ns lifetime value of the uncomplexed cage.[142]

a) b)

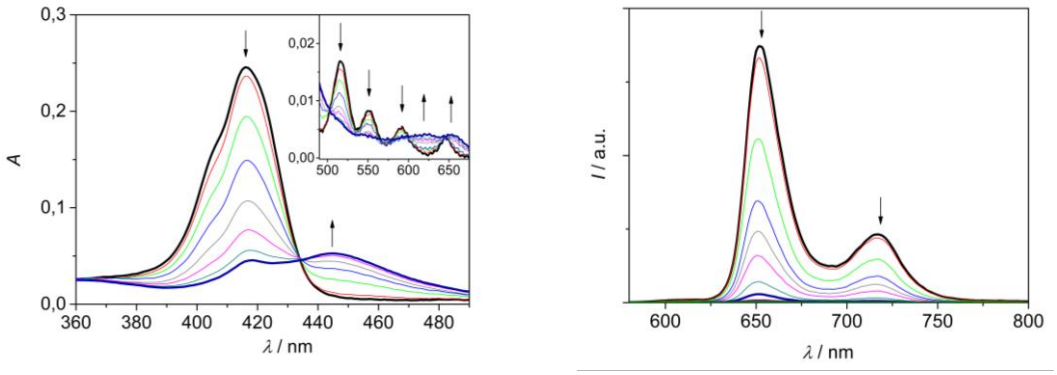

Figure 3.6. Absorption (a) and uncorrected emission spectra (λ_{exc} = 434 nm, isosbestic point) (b) of CH_2Cl_2/MeOH (9:1) solutions containing **2H-L-2H** ($5.6 \cdot 10^{-7}$ M) and increasing amounts of Ag(OTf) (0-30 equivalents). Inset of (a): amplification of the Q-bands region (490-700 nm).

An excess of Ag(I), up to 400 equivalents, affects the equilibrium of the complexation process of **2H-L-2H**. In the absorption spectra, two new bands increase at 421 and 541 nm, while the emission intensity continues to decrease (Figure 3.7). This subsequent process could be ascribed to the interaction of Ag(I) ions with the triazole ligands integrated in the cage linkers after the porphyrins are metalated, inducing a conformational change in the system.

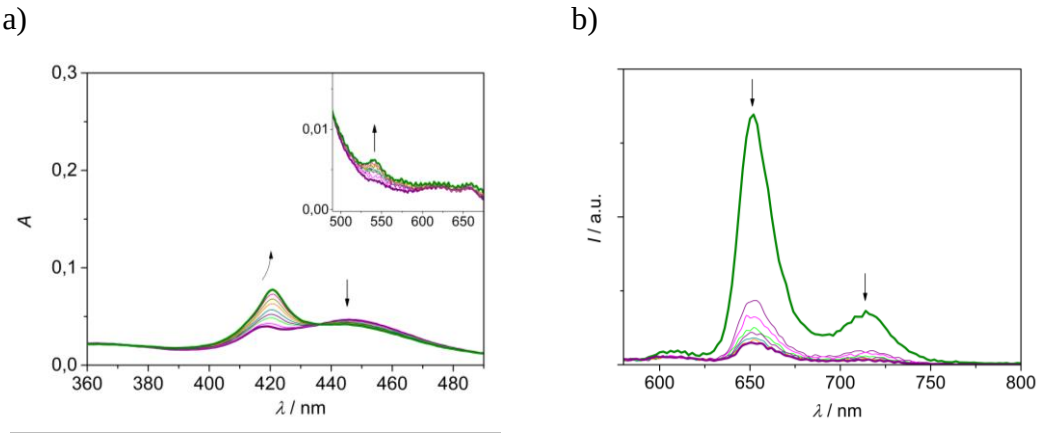

Figure 3.7. Absorption (a) and uncorrected emission spectra (λ_{exc} = 434 nm, isosbestic point) (b) of CH_2Cl_2/MeOH (9:1) solutions containing **2H-L-2H** ($5.6 \cdot 10^{-7}$ M) and increasing amounts of Ag(OTf) (30-400 equivalents). Inset of (a): amplification of the Q-bands region (490-700 nm). In (b) the y-axis scale is amplified by a factor of 3 with respect of the scale of Figure 3.6b.

The absorption and emission data for the first equilibrium converged when a 1:2 model (cage:Ag^+) was applied in ReactLab software,[178] (Figure 3.8). The derived binding constant was $\log(K_a/M^{-2}) = (10.48 \pm 0.01)$.

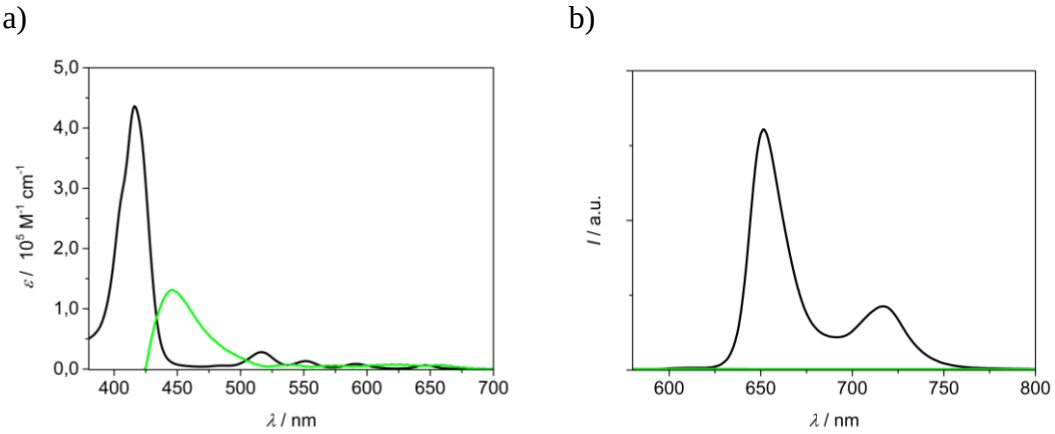

Figure 3.8. a) Experimental absorption spectrum of **2H-L-2H** (black, imposed in the fitting) and fitted absorption spectrum of the complex $[(\mathbf{2H\text{-}L\text{-}2H})Ag_4]^{4+}$ (green) in CH_2Cl_2/MeOH (9:1). b) Fitted emission spectrum of **2H-L-2H** (black) and $[(\mathbf{2H\text{-}L\text{-}2H})Ag_4]^{4+}$ (green). The fitting was performed with the software ReactLab Equilibria[178] by using a 1:4 (cage:Ag^+) binding model and Ag^+ as a non-absorbing and non-emissive species.

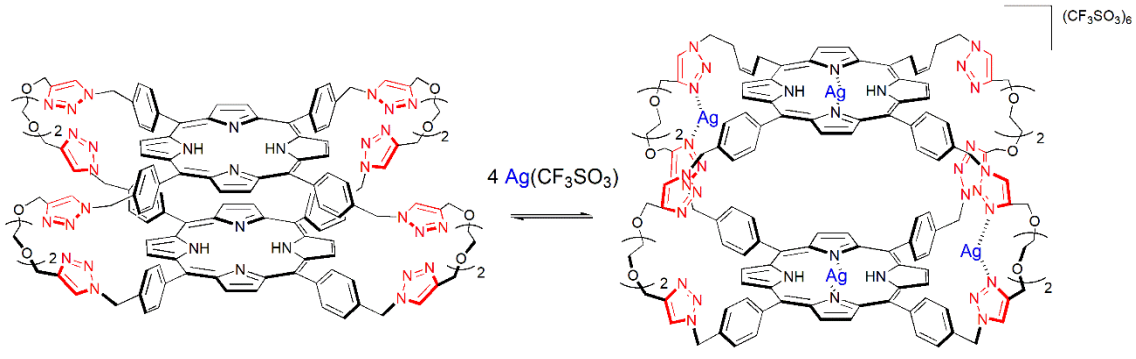

Figure 3.9. Schematic illustration of the assumed complexation processes of **2H-L-2H** with silver(I).

Computational results on 2H-S,L-2H cages:

This study was carried out in collaboration with Prof. Daidone's group.**

As mentioned before, molecular dynamics (MD) simulations of both uncomplexed cages **2H-S-2H** and **2H-L-2H** were performed to compare the structural and dynamics characteristics that could explain the difference in their behavior upon addition of Ag(I).

The MD simulations showed that the closed conformation of the cages is different. In **2H-L-2H** the distance between the porphyrins planes is lower on average than in **2H-S-2H**. Besides, the relative orientation of the two porphyrins is different in the two cages. In **2H-L-2H** the two porphyrins are parallel and cofacial, while in **2H-S-2H,** the planes take more often an oblique and slipped conformation. This can be explained thanks to the more rigid "shorter" linkers that do not facilitate a tightly conformation that implies the bending of the linkers.

The different conformation of the two uncomplexed cages also affect their reactivity towards Ag(I) ions. The more slipped conformation present in **2H-S-2H** determine an average *outer* orientation of the two NH groups of the porphyrin plane. Contrarily, in **2H-L-2H** and *inward* orientation of the NH groups is favored. The latter conformation exposes to the solvent the lone pair of the nitrogen, so that upon addition of Ag(I) ions in solution the nitrogen can coordinate easier to the silver ions and this process can compete with the complexation process of the triazole ligands.

Monometallated Zn-/free-base porphyrin cages:

Addition of increasing amounts of Ag(I) to the monometallated cage **Zn-S-2H** ($5.5 \cdot 10^{-7}$ M) in the range of 0-40 equivalents causes changes in both absorption and emission spectra. A reduction of the splitting of the Soret band is observed in the absorption spectra, forming a single band more intense with maximum at 418 nm (Figure 3.10a), while the Q-bands region remains almost unaltered. These data, similar to those observed for its free-base analogous **2H-S-2H** cage, points towards a cage opening process.

Differently from its analogous **2H-S-2H**, for **Zn-S-2H** in the emission titration it can be observed an increase in intensity of both the bands of the free-base unit (652 and 717 nm)[142] and of the Zn-porphyrin (606 nm, the second band at *ca*. 660 nm is superimposed with the free-base porphyrin emission)[142] (Figure 3.10b).

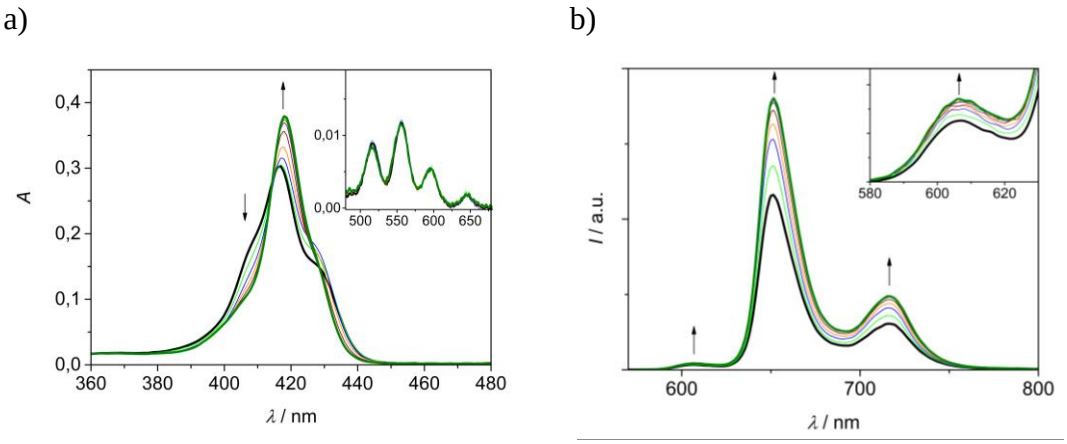

Figure 3.10. Absorption (a) and uncorrected emission spectra (λ_{exc} = 415.5 nm, isosbestic point) (b) of CH_2Cl_2/MeOH (9:1) solutions containing **Zn-S-2H** ($5.5 \cdot 10^{-7}$ M) and increasing amounts of Ag(OTf) (0-40 equivalents). Inset of (a): amplification of the Q-bands region (480-680 nm). Inset of (b): amplification of the 580-630 nm region.

Figure 3.11 displays the Zn-porphyrin emission in **Zn-S-2H** where the contribution of a normalized **2H-S-2H** spectrum at 712 nm has been subtracted to the spectrum of the mixture for each point of the titration of the monometallated cage, thus making more noticeable the increase of the Zn-porphyrin unit emission intensity upon addition of Ag(I).

It has been previously explained (Chapter 2) that the emission properties of the free-base component in **Zn-S-2H** are affected by the presence the of closely spaced Zn-porphyrin counterpart, with a reduction on the quantum yield and lifetimes values (6.7 *vs* 8.5 ns) with respect to the model monomer **2H-alkyne** and cage **2H-S-2H**.[142] The recovery of the free-base emission intensity upon addition of Ag(I) evidences the separation of the two units due to the coordination of the silver(I) ions to the triazole ligands (Figure 3.13). In fact, the lifetime of the free-base emission measured at 720 nm for the complex was found to be 7.9 ns, which is closer to the value of 8.5 ns of the free-base porphyrin unaffected by the Zn-counterpart.[142]

The parting of the two units towards an open cage conformation also decreases the efficiency of the energy transfer occurring from the Zn-porphyrin to the free-base counterpart,[142] with the result of an increase of the emissions intensity of the Zn component in the complexed cage.

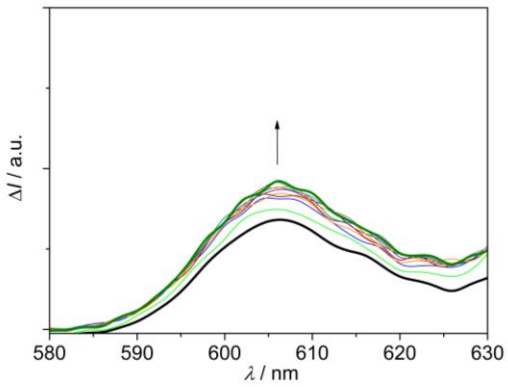

Figure 3.11. Emission spectra (λ_{exc} = 415.5 nm) of CH_2Cl_2/MeOH (9:1) solutions containing **Zn-S-2H** ($5.5 \cdot 10^{-7}$ M) and increasing amounts of AgOTf (0-40 equivalents). The spectra are expressed as differential intensity, calculated by subtracting, from the spectrum of the cage at each point of the titration, an emission spectrum of **2H-S-2H** normalized at 712 nm.

The absorption and emission data could be fitted with a 1:4 (cage:Ag^+) binding model with ReactLab[178] software (Figure 3.12). The derived binding constant for this system was $\log(K_a/M^{-4}) = (22.09 \pm 0.05)$.

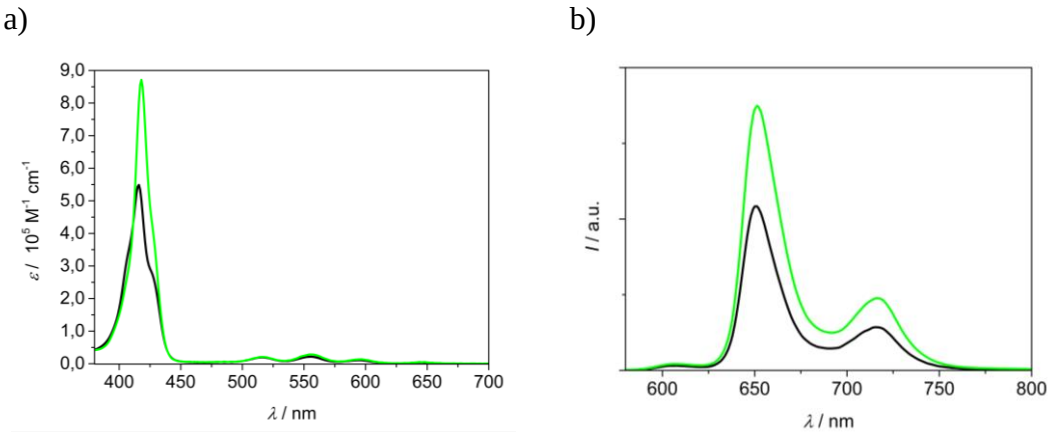

Figure 3.12. a) Experimental absorption spectrum of **Zn-S-2H** (black, imposed in the fitting) and fitted absorption spectrum of the complex [(**Zn-S-2H**)Ag_4]$^{4+}$ (green) in CH_2Cl_2/MeOH (9:1). b) Fitted emission spectrum of **Zn-S-2H** (black) and [(**Zn-S-2H**)Ag_4]$^{4+}$ (green). The fitting was performed with the software ReactLab Equilibria[178] by using a 1:4 (cage:Ag^+) binding model and Ag^+ as a non-absorbing and non-emissive species.

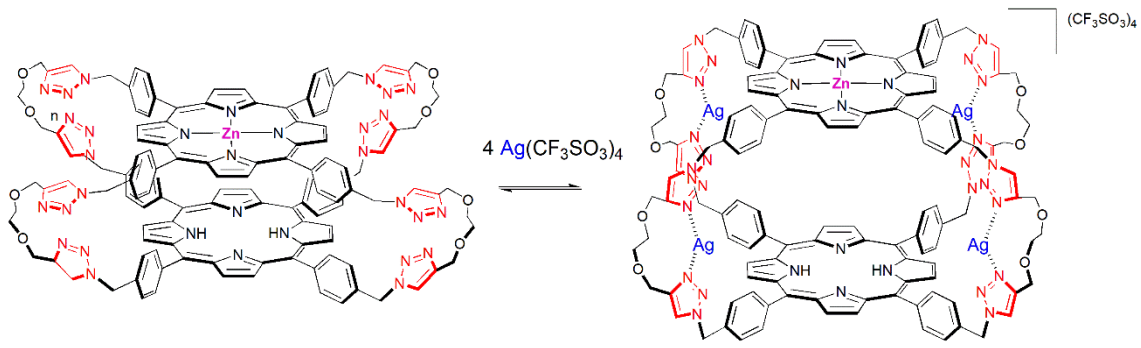

Figure 3.13. Schematic illustration of the complexation process of **Zn-S-2H** with silver(I).

The behavior of the monometallated cage **Zn-L-2H** differs from that of its analogous bis free-base version, **2H-L-2H**. The addition of increasing amounts of Ag(I) to **Zn-L-2H** ($6.5 \cdot 10^{-7}$ M) in the range of 0-25 equivalents provokes changes in absorption and emission spectra. The absorption spectra testify again the reduction of the splitting of the Soret band with an increase of the band at 417 nm and a reduction of the shoulder at 426 nm (Figure 3.14). The Q-bands region does not present any significant modifications. These data supports the opening process of the cage, as seen before for **2H-S-2H** and **Zn-S-2H**.

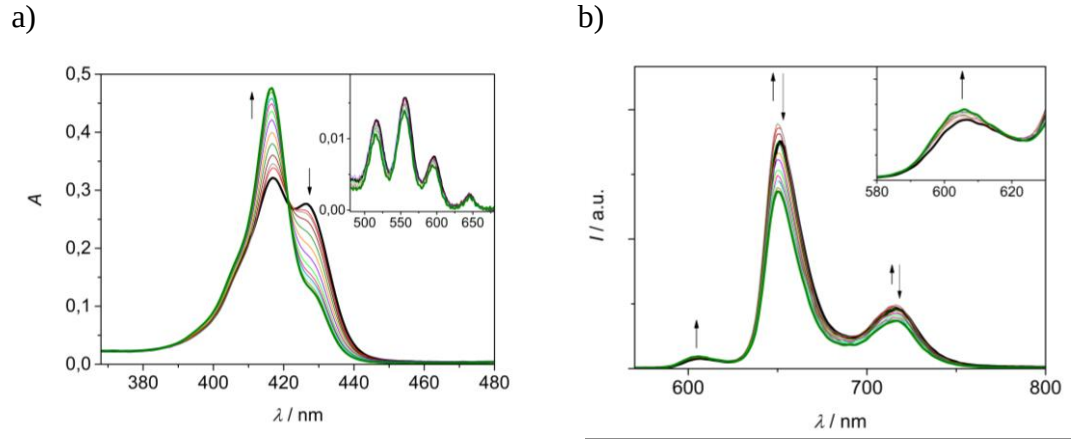

Figure 3.14. Absorption (a) and uncorrected emission spectra (λ_{exc} = 421 nm, isosbestic point) (b) of CH_2Cl_2/MeOH (9:1) solutions containing **Zn-L-2H** ($6.5 \cdot 10^{-7}$ M) and increasing amounts of Ag(OTf) (0-25 equivalents). Inset of (a): amplification of the Q-bands region (480-680 nm). Inset of (b): amplification of the 580-630 nm region.

Regarding the emission spectra, a different behavior from that of its analogous **Zn-S-2H** is observed (Figure 3.14b). The band corresponding to the Zn-porphyrin emission at 606 nm presents an increase in intensity until the end of the titration, confirmed by considering the subtraction of the free-base contribution (Figure 3.15). Conversely, the bands of the free-base component at 652 and 716 nm show a slight increase followed by a decrease.

The reduction of the efficiency of the energy transfer process occurring in the cage can explain the increase in intensity of the Zn-porphyrin, as well as for its analogous **Zn-S-2H**. The dual behavior of the free-base emission is more complicated to justify. The initial increase can be attributed to a recovery of the emission of the unit, which is reduced in the cage by the presence of the Zn counterpart (*ca*. 20% reduction),[142] the subsequent decrease could be explained by an interaction of the free-base porphyrin with the linked Ag(I), as the metalation of the core can be discarded by the absorption features of the complex.

The lifetime of the free-base component in the complex was slightly decreased in comparison to that of the same unit in the bare cage, i.e. 7.0 *vs* 7.6 ns.[142]

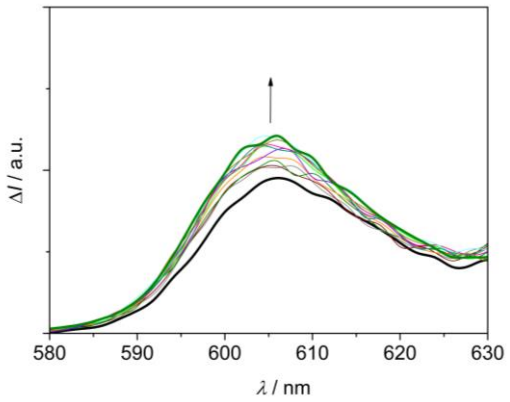

Figure 3.15. Emission spectra (λ_{exc} = 421 nm) of CH_2Cl_2/MeOH (9:1) solutions containing **Zn-L-2H** ($6.5 \cdot 10^{-7}$ M) and increasing amounts of AgOTf (0-40 equivalents). The spectra are expressed as differential intensity, calculated by subtracting, from the spectrum of the cage at each point of the titration, an emission spectrum of **2H-L-2H** normalized at 712 nm.

The absorption and emission data have been fitted with a 1:4 model (cage:Ag^+) with ReactLab[178] software (Figure 3.16) and the derived binding constant for the system is $\log(K_a/M^{-4}) = (20.78 \pm 0.02)$.

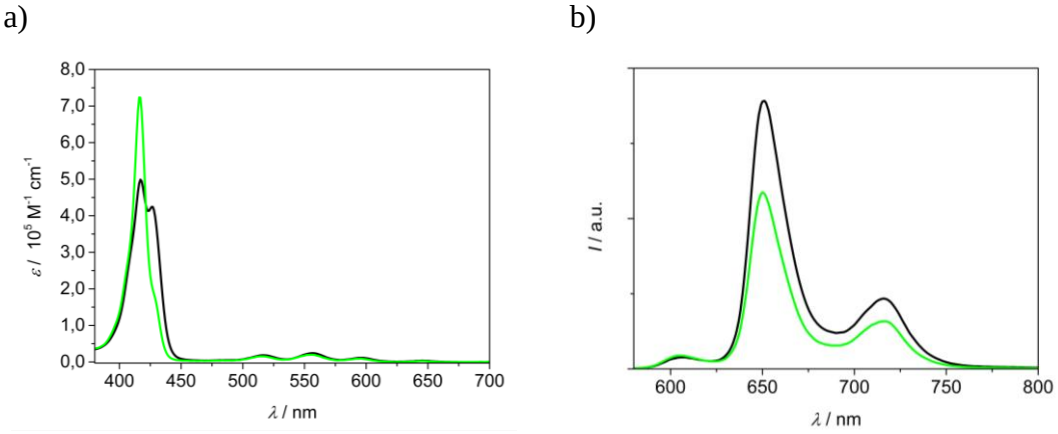

Figure 3.16. a) Experimental absorption spectrum of **Zn-L-2H** (black, imposed in the fitting) and fitted absorption spectrum of the complex [(**Zn-L-2H**)Ag_4]$^{4+}$ (green) in CH_2Cl_2/MeOH (9:1). b) Fitted emission spectra of **Zn-L-2H** (black) and [(**Zn-L-2H**)Ag_4]$^{4+}$ (green). The fitting was performed with the software Reactlab Equilibria[178] by using a 1:4 (cage:Ag^+) binding model and Ag^+ as a non-absorbing and non-emissive species.

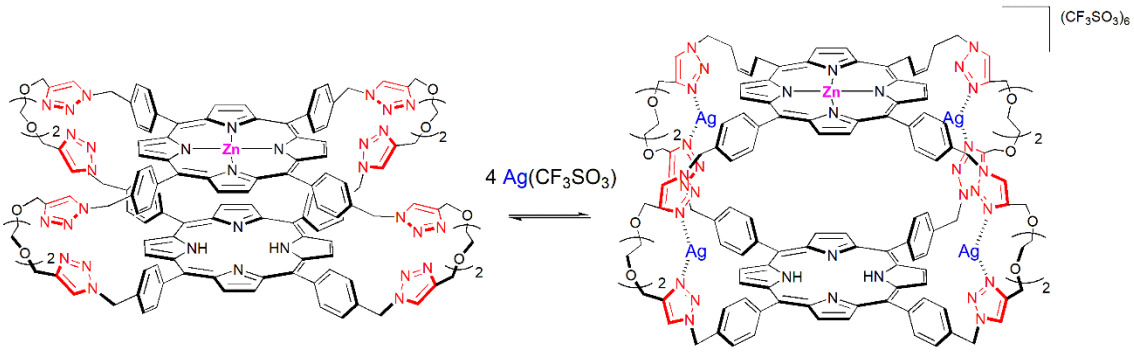

Figure 3.17. Schematic illustration of the complexation process of **Zn-L-2H** with silver(I).

Ultrafast luminescence measurements on Zn-S,L-2H:

The observed modifications in the emission properties of the Zn-porphyrin unit in the titrations of **Zn-S-2H** and **Zn-L-2H** with Ag(I) point to a modification of the efficiency of the energy transfer process upon complexation. Ultrafast luminescence measurements were carried out on the complexed cages in order to get insights on this process.

The luminescence time profiles of the two complexed cages in the range 600-620 nm, where uniquely the emission of the Zn-porphyrin is collected, are shown in Figure 3.18. The decays are fitted with lifetimes of 230 ps and 160 ps for **Zn-S-2H** and **Zn-L-2H**, respectively.[142] Taking into account a lifetime of 1.7 ns for the unquenched Zn-porphyrin model **Zn-alkyne**,[142] the efficiency of the energy transfer decreases from 99.4% to 86.5% in **Zn-S-2H**, and from 99.6% to 90.6% in **Zn-L-2H**, in agreement with the observed increase in the emission intensity upon titration with Ag(I), due to the increased distance between the porphyrin planes.

The larger distance between the porphyrin planes in the Ag(I) complexed cages has been previously confirmed in a combined experimental and computational study on the analogous bis Zn-porphyrin cages.[141]

Furthermore, it is noteworthy to remark that the lifetime of the Zn-porphyrin component in [(**Zn-S-2H**)·Ag_4]$^{4+}$ is longer than that of the same unit in the more flexible [(**Zn-L-2H**)·Ag_4]$^{4+}$, indicating a closer disposition of the two units in the latter as it occurs for the uncomplexed cages and for the analogous Zn-porphyrin cages studied previously.[141,142]

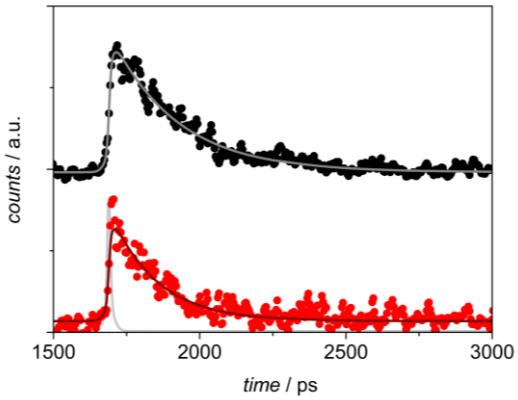

Figure 3.18. Luminescence decays in the 600-620 nm region for **Zn-S-2H** (black dots) and **Zn-L-2H** (red dots) added with 20 equivalents of AgOTf. The bi-exponential fittings are reported as lines. The excitation profile is shown in grey. Excitation at 560 nm (26 μJ/pulse).

Cl^- addition to Ag(I) complexes

Prior to the encapsulation of the guest, we tested the removal of Ag(I) coordinated to the triazole ligands through the addition of chloride (provoking the precipitation of the ions in the form of AgCl) to confirm the reversibility of the open/close process induced by the Ag(I) ions.

The addition of an excess of LiCl to both [(**2H-S-2H**)·Ag_4]$^{4+}$ and [(**Zn-S-2H**)·Ag_4]$^{4+}$ causes changes in the absorption and emission spectra. In the two cages, a decrease in intensity and a splitting of Soret band is observed in the absorption spectra (Figure 3.19a and Figure 3.20a), with a final spectrum similar to the one of the uncomplexed cage in both cases. This implies that the chloride anions effectively remove the Ag(I) ions and return the cage back to its original uncomplexed form. Regarding the emission features, a return to the original emission intensity is observed for the **2H-S-2H** cage (Figure 3.19b), but a further decrease is observed in its monometallated analogous **Zn-S-2H** (Figure 3.20b) probably due to the excess of Cl^- added. These data confirm the reversible size-tunable capacity of the cages **2H-S-2H** and **Zn-S-2H** upon the addition and removal of the effector Ag(I) ion.

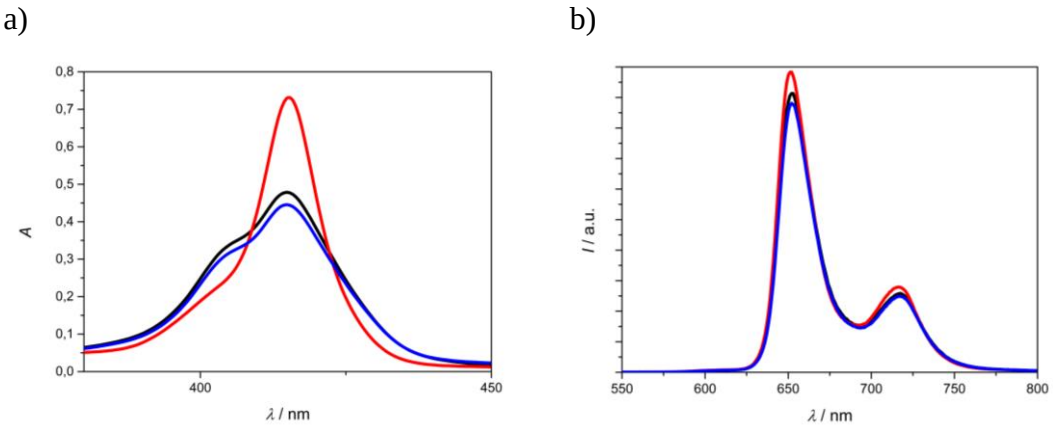

Figure 3.19. Absorption (**a**) and uncorrected emission spectra (λ_{exc} = 409 nm) (**b**) of CH_2Cl_2/MeOH (9:1) solutions containing **2H-S-2H** ($6.02 \cdot 10^{-7}$ M) (black), **2H-S-2H** added with Ag(I) (25 equivalents) (red) and **2H-S-2H** with Ag(I) added with an excess of Cl^- (300 equivalents) (blue).

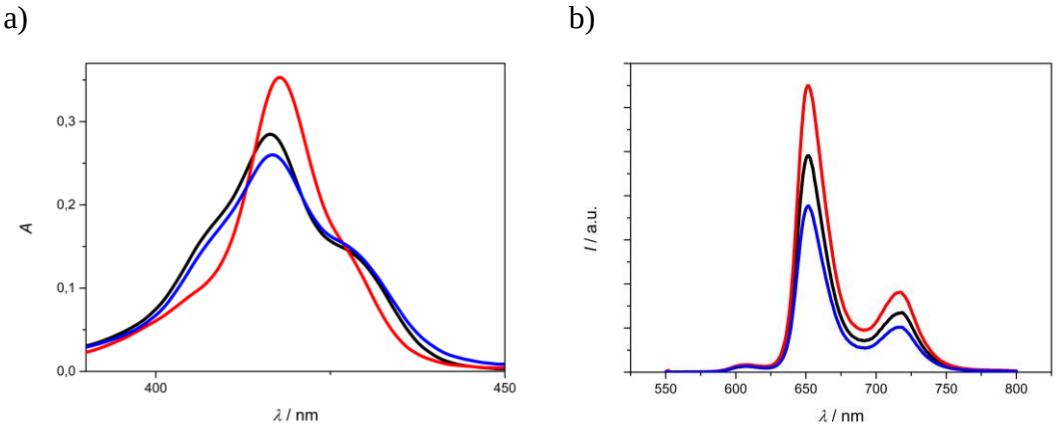

Figure 3.20. Absorption (**a**) and uncorrected emission spectra (λ_{exc} = 389 nm) (**b**) of CH_2Cl_2/MeOH (9:1) solutions containing **Zn-S-2H** ($4.39 \cdot 10^{-7}$ M) (black), **Zn-S-2H** added with Ag(I) (20 equivalents) (red) and **Zn-S-2H** with Ag(I) added with an excess of Cl^- (300 equivalents) (blue).

3.2.2. Complexation of ETH with Ag(I) complexed cages

After the characterization of the Ag(I) complexation of the four cages, that proved their size tunable capacity in the case of **2H-S-2H**, **Zn-S-2H** and **Zn-L-2H**, we selected the *short* cages for the study of their ability, once their cavity has been opened by the binding of silver ions, to work as hosts for the complexation of the ethionamide molecule.

Ethionamide (ETH) (Figure 3.21) has been firstly characterized from the photophysical point of view in the solvent mixture CH_2Cl_2/MeOH (9:1). It shows an absorption spectrum confined below 400 nm, with maximum at 290 nm (Figure 3.22), which does not interfere with the region of the Soret band of the host. Moreover, it was found to be non-emissive in the same solvent.

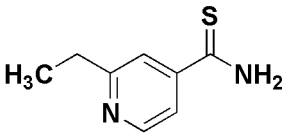

Figure 3.21. Structure of the guest molecule ethionamide.

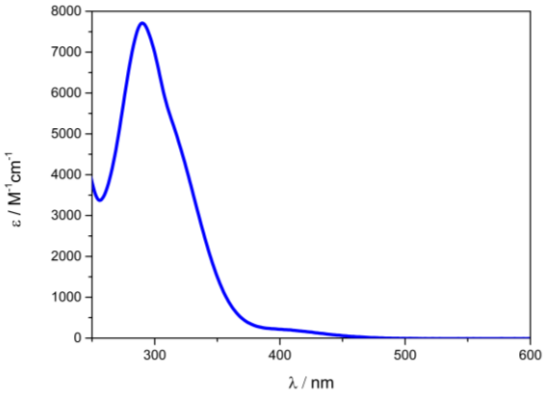

Figure 3.22. Absorption spectrum of ethionamide in CH_2Cl_2/MeOH (9:1).

The titration experiments for both cages [(**2H-S-2H**)·Ag_4]$^{4+}$ and [(**Zn-S-2H**)·Ag_4]$^{4+}$ with ETH have been carried out with the following procedure: i) 5-8·10^{-7} M CH_2Cl_2/MeOH (9:1) solutions of **2H-S-2H** and **Zn-S-2H** have been added with Ag(OTf) with the proper concentration to ensure a complete silver(I) complexation, ii) micro aliquots of an ETH stock solution prepared in the same solvent have been progressively added to the previous solutions. Absorption and emission spectra were recorded for each ETH addition.

2H-S-2H

The addition of increasing amounts of ethionamide to a [(**2H-S-2H**)·Ag_4]$^{4+}$ ($1.01\cdot10^{-6}$ M) solution in the range of 0-2 equivalents causes absorption changes as shown in Figure 3.23a. The Soret band decreases its intensity and recovers the splitting due to the exciton coupling observed in the uncomplexed cage, meanwhile, the Q band region remains unaltered without any significant changes. A possible explanation of this behavior comes from preliminary computational studies made in collaboration with Prof. Daidone's group**: the changes observed in the absorption spectra agrees with the coordination of the ethionamide guest to the Ag(I) ions coordinated to the lateral triazoles. This external coordination provokes the staking of the two porphyrins in a conformation closer to that of the uncomplexed cage, explaining the slight different shape in the Soret band between the ETH complexed cage and the uncomplexed one.

In the emission spectra (Figure 3.23b) collected upon excitation at 409 nm, isosbestic point for the absorption titration, a quenching process that reduce the emission intensity around 20% is observed. This process agrees with the closer conformation induced by the coordination of ETH with the Ag(I) ions, since the closeness of the porphyrin cores reduces their emission intensity.[142]

a) b)

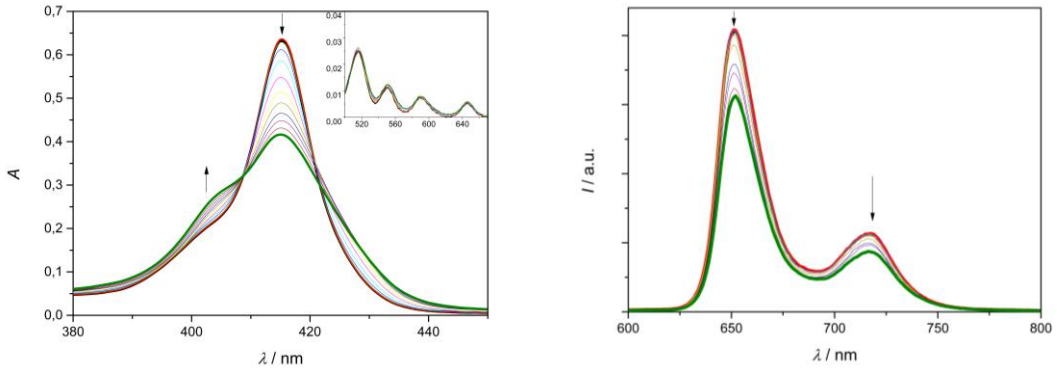

Figure 3.23. Absorption (a) and uncorrected emission spectra (λ_{exc} = 409 nm) (b) of CH_2Cl_2/MeOH (9:1) solution containing [(**2H-S-2H**)·Ag_4]$^{4+}$ ($1.01\cdot10^{-6}$ M) and increasing amounts of ETH (0-1.8 equivalents). Inset of (a): amplification of the Q-band regions (510-650 nm).

Zn-S-2H

Addition of increasing amounts of ETH to a [(**Zn-S-2H**)·Ag_4]$^{4+}$ ($6.02\cdot10^{-7}$ M) solution in the range of 0-8 equivalents causes absorption changes as shown in Figure 3.24a. Similar features to those of its analogous [(**2H-S-2H**)·Ag_4]$^{4+}$ are observed: a decrease of intensity and appearance of the splitting of the Soret band occur, while the Q-bands region remains unaltered. The same explanation can be applied for this case.

In the emission spectra (Figure 3.24b) collected upon excitation at 389 nm, isosbestic point of the absorption titration, a quenching process is also observed up to *ca*. 50%. This outcome can be explained by the hypothesis of the formation of a more closed upon complexation of ETH, where the porphyrin planes are reciprocally affecting their emission properties. Other events anyway cannot be excluded, and studies to clarify the process are ongoing.

a) b)

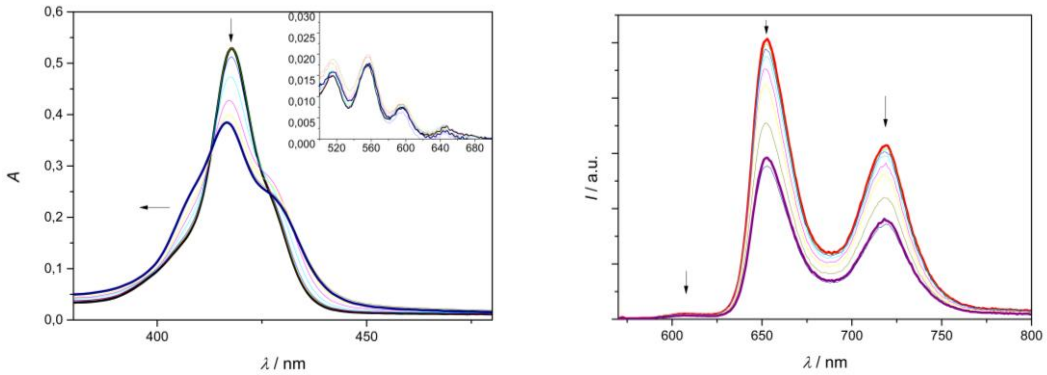

Figure 3.24. Absorption (a) and uncorrected emission spectra (λ_{exc} = 389 nm) (b) of CH_2Cl_2/MeOH (9:1) solutions containing [(**Zn-S-2H**)·Ag_4]$^{4+}$ ($6.02 \cdot 10^{-7}$ M) and increasing amounts of ETH (0-7.8 equivalents). Inset of (a): amplification of the Q-band regions (500-700 nm).

Due to the similarity of the final absorption spectra of the ETH-complexed cages and of the closed cages recovered with the addition of Cl^- ions, experiments performed to investigate the possible release of ETH upon the removal of Ag^+ with the addition of chloride did not produce significant results. The drug delivery event, if occurring, is not easily detected by optical techniques and NMR studies are ongoing to elucidate the processes.

3.3. Conclusions

The complexation process with Ag(I) of the four flexible covalent cages presented in Chapter 2 (**2H-S-2H**, **2H-L-2H**, **Zn-S-2H** and **Zn-L-2H**) has been studied by means of steady-state and time-resolved spectroscopy.

The effective coordination of Ag(I) ions to the lateral triazole ligands integrated in the linkers of **2H-S-2H**, **Zn-S-2H** and **Zn-L-2H** occurs within the range of 20-40 equivalents and provokes the opening of the cage cavities. The changes observed in the absorption spectra indicate that a separation of the porphyrin planes takes place since the reduction of the splitting of the Soret band implies a decrease of the coupling between the units. The features observed in the fluorescence titrations agree with the proposed mechanism.

Interestingly, a porphyrin core metalation process in competition with the complexation of the triazole moieties occurs for **2H-L-2H**. Thanks to MD simulations, it could be proposed that a more favorable orientation of the porphyrinic NH groups, compared to its analogous **2H-S-2H**, influences the metalation process. Indeed, the *long* cage's NH groups points towards the interior of the cage, leading to the exposure of the reactive lone pair of the nitrogen to the solvent enhancing the reactivity towards the binding of the Ag(I) ions. The particular orientation of these groups in **2H-L-2H** is permitted by the higher flexibility of the longer linkers.

The ability of **2H-S-2H** and **Zn-S-2H**, in their open conformation, to function as hosts in the formation of host-guest systems has been tested with the ETH molecule. The addition of ETH to Ag(I) complexes of the cages provokes changes in the absorption and emission spectra pointing to an increase of the exciton coupling, probably due to the lower distance between the porphyrin planes due to the complexation of ETH to the Ag(I) ions that induces a more constricted conformation of the cages. This thesis is supported by computational simulations.

3.4. Experimental

Spectroscopy grade CH_2Cl_2 and MeOH were from Merck and used as received. Silver trifluoromethanesulfonate (Ag(OTf)) was from Sigma-Aldrich. It has been stored under argon in a sealed vial in dark and dry conditions. Ag(OTf) solutions were used fresh and kept in the dark during the measurements. Ethionamide was used as received from TCI.

Absorption spectra were recorded with Perkin-Elmer Lambda 650 UV-VIS and Perkin-Elmer Lambda 950 UV-VIS-NIR spectrophotometers.

Emission spectra were collected with an Edinburgh FLS920 fluorimeter, equipped with a Peltier-cooled Hamamatsu R928 PMT (200-850 nm), and corrected for the wavelength dependent response.

Titration experiments were performed by incremental addition of micro aliquots of stock solution of Ag(OTf) (10^{-3} to 10^{-4} M) and ETH (10^{-3} to 10^{-4} M) to a solution of molecular cage or Ag(I)-complexed cage (5-8 · 10^{-7} M), respectively. The final added volume was kept below 10% of the total volume to avoid dilution of the cage. The experiments have been conducted avoiding light exposure of the solutions.

All the titrations were characterized by an early step where the addition of silver (5-10 equivalents) caused no changes in both absorption and emission features, attributed to an initial disaggregation process.

Addition of an excess of silver salt caused in all cases, except cage **2H-L-2H**, degradation of the compounds with a decrease in intensity of both absorption and emission bands.

Titration data have been analyzed with ReactLab Equilibira software[178] to determine the association constants.

Fluorescence lifetimes in the nanosecond range were detected by using an IBH Time Correlated Single Photon Counting apparatus with Nano-LED excitation at 465 nm. Analysis of the decay profiles against time was performed using the Decay Analysis Software DAS6 provided by the manufacturer.

Fluorescence lifetimes in the ps regime were measured by means of a Hamamatsu synchroscan streak-camera apparatus (C10910-05 main unit and M10911-01 synchroscan unit) equipped with an ORCA-Flash 4.0 V2 charge-coupled device (CCD) and an Acton spectrograph SP2358. As excitation source, a Newport Spectra Physics Solstice-F-1K-230 V laser system, combined with a TOPAS Prime (TPR-TOPAS-F) optical parametric amplifier (pulse width: 100 fs, 1 kHz repetition rate) was used, tuned at 560 nm. To reduce

photo-degradation, the pump energy on the sample was reduced to 26 μJ/pulse. Emission from the sample, collected at a right angle with a 1 mm slit, was focused by means of a system of lenses into the spectrograph slit. Streak images were taken in analog integration mode (100 exposures, exposure time: 2 s). The decays were measured over emission spectral ranges of 20–40 nm. HPD-TA 9.3 software from Hamamatsu was used for data acquisition and analysis. The overall time resolution of the system after deconvolution procedure was 1 ps.

Chapter 4: Photophysical Properties of a series of Acridinium-Zn(II) Porphyrin Conjugates

4.1. Introduction

4.1.1. Acridinium – Porphyrin Conjugates

The *N*-substituted acridinium unit constitutes a good building block for the construction of molecular architectures since it promotes guest binding properties and responds to chemical, redox or photonic stimuli. It can be functionalized either at 9- and *N*-positions from an acridone thanks to its available lone pair and ketone functional group,[181,182] and the substituents can tune its physico-chemical properties. Particularly, 9-aryl-*N*-methyl-acridinium (**ArAc**$^+$) displays multi-responsive properties based on two extreme resonance structures. The 9-phenylacridinium (**PhAc**$^+$), due to its resonance form shown on the right of Figure 4.1, displays halochromic and photochromic properties in an analogous way as pH-indicators do (like malachite green, phenolphthalein, bromothymol blue, etc.). In the resonance form shown on the left of Figure 4.1, the *N*-pyridinium core offers potential redox capacity.[183] In addition, acridinium molecules have the ability to interact with other aromatic compounds through π-π interactions, because of their relatively large aromatic character.

Due to its chemi-, photo- and electrochromic properties, the **ArAc**$^+$ motif has been included in several supramolecular structures as responsive unit. Nevertheless, the combination of porphyrins and acridiniums has not been widely explored, even though these units can offer interesting opportunities when they are conjugated.

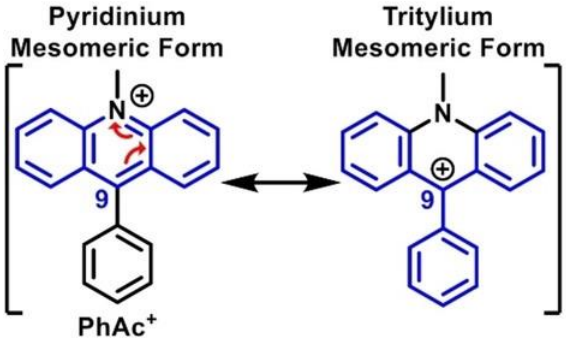

Figure 4.1. Resonance forms of the 9-phenyl-*N*-methyl-acridinium (**PhAc**$^+$) motif. Reproduced with permission of © 1999-2921 John Wiley & Sons, Inc.[183]

Kitagawa et al.[184] prepared bis-porphyrins-based water-soluble receptors interacting through π-donor/π-acceptor interactions with protonated acridine derivatives. Also, they

showed that the guest is stabilized by charge-transfer interactions between the porphyrin and the acridinium guest.[185] Ko et al.[186] synthesized cofacial zinc-porphyrin complexes that were effective receptors for acridinium ions, their preorganized configuration helped the guest to readily position itself in a favorable way for encapsulation.

Rath et al.[187] prepared a diethylpyrrole-bridged bisporphyrin receptor to encapsulate a fluorescent probe constituted by an acridinium ion (**AcH**$^+$). When the acridinium was encapsulated, its redox properties changed making it difficult to be reduced/oxidized. The fluorescence intensity of the complexed **AcH**$^+$ was severely quenched. The good overlap between the emission spectrum of the guest (energy donor) and the absorption spectrum of the host (energy acceptor) facilitated the efficient intermolecular energy transfer from the excited state of **AcH**$^+$ to the free base bisporphyrin. Hence, a photoinduced electron transfer from the excited state of bisporphyrin to **AcH**$^+$ upon 560 nm excitation, which was thermodynamically favorable, provoked as well the quenching of the guest's fluorescence. In this work, **AcH**$^+$ could act as either acceptor or donor depending on which chromophore was excited in the host-guest complex. Computational modeling located electron densities on the HOMOs and LUMOs that supported the formation of a charge-separated state in which the host acted as electron donor while the guest acted as electron acceptor in the complex.

Fukuzumi et al,[188] reported a system constituted by two cofacial free-base porphyrins linked by a flexible spacer able to host the acridinium ion (**AcH**$^+$) forming a π-complex. Photoinduced electron transfer from the host to the guest took place efficiently to form the charge separated state (**Host·$^+$-AcH·**) detected by laser flash photolysis. Later, they reported[189] a quantitative fluorescence sensor for $O_2^{\bullet-}$ constituted by a bis-acridinium-porphyrin triad (**Acr$^+$-H$_2$P-Acr$^+$**) (Figure 4.2). The acridinium ion was employed as electron acceptor and a photoinduced electron transfer from the porphyrin to the acridinium unit was revealed by femtosecond transient absorption. When the superoxide ion was added to a solution of the triad, the fluorescence intensity of the latter was enhanced. The electron transfer that takes place from the superoxide ion to the Acr$^+$ moiety, indeed, produces a two-electron-reduced species (**Acr$^{\bullet}$-H$_2$P-Acr$^{\bullet}$**) and inhibits the fluorescence quenching *via* the photoinduced process. The triad thus acts as an efficient fluorescence sensor for the superoxide ion.

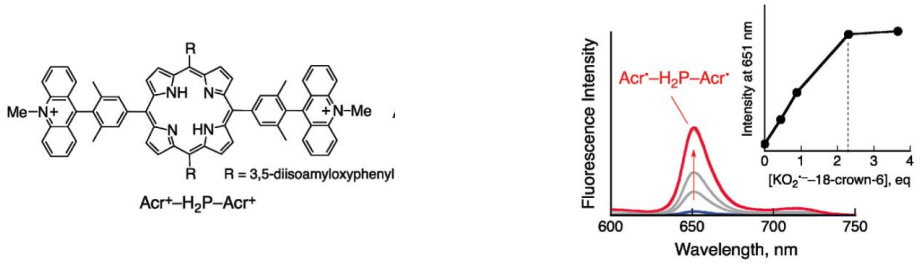

Figure 4.2. (Left) Structure of the (**Acr$^+$-H$_2$P-Acr$^+$**) triad. (Right) Fluorescence spectra observed in the titration of the triad with $KO_2^{\bullet-}$-18-crown-6. Reproduced with permission of © 2021 American Chemical Society.[189]

In view of exploring novel arrays based on porphyrins and acridinium units, several acridinidum-Zn(II) porphyrin conjugates were synthesised by Prof. Heitz's group* and the photophysical characterization of these systems is presented in this chapter.

Several conjugates have been explored: bisacridinium-Zn(II) porphyrin (**BisAcr Porph**), tetrakisacridinium-Zn(II) porphyrin (**TetraAcr Porph**), monoacridnium-Zn(II) porphyrin (**MonoAcr Porph**) and bisacridinium-Zn(II) bisporphyrin (**Tweezer**). These compounds aim to have interesting photophysical properties and to be active in Photodynamic Therapy (PDT) to treat cancer cells. Furthermore, the **Tweezer** can encapsulate a guest, turning it into a drug delivery system.

Part of the results presented in this chapter were published in 2021: *"Synthesis, electronic and photophysical properties of a bisacridinium-Zn(II) porphyrin conjugate"*, A. Edo-Osagie, D. Sánchez-Resa, D. Serillon, E. Bandini, C. Gourlaouen, H.P. Jacquot de Rouville, B. Ventura, V. Heitz, *Comptes Rendus Chimie*, **2021**, *24*, DOI: 10.5802/crchim.100.[190] The figures related to this publication are reproduced with permission of © 2019 – 2021 Centre Mersene, l'Acadèmie des sciences, et les auteurs.

4.2. Results and discussion

4.2.1. Bisacridinium-Zn(II) porphyrin conjugate

The photophysical study of the bisacridinium-Zn(II) porphyrin conjugate (**BisAcr Porph**) (Figure 4.3), and model compounds Zn-bisphenyl porphyrin (**Zn-bP**) and acridinium benzaldehyde (**Acr Benz**) (Figure 4.4) was performed in CH_3CN.

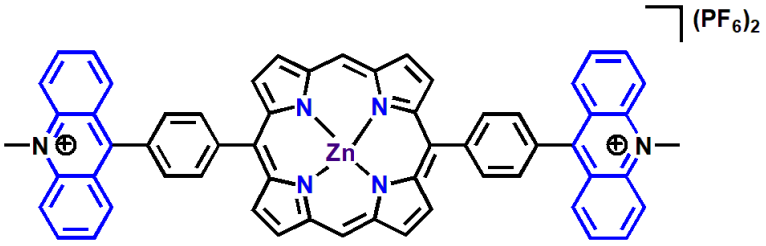

Figure 4.3. Structure of the bisacridinium-Zn(II) porphyrin conjugate (**BisAcr Porph**).[190]

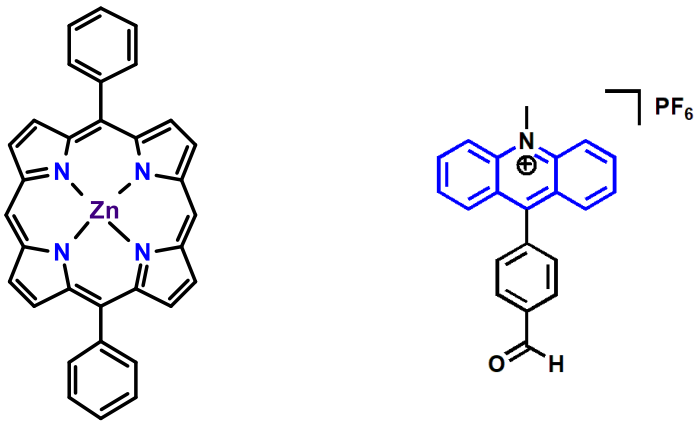

Figure 4.4. Structure of the models Zn-bisphenyl porphyrin (**Zn-bP**) (left) and acridinium benzaldehyde (**Acr Benz**) (right).[190]

Figure 4.5 displays the absorption spectrum of the conjugate compared with those of the models **Zn-bP** and **Acr Benz** and their weighted sum. The spectrum of the conjugate matches fairly well with the sum in the 280-400 nm region (acridinium benzaldehyde region), while the Q-bands of the porphyrin (500-600 nm) are slightly red-shifted with respect to the model **Zn-bP**, and the same occurs to the Soret band (400-450 nm) which presents a decrease in intensity and a broadening. Theoretical analysis proved that the observed absorption features correspond to the contribution of three electronic π-π* transitions either centered on the porphyrin or on the acridinium cores.[190]

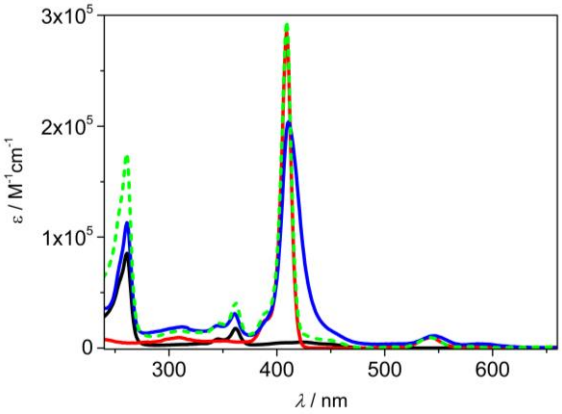

Figure 4.5. Absorption spectra of bisacridinium-porphyrin conjugate (**BisAcr Porph**) (blue), model compounds **Zn-bP** (red) and **Acr Benz** (black) and the sum of the spectrum of **Zn-bP** with twice the spectrum of **Acr Benz** (green dotted) in CH_3CN.[190]

Luminescence measurements were performed both at room temperature and 77 K in CH_3CN. **Acr Benz**, at room temperature, presents a broad emission spectrum with maximum at 515 nm, a quantum yield of 0.045 and an excited state lifetime of 1.73 ns, whereas **Zn-bP** shows emission maxima at 588 and 638 nm, ϕ_{fl} = 0.035 and τ = 2.30 ns (Figure 4.6 and Table 4.1).

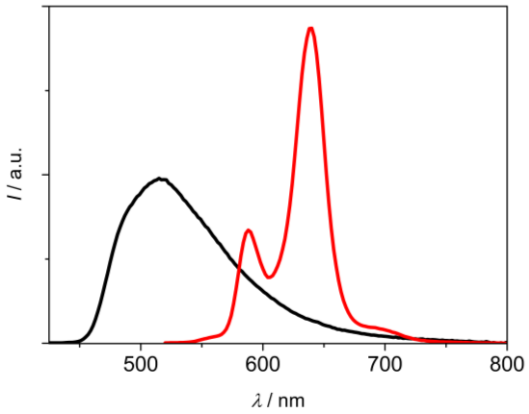

Figure 4.6. Corrected emission spectra of models **Acr Benz** (black) and **Zn-bP** (red) in CH_3CN at room temperature. The area below the curves is proportional to the emission quantum yield. Excitation at 400 nm for **Acr Benz** and at 520 nm for **Zn-bP**.[190]

On the contrary, the conjugate **BisAcr Porph** is barely emissive due to a strong quenching of both the acridinium and porphyrin units. Selective excitation of the porphyrin component in the conjugate at 543 nm resulted in an emission quantum yield below 10^{-4}, which represents less than 0.3% the yield of the model **Zn-bP** (Table 4.1). Excitation at 262 nm, where the acridinium unit is prevalently excited (*ca*. 96%), of isoabsorbing solutions of the **BisAcr Porph**, **Zn-bP** and **Acr Benz** was carried out to estimate the quenching of the acridinium units in the conjugate (Figure 4.7). The

porphyrin fluorescence intensity found in **BisAcr Porph** was below 4%, which would correspond to the direct excitation of the porphyrin in the array, corroborating the quenching already observed. The residual acridinium emission indicates a quenching higher than 99% of these units in the conjugate. These characteristics points to a very fast and efficient photoinduced process that depopulates the lowest single excited states of both components in the conjugate, most probably an electron transfer. This hypothesis is supported by transient absorption experiments described below.

Table 4.1. Emission data for models and conjugate in CH_3CN.[190]

		RT			77 K		
		λ_{max} (nm)[a]	ϕ_{em}[b]	τ (ns)[c]	λ_{max} (nm)[a]	τ (ns)[c]	E (eV)[d]
Acr Benz	Acr Benz[1]	515	0.045	1.73	471, 500	2.70 (20%), 16.6 (80%)	2.63
Zn-bP	Zn-bP[1]	588, 638	0.035	2.30	605, 648	2.31	2.05
	Zn-bP[3]				794	-	1.56
BisAcr Porph		590, 642[e]	$<1.0\cdot10^{-4}$[e]		-	-	-

[a]Emission maxima from corrected spectra. [b]Fluorescence quantum yields, measured with reference to **TPP** (*meso*-tetraphenylporphyrin) in aerated toluene as a standard for the porphyrin units and with reference to Coumarin 153 in ethanol for the acridinium units. [c]Fluorescence lifetimes in the nanosecond range, excitation at 465 nm for **Zn-bP** and at 368 nm for **Acr Benz**. [d]Energy of the excited state determined as the energy of the 0-0 emission band collected at 77 K. [e]Upon selective excitation of the Zn-porphyrin at 543 nm, the yield is below the minimum value measurable with steady-state experiments, i.e., $1.0\cdot10^{-4}$.

Although an electron transfer can explain the quenching, we could not exclude the possibility of an energy transfer from the acridinium unit towards the porphyrin singlet excited state, which is thermodynamically allowed (Figure 4.8) and supported by a non-zero overlap between the emission spectrum of the acridinium unit and the absorption spectrum of the porphyrin component (Figure 4.5 and Figure 4.6). To investigate the occurrence of photoinduced energy transfer, the excitation spectrum of **BisAcr Porph** was collected at 660 nm, wavelength at which only the emission of the porphyrin component is present, and compared to the absorption spectrum (Figure 4.9). Although the excitation spectrum is noisy, because of the weak emission, it displays the absorption bands of the porphyrin and lacks the characteristic absorption peaks of the acridinium unit at 262 and 362 nm. This result indicates that an energy transfer from the acridinium units to the central porphyrin unit does not take place in the conjugate, likely due to the competition with the ultrafast electron transfer process.

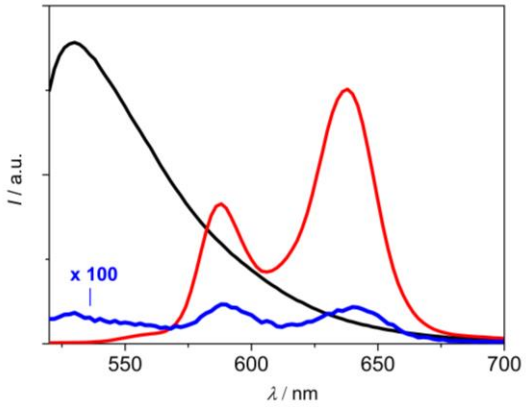

Figure 4.7. Uncorrected emission spectra of CH_3CN solutions of **BisAcr Porph** (blue) and models **Acr Benz** (black) and **Zn-bP** (red), isoabsorbing at 262 nm (A_{262} = 0.1). λ_{exc} = 262 nm. The blue spectrum has been multiplied by a factor of 100.[190]

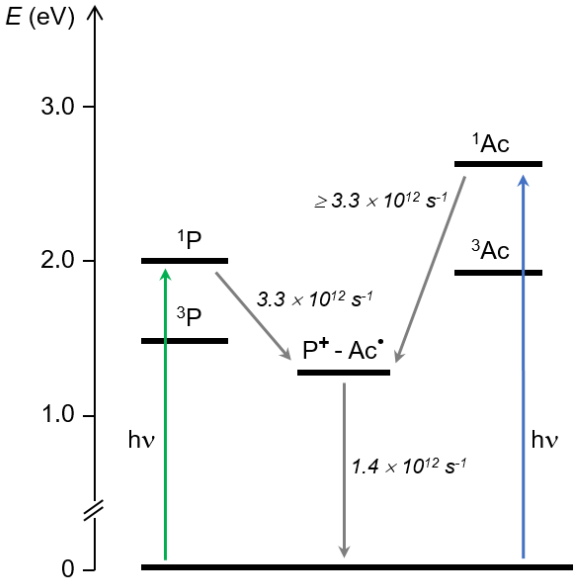

Figure 4.8. Energy level diagram and kinetics of the photoinduced processes occurring in the conjugate **BisAcr Porph** in CH_3CN. The singlet and triplet energy levels are taken from data of the present paper and from literature.[191] The energy of the charge separated state (1.39 eV) has been approximated as E_{ox}-E_{red} (with E_{ox} and E_{red} as "redox energy", expressed in eV), by considering the oxidation potential of the porphyrin unit (E_{ox} = +0.949 V versus SCE) and the reduction potential of the acridinium unit ($E_{1/2}$ = -0.442 V versus SCE) measured in DMF (N,N-dimethylformamide), whose polarity is similar to that of CH_3CN.[190]

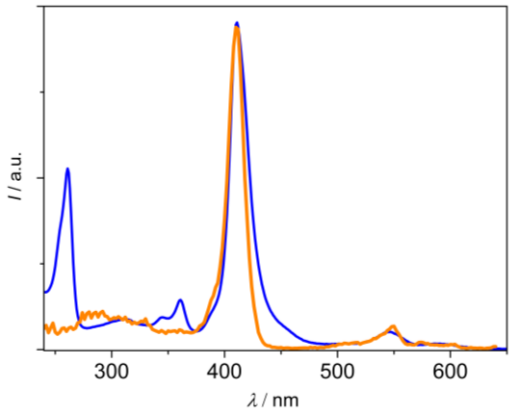

Figure 4.9. Arbitrarily scaled excitation (orange) and absorption (blue) spectra of **BisAcr Porph** in CH_3CN. λ_{em} = 660 nm.[190]

Emission measurements at 77 K revealed spectra with higher vibrational resolution for the models **Acr Benz** and **Zn-bP** (Figure 4.10) and phosphorescence at 794 nm was observed for **Zn-bP**. The conjugate **BisAcr Porph** is weakly emissive also at 77 K and its spectrum is barely collected because of scattering issues. The latter observation reveals that the decrease in temperature does not affect the efficiency of the quenching process that takes place within the components in the conjugate.

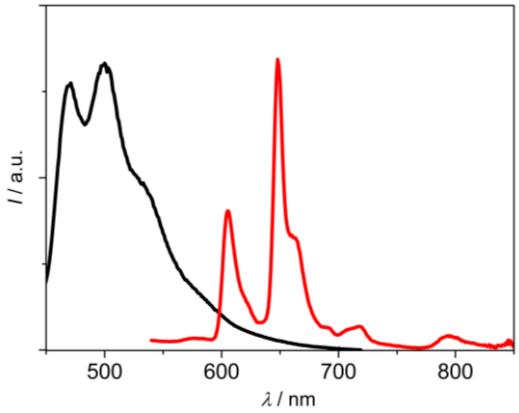

Figure 4.10. Normalized corrected emission spectra of models **Acr Benz** (black) and **Zn-bP** (red) in CH_3CN at 77K. Excitation at 362 nm for **Acr Benz** and at 520 nm for **Zn-bP**.[190]

To elucidate the fast photoinduced processes occurring in the conjugate, pump-probe transient absorption measurements with femtosecond resolution were carried out on **BisAcr Porph** and its models.

The excitation wavelengths selected were: 560 nm, where a selective population of the porphyrin singlet is achieved and 360 nm, where the acridinium units are prevalently excited. The peak at 262 nm of the acridinium is not experimentally accessible.

Figure 4.11a displays the time evolution of the transient spectrum of model **Zn-bP** upon excitation at 560 nm. The initial spectrum shows a positive band below 530 nm, ground state beaching at 542 and 580 nm and stimulated emission at 640 nm and it evolves into a new spectrum with a positive maximum at 463 nm, with clear isosbestic points. The kinetics was found to be equal to the fluorescence lifetime of the molecule (times profiles are reported in Figure 4.12), i.e. 2.3 ns; the final spectrum is attributed to the triplet state and the process is assigned to S1→ T1 intersystem crossing.

a) b)

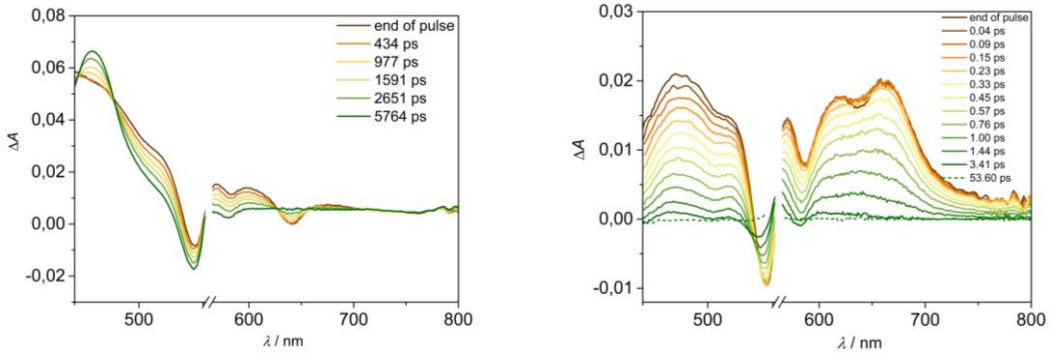

Figure 4.11. Transient absorption of a) **Zn-bP** and b) **BisAcr Porph** in CH_3CN at different delays. Excitation at 560 nm (A_{560} = 0.1, 0.2 cm optical path, 2 μJ/pulse).[190]

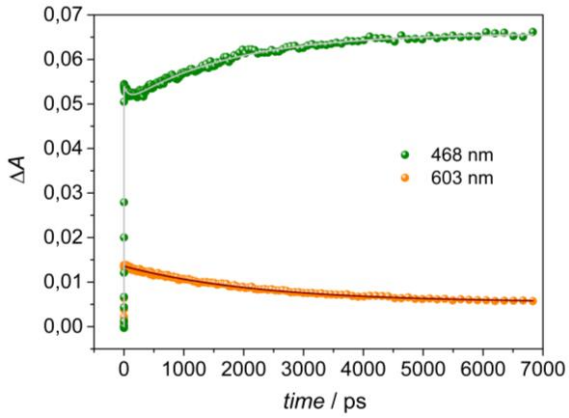

Figure 4.12. Time evolution of Δ*A* at the indicated wavelengths for **Zn-bP** in CH_3CN. Excitation at 560 nm (A_{560} = 0.1, 0.2 cm optical path, 2 μJ/pulse). The fittings are reported as lines.[190]

In the case of **BisAcr Porph** (Figure 4.11b), the results are completely diverse. The end of pulse spectrum shows maxima at 480, 520, 620 and 662 nm, as well as bleaching bands at 545 and 568 nm. In the region 620-600 nm an ultrafast signal rise, of the order of the time resolution of the system, is observed. This spectrum quickly decays, with a lifetime of 0.65 ps (Figure 4.13a). The observed transient spectrum can be safely ascribed to the charge separated state $\mathbf{P}^{+}$ - $\mathbf{Ac}^{\cdot}$ (P: porphyrin, Ac: acridinium), since the bands between 600 and 700 nm resembles those reported for a Zn-porphyrin cation,[192] and

bands at *ca*. 480 nm and 520 nm have been reported for the reduced species of *N*-alkyl substituted acridinium compounds.[188,193–195] The singlet excited state of the porphyrin is thus depopulated in *ca*. 0.3 ps to yield the charge separated state, which in turn lives less than 1 ps. It can be highlighted that the decay of the spectrum shows a second component, accounting for a very small fraction of the signal (*ca*. 2%), with a lifetime of *ca*. 32 ps (Figure 4.13b). This second component can be tentatively ascribed to a slower charge recombination occurring in a different conformation of the array or deriving from another minimum of the first excited singlet potential energy surface. This is consistent with the molecular flexibility in the excited state highlighted by theoretical analysis.[190]

a) b)

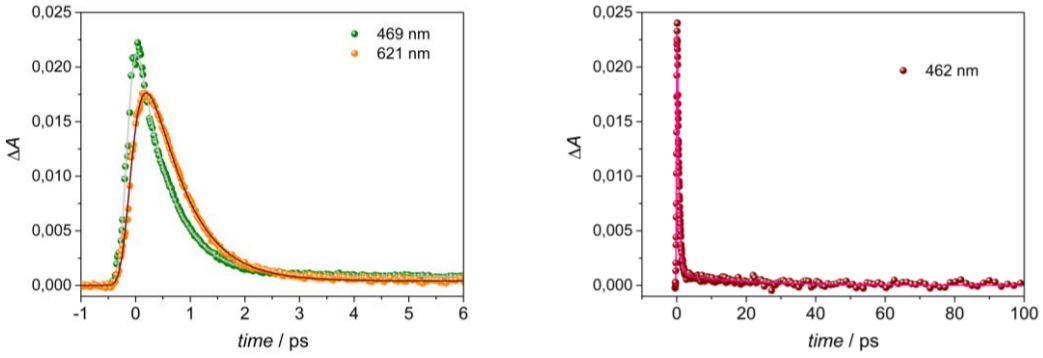

Figure 4.13. Time evolution of Δ*A* at the indicated wavelengths for **BisAcr Porph** in CH_3CN. Excitation at 560 nm (A_{560} = 0.1, 0.2 cm optical path, 2 μJ/pulse). a) Time scale: 0-6 ps; b) time-scale: 0-100 ps. The fittings are reported as lines.[190]

Transient absorption analysis upon excitation at 360 nm was performed for **BisAcr Porph** and models **Acr Benz** and **Zn-bP**. In **Acr Benz**, the initial formation of a signal with a risetime of 1 ps, ascribable to vibrational relaxation was observed (Figure 4.14a). The formed spectrum shows positive bands in the 450-510 nm and 630-800 nm regions, with maxima at 472 nm and 680 nm, and stimulated emission at 550 nm, red-shifted with respect to that detected from luminescence measurements due to the sum with the positive absorption bands. The signal decays with a lifetime of 1.6 ns (Figure 4.14b and Figure 4.15), and with defined isosbestic points, allowing to ascribe the process to S1 → T1 intersystem crossing, even if the spectral features of the triplet are hardly detectable. **Zn-bP** shows a behavior similar to that observed upon excitation at 560 nm, with intersystem crossing in 2.3 ns, but preceded by an initial fast evolution of 1 ps, ascribable to internal conversion (Figure 4.16 and Figure 4.17).[150]

a) b)

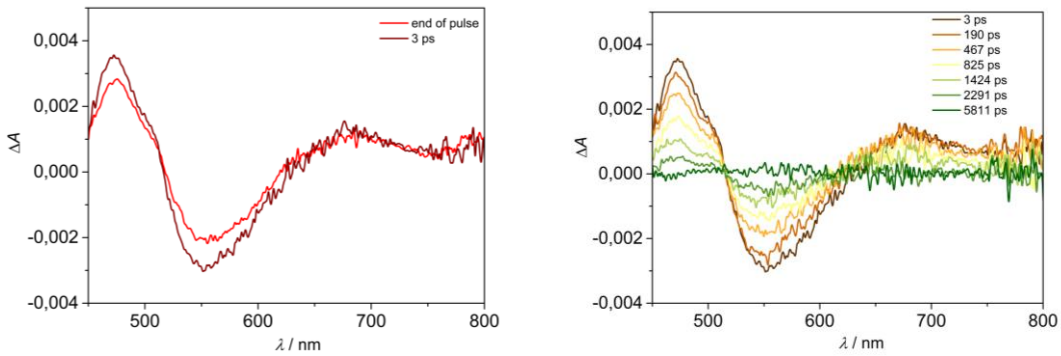

Figure 4.14. Transient absorbance of **Acr Benz** in CH_3CN at a) the end of pulse and after 3 ps, b) different delays. Excitation at 360 nm (A_{360} = 0.2, 0.2 cm optical path, 2 μJ/pulse).[190]

a) b)

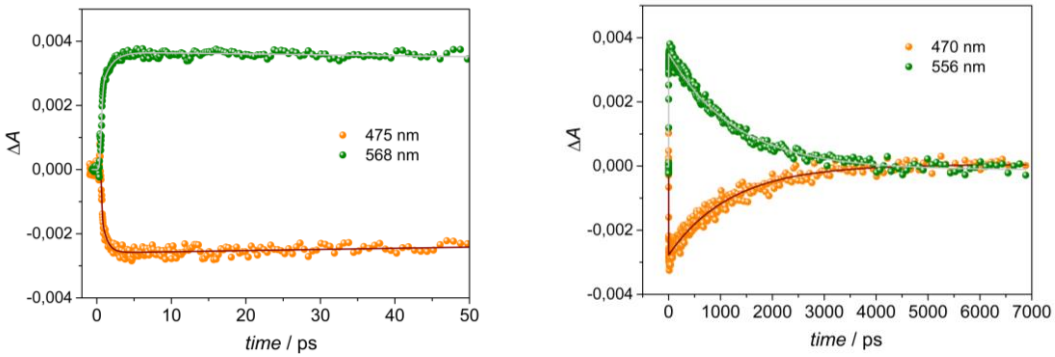

Figure 4.15. Time evolution of Δ*A* at the indicated wavelengths for **Acr Benz** in CH_3CN. Excitation at 360 nm (A_{360} = 0.2, 0.2 cm optical path, 2 μJ/pulse). a) Time scale: 0-50 ps; b) time-scale: 0-7000 ps. The fittings are reported as lines.[190]

a) b)

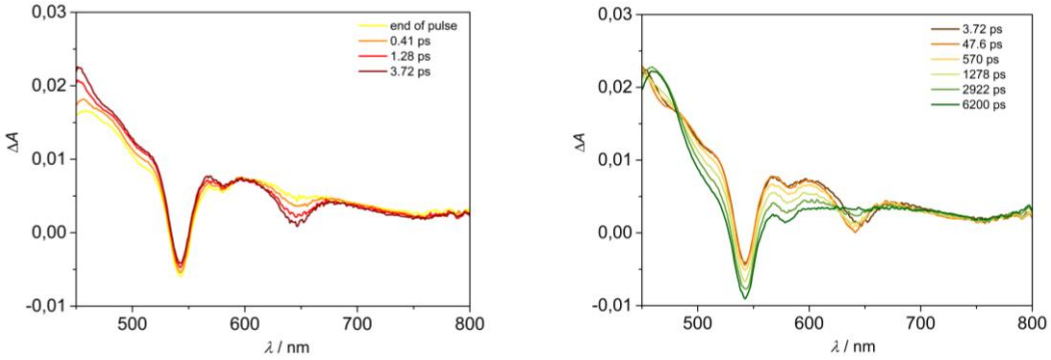

Figure 4.16. Transient absorbance of **Zn-bP** in CH_3CN at different delays: a) 0-3.72 ps; b) 3.72-6200 ps. Excitation at 360 nm (A_{360} = 0.2, 0.2 cm optical path, 2 μJ/pulse).[190]

a) b)

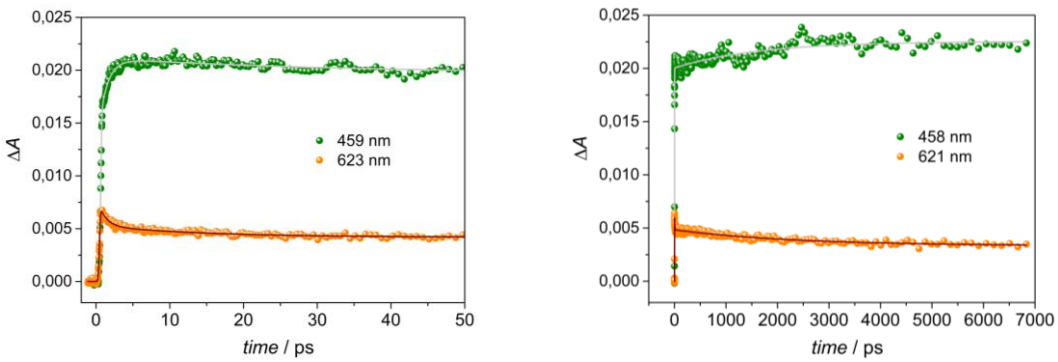

Figure 4.17. Time evolution of Δ*A* at the indicated wavelengths for **Zn-bP** in CH_3CN. Excitation at 360 nm (A_{360} = 0.2, 0.2 cm optical path, 2 μJ/pulse). a) Time scale: 0-50 ps; b) time-scale: 0-7000 ps. The fittings are reported as lines.[190]

The end of pulse spectrum of **BisAcr Porph** does not present any of the spectral characteristics of the singlet excited states absorption of the respective components but recall those observed upon excitation at 560 nm with clear features of the charge separated state (Figure 4.18). There is no evidence of signal formation, implying that the process upon prevalent excitation of the acridinium component occurs on an ultrafast scale (≤ 0.3 ps). The spectrum evolves quickly, almost disappearing with τ = 0.70 ps. A minor component, accounting for *ca*. 5% of the decay and with lifetime of 33 ps (Figure 4.18 and Figure 4.19) is detected, in agreement with that observed upon excitation of the porphyrin unit.

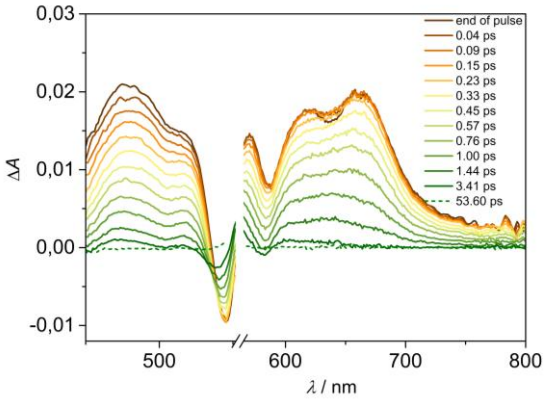

Figure 4.18. Transient absorbance of **BisAcr Porph** in CH_3CN at different delays. Excitation at 360 nm (A_{360} = 0.2, 0.2 cm optical path, 2 μJ/pulse).[190]

a) b)

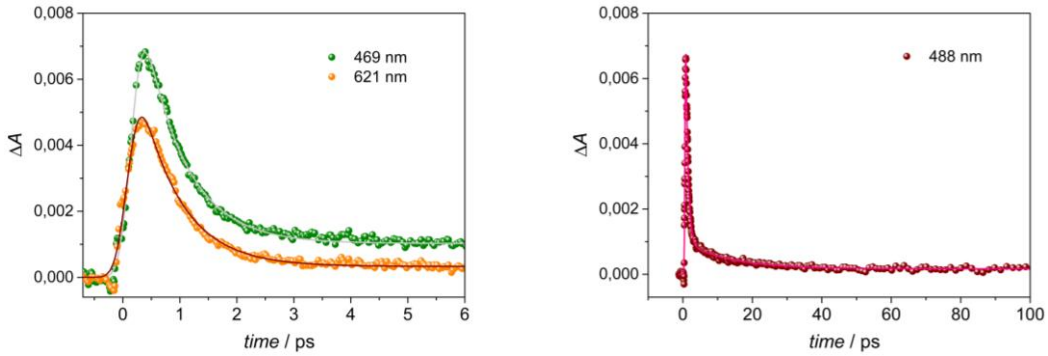

Figure 4.19. Time evolution of Δ*A* at the indicated wavelengths for **BisAcr Porph** in CH_3CN. Excitation at 360 nm (A_{560} = 0.2, 0.2 cm optical path, 2 μJ/pulse). a) Time scale: 0-6 ps; b) time-scale: 0-100 ps. The fittings are reported as lines.[190]

The observed photoinduced electron transfer process is, indeed, thermodynamically allowed upon excitation of both the porphyrin (Δ*G* = -0.66 eV) and the acridinium units (Δ*G* = -1.24 eV), as indicated in Figure 4.8 and, in the latter case, a higher energy gap account for the increased reaction rate, placing the reaction in the normal Marcus region.[196]

4.2.2. Tetrakisacridinium-Zn(II) porphyrin conjugate

Figure 4.20 display the structure of the tetrakisacridinium-Zn(II) porphyrin conjugate (**TetraAcr Porph**), in which the combination of porphyrin and acridinium units is further explored and can be useful for the development of future cage-type systems.

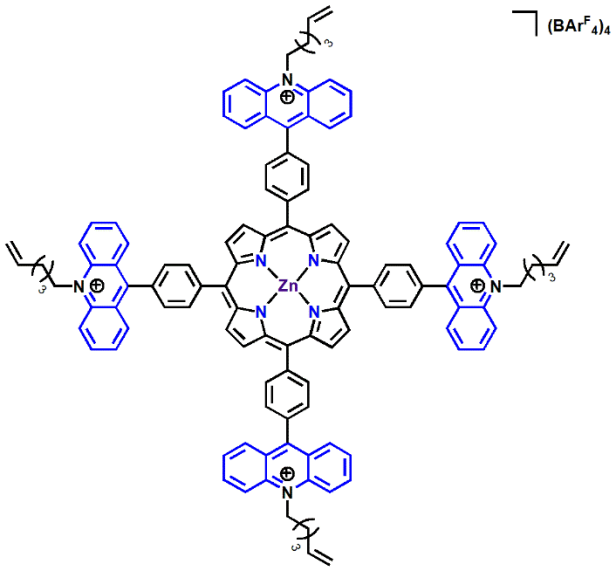

Figure 4.20. Tetrakisacridinium-Zn(II) porphyrin conjugate (**TetraAcr Porph**).

The photophysical properties of the **TetraAcr Porph** were studied in CH_3CN. **Zn-TPP** and **Acr Benz** were employed as models for comparison purposes and characterized in the same solvent.

Figure 4.21 shows the absorption spectrum of **TetraAcr Porph**, compared with the spectra of its corresponding models **Zn-TPP** and **Acr Benz** and their weighted sum. As in the **BisAcr Porph** case, the spectrum of the conjugate correlates fairly with the sum in the 280-400 nm region, which concerns the acridinium absorption region. Whereas the Q-bands (500-600 nm) are slightly red-shifted with respect to the **Zn-TPP** model, and also the Soret band is reduced in intensity, broadened and more red-shifted in comparison with its analogous **BisAcr Porph**, probably due to the presence of two more acridinium units. In analogy with **BisAcr Porph**, we can assume that the features in absorption are given by π-π* electronic transitions either centered on the porphyrin or on the acridinium cores.

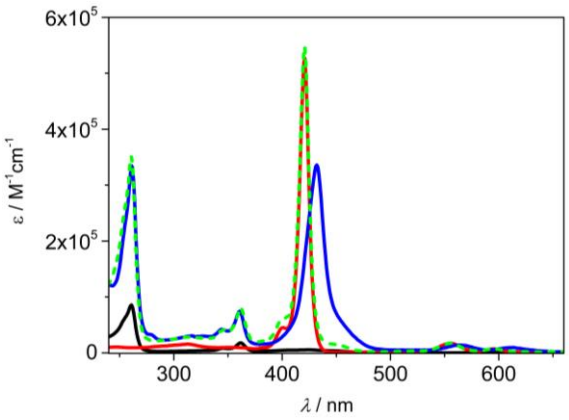

Figure 4.21. Absorption spectra of Tetrakisacridinium-Zn(II) porphyrin conjugate **TetraAcr Porph** (blue), model compounds **Zn-TPP** (red) and **Acr Benz** (black) and the sum of the spectra of **Zn-TPP** with four times the spectrum of **Acr Benz** (green dotted) in CH_3CN.

Luminescence measurements were carried out both at room temperature and at 77 K in CH_3CN. The luminescence properties of model **Acr Benz** have been already described. **Zn-TPP** displays emission maxima at 606 and 658 nm, ϕ_{fl} = 0.049 and τ = 2.15 ns (Figure 4.22 and Table 4.2), in agreement with literature reports.[197]

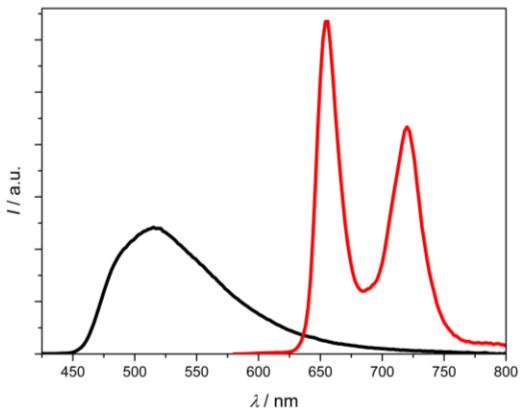

Figure 4.22. Corrected emission spectra of models **Acr Benz** (black) and **Zn-TPP** (red) in CH_3CN at room temperature. The area below the curves is proportional to the emission quantum yield. Excitation at 400 nm for **Acr Benz** and at 555 nm for **Zn-TPP**.

As observed for the **BisAcr Porph** conjugate, the tetrakisacridinium derivative displays strong quenching in both the acridinium and porphyrin units.

Upon excitation at 543 nm, in the porphyrin domain, a quantum yield less than 10^{-4} was found for **TetraAcr Porph**, representing less than 0.3% of the yield of the **Zn-TPP** model (Table 4.2). As shown in Figure 4.23, the major contribution to the emission spectrum of this conjugate comes from the acridinium moiety.

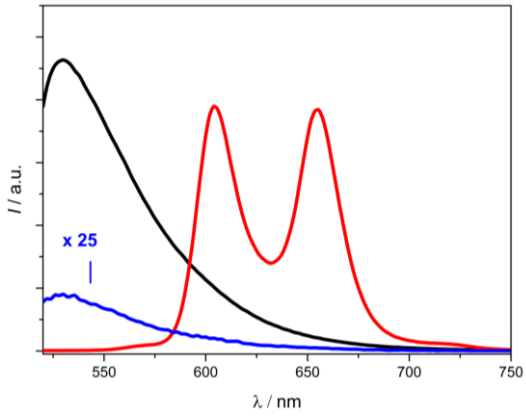

Figure 4.23. Uncorrected emission spectra of CH_3CN solutions of **TetraAcr Porph** (blue) and models **Acr Benz** (black) and **Zn-TPP** (red), isoabsorbing at 262 nm (A_{262} = 0.1). λ_{exc} = 262 nm. The blue spectrum has been multiplied by a factor of 25.

As carried out for the **BisAcr Porph**, in order to estimate the quenching of the acridinium units in the **TetraAcr Porph** conjugate, excitation of isoabsorbing solutions of the conjugate, the **Zn-TPP** and **Acr Benz** models at 262 nm (where the acridinium is prevalently excited) was performed (Figure 4.23).

For the conjugate, we found that the residual porphyrin fluorescence was below the 2% of the **Zn-TPP** emission, percentage which corresponds to the direct excitation of the

porphyrin unit in the array, confirming the quenching already observed and also displayed in the **BisAcr Porph** case. Regarding the acridinium emission, quenching by ≥ 99% was observed. This corresponds to a very fast and efficient photoinduced process that depopulates the lowest single excited state of both components in the array, like an electron transfer, which will be detailed below.

Table 4.2. Emission data for models and conjugate in CH_3CN.

		RT			77 K		
		λ_{max} (nm)[a]	ϕ_{em}[b]	τ (ns)[c]	λ_{max} (nm)[a]	τ (ns)[c]	E (eV)[d]
Acr Benz	Acr Benz[1]	515	0.045	1.73	471, 500	2.70 (20%), 16.6 (80%)	2.63
Zn-TPP	Zn-TPP[1]	606, 658	0.049	1.78	606, 652	2.15	2.05
	Zn-TPP[3]					-	
TetrakAcr Porph		590, 650[e]	$<1.0\cdot10^{-4}$[e]	-	-	-	-

[a]Emission maxima from corrected spectra. [b]Fluorescence quantum yields, measured with reference to **TPP** (*meso*-tetraphenylporphyrin) in aerated toluene as a standard for the porphyrin units and with reference to Coumarin 153 in ethanol for the acridinium units. [c]Fluorescence lifetimes in the nanosecond range, excitation at 465 nm for **Zn-TPP** and at 368 nm for **Acr Benz**. [d]Energy of the excited state determined as the energy of the 0-0 emission band collected at 77 K. [e]Upon selective excitation of the Zn-porphyrin at 543 nm, the yield is below the minimum value measurable with steady-state experiments, i.e., $1.0\cdot10^{-4}$.

To analyze the occurrence of a possible energy transfer process in the conjugate, we collected the excitation spectrum of **TetraAcr Porph** at 660 nm, where only the emission of the porphyrin component is present, and compared to the absorption spectrum (Figure 4.24). The excitation spectrum recollected displays the absorption bands of the porphyrin, even if with noise due to the weakness of the emission signal, and lacks the characteristic absorption peaks of the acridinium unit at 262 and 362 nm. With these data, we can conclude that energy transfer from the acridinium units to the central porphyrin does not occur in the conjugate, probably due to the competition with an ultrafast electron transfer process.

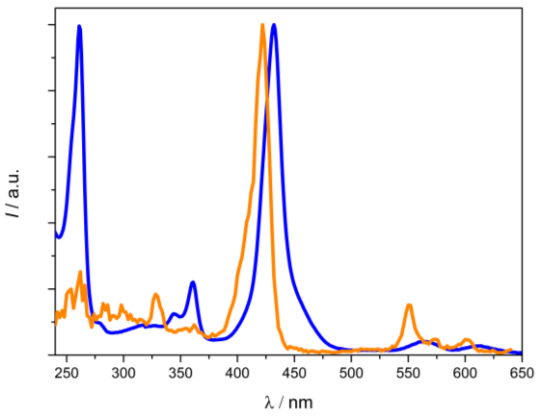

Figure 4.24. Arbitrarily scaled excitation (orange) and absorption (blue) spectra of **TetraAcr Porph** in CH_3CN. λ_{em} = 660 nm.

Emission measurements at 77 K show features similar to those observed at room temperature for the **Acr Benz** model and for **Zn-TPP** (Figure 4.25) with higher vibrational resolution. On the contrary, for the conjugate, the emission is very weak also at low temperature and its spectrum is hard to detect due to scattering issues that affect this measurement. This result leads to conclude that the decrease in temperature does not affect the efficiency of the quenching process occurring within the components of the array.

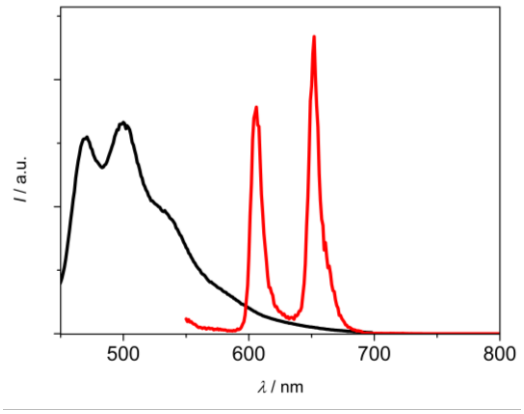

Figure 4.25. Normalized corrected emission spectra of models **Acr Benz** (black) and **Zn-TPP** (red) in CH_3CN at 77K. Excitation at 362 nm for **Acr Benz** and at 520 nm for **Zn-TPP**.

As in the case of **BisAcr Porph**, pump-probe transient absorption measurements with femtosecond resolution were performed on **TetraAcr Porph** and the models **Zn-TPP** and **Acr Benz** (previously described). The chosen excitation wavelengths were the same, i.e. 560 nm for the selective excitation of the porphyrin and 360 nm, where the acridinium unit is prevalently excited.

The time evolution of the transient absorption spectrum of the model **Zn-TPP** obtained upon excitation at 560 nm is displayed in Figure 4.27a. The initial spectrum presents a positive band below 530 nm, ground state bleaching at *ca*. 560 and 598 nm and stimulated emission at 658 nm. This spectrum evolves into a new spectrum with a positive maximum at 468 nm, with clear isosbestic points at 487 and 645 and 677 nm. The kinetics reflects the fluorescence lifetime of the molecule (the time profiles are reported in Figure 4.26): the decay and the rise are fitted with a lifetime of 1.7 ns, which is close to the fluorescence lifetime of 1.78 ns (Table 4.2); the final spectrum is thus attributed to the triplet state and the process is assigned to S1 → T1 intersystem crossing.

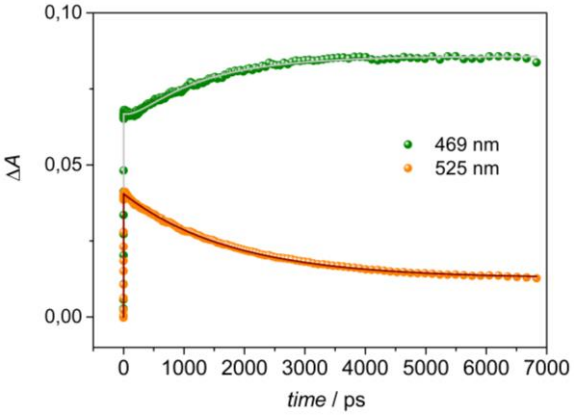

Figure 4.26. Time evolution of Δ*A* at the indicated wavelengths for **Zn-TPP** in CH_3CN. Excitation at 560 nm (A_{560} = 0.2, 0.2 cm optical path, 2 µJ/pulse). The fittings are reported as lines.

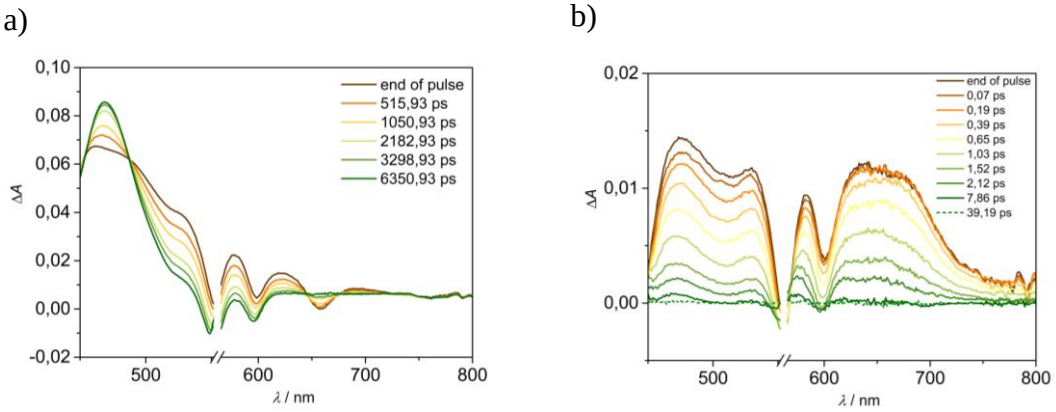

Figure 4.27. Transient absorbance of a) **Zn-TPP** and b) **TetraAcr Porph** in CH_3CN at different delays. Excitation at 560 nm (A_{560} = 0.2, 0.2 cm optical path, 2 µJ/pulse).

On the contrary, for the **TetraAcr Porph** conjugate the end-of-pulse spectrum (Figure 4.27b) differs from those of the models and is similar to the one of **BisAcr Porph**. The spectrum presents broad absorption bands between 450 and 750 nm, overlaid with ground state bleaching bands at *ca*. 560 and 600 nm. In the region 630-680 nm an ultrafast signal rise, of the order of the time resolution of the system, is observed. This spectrum

quickly decays, with a lifetime of 0.92 ps (Figure 4.28a). The observed transient spectrum can be ascribed, again, to the charge separated state $\mathbf{P^+}$ - $\mathbf{Ac^{\cdot}}$. The singlet excited state of the porphyrin is thus depopulated in *ca.* 0.33 ps to yield the charge separated state, which in turn lives about 1 ps (0.92 ps). It can be noticed that the decay of the spectrum shows a second component in the region 450-500 nm, accounting for a very small fraction of the signal (*ca*. 4%), with a lifetime of *ca*. 23 ps (Figure 4.28b). This second component can be tentatively ascribed, as before, to a slower charge recombination occurring in a different conformation of the array, or deriving from another minimum of the first excited singlet potential energy surface.

a) b)

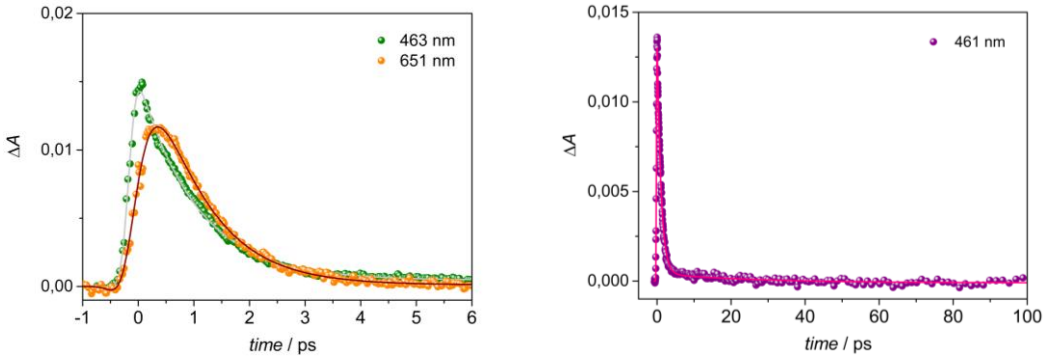

Figure 4.28. Time evolution of Δ*A* at the indicated wavelengths for **TetraAcr Porph** in CH_3CN. Excitation at 560 nm (A_{560} = 0.2, 0.2 cm optical path, 2 µJ/pulse). a) Time scale: 0-6 ps; b) time-scale: 0-100 ps. The fittings are reported as lines.

Transient absorption analysis with excitation at 360 nm has been performed for **TetraAcr Porph** and models **Acr Benz** and **Zn-TPP**. Model **Acr Benz** has been already described, **Zn-TPP** shows a similar behavior to the one observed upon excitation at 560 nm, with intersystem crossing occurring in 1.78 ns, but preceded by an initial fast evolution of 1.87 ps, ascribable to internal conversion (Figure 4.29 and Figure 4.30).[150]

a) b)

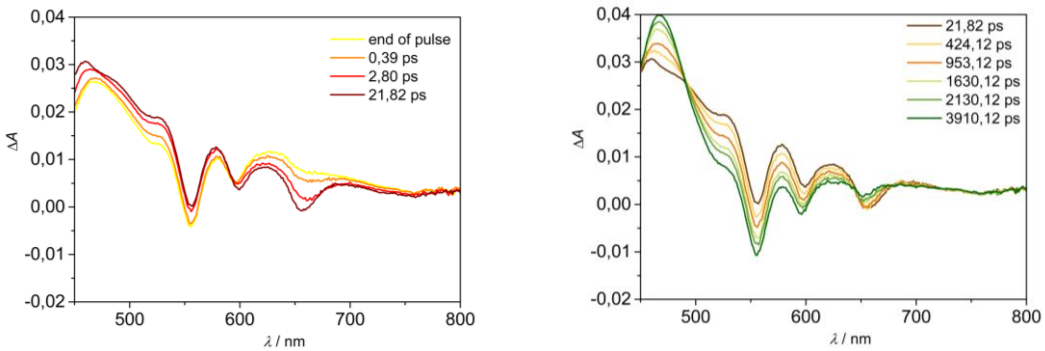

Figure 4.29. Transient absorbance of **Zn-TPP** in CH_3CN at different delays: a) 0-21.8 ps; b) 21.8-3900 ps. Excitation at 360 nm (A_{360} = 0.2, 0.2 cm optical path, 2 µJ/pulse).

a) b)

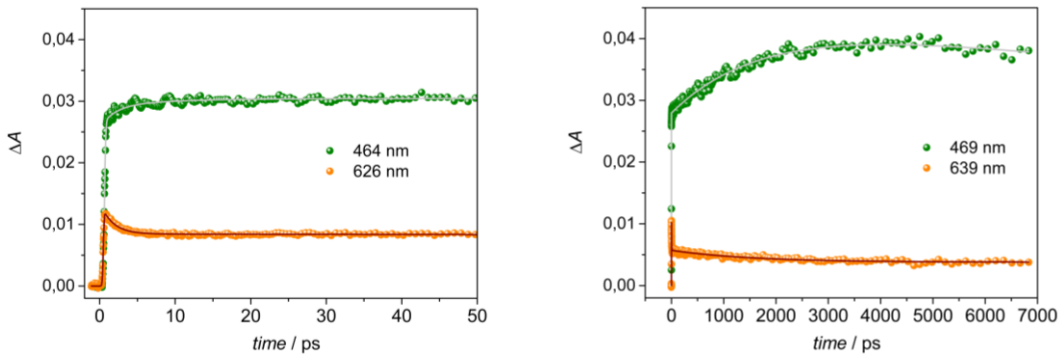

Figure 4.30. Time evolution of Δ*A* at the indicated wavelengths for **Zn-TPP** in CH_3CN. Excitation at 360 nm (A_{360} = 0.2, 0.2 cm optical path, 2 μJ/pulse). a) Time scale: 0-6 ps; b) time-scale: 0-100 ps. The fittings are reported as lines.

The end-of-pulse spectrum of **TetraAcr Porph** does not present any of the spectral features of the singlet excited states absorption of the respective components, but recall those observed upon excitation at 560 nm with clear features of the charge separated state (Figure 4.32). There is no evidence of signal formation, implying that the process, upon prevalent excitation of the acridinium component, occurs on an ultrafast scale (≤ 0.3 ps). The spectrum evolves quickly, almost disappearing with τ = 1.03 ps. A minor component, accounting for *ca.* 15% with a lifetime of 21.9 ps (Figure 4.31b and Figure 4.32) is detected, in agreement with that observed upon excitation of the porphyrin unit.

a) b)

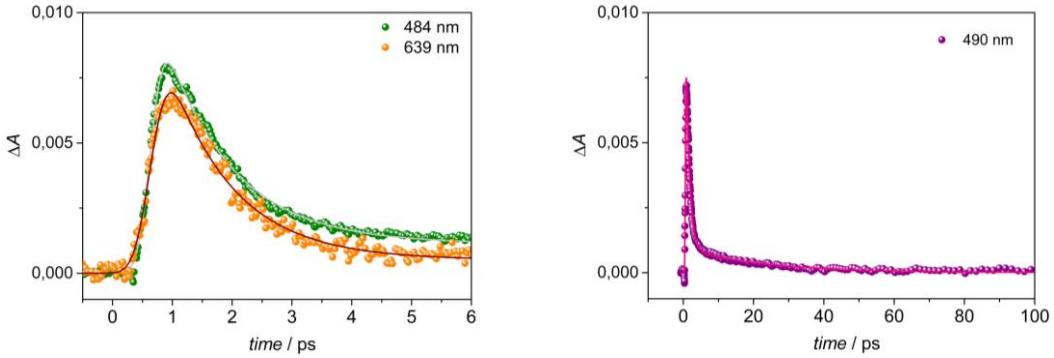

Figure 4.31. Time evolution of Δ*A* at the indicated wavelengths for **TetraAcr Porph** in CH_3CN. Excitation at 360 nm (A_{360} = 0.2, 0.2 cm optical path, 2 μJ/pulse). a) Time scale: 0-6 ps; b) time-scale: 0-100 ps. The fittings are reported as lines.

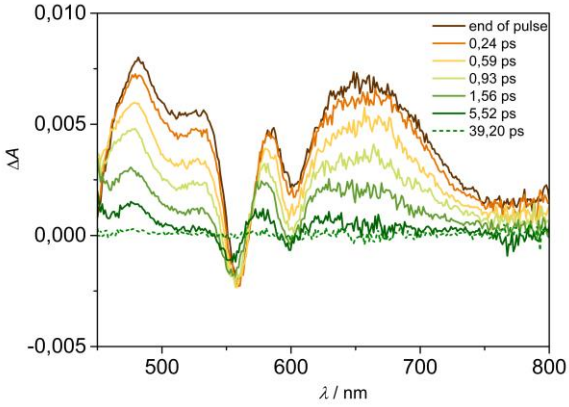

Figure 4.32. Transient absorbance of **TetrakAcr Porph** in CH_3CN at different delays. Excitation at 360 nm (A_{360} = 0.2, 0.2 cm optical path, 2 µJ/pulse).

4.2.3. Monoacridinium-Zn(II) porphyrin and bisacridinium-Zn(II) bisporphyrin conjugates

In this section, we describe the photophysical study of the Bisacridinium-Zn(II)-bisporphyrin conjugate (**Tweezer**) that can function as a molecular receptor thanks to the rotational freedom of the alkyl linkers between the two acridinium units, and of its model, the Monoacridinium-Zn(II) porphyrin conjugate (**MonoAcr Porph**). Their structures are presented in Figure 4.33.

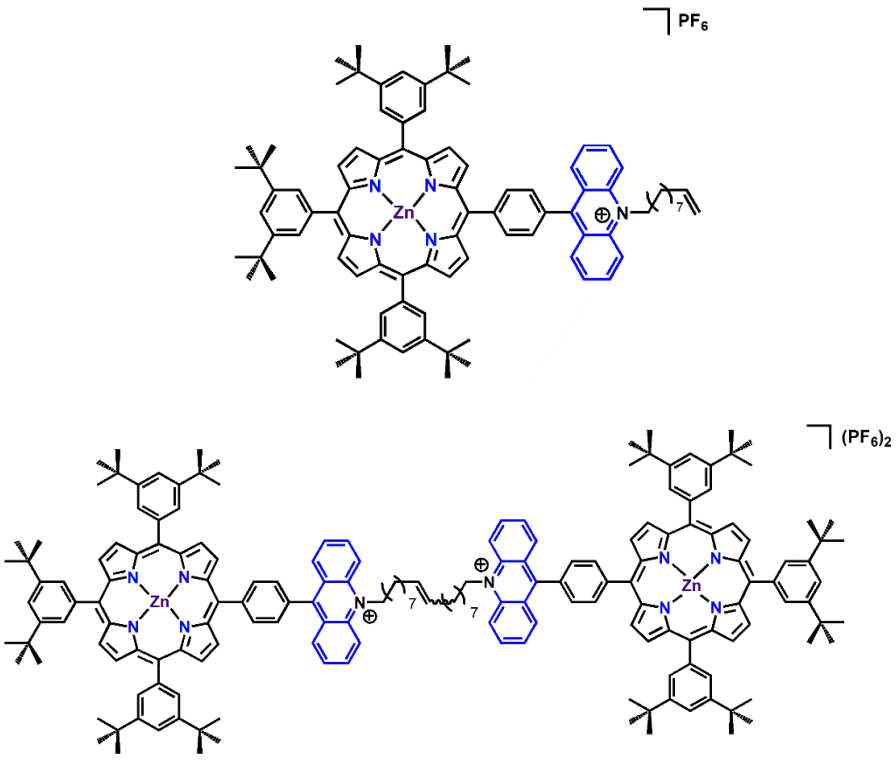

Figure 4.33. Monoacridinium-Zn(II) porphyrin (**MonoAcr Porph**) (top) conjugate and Bisacridinium-Zn(II)-bisporphyrin conjugate (**Tweezer**) (bottom).

The absorption spectrum of the Monoacridinium-Zn(II) porphyrin conjugate (**MonoAcr Porph**), together with the sum of the spectra of the models, is presented in Figure 4.34a. We can observe a reasonable correlation between the spectrum of the conjugate and the weighted sum of the spectra of the models in all regions. Only for the Soret band we observe that it is decreased and slightly red-shifted with respect to the sum of the spectra of the models.

Figure 4.34b shows the spectrum of the **Tweezer** compared with twice the spectrum of **MonoAcr Porph**. The spectra perfectly correlate in all regions except for the Soret band, which in the tweezer is slightly decreased in intensity, probably due to electronic interactions between the two porphyrin planes.

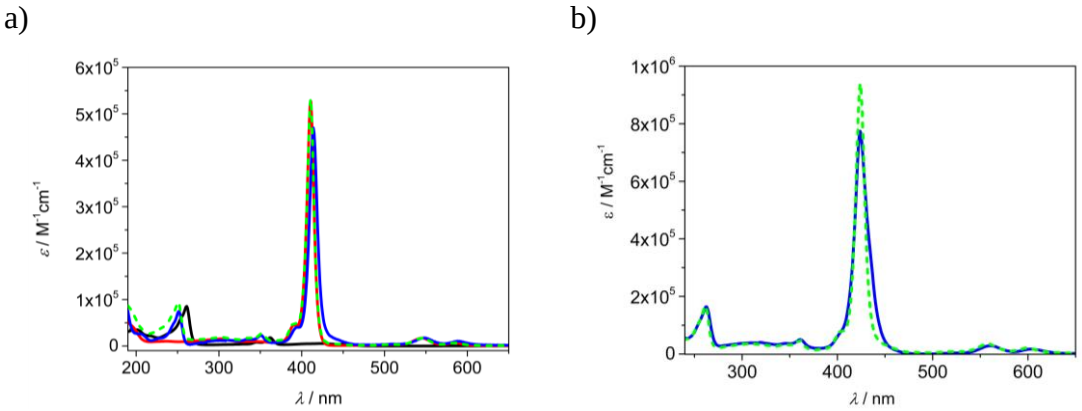

Figure 4.34. a) Absorption spectra of Monoacridnium-Zn(II) porphyrin conjugate **MonoAcr Porph** (blue), models compound **Zn-TPP** (red) and **Acr Benz** (black) and the sum of the spectrum of **Zn-TPP** with one time the spectrum of **Acr Benz** (green dotted) in CH_3CN. b) Absorption spectrum of Bisacridinium-Zn(II)-bisporphyrin conjugate **Tweezer** (blue) and the sum of twice the spectrum of **MonoAcr Porh** (green dotted) in CH_3CN.

As observed for the **BisAcr** and **TetraAcr Porph** conjugate, the **MonoAcr Porph and Tweezer** display strong luminescence quenching for both the acridinium and porphyrin units.

Indeed, low quantum yields values ($\leq 10^{-4}$) upon excitation of the porphyrin at 543 nm were found (Table 4.3).

As carried out for the **BisAcr** and **TetraAcr Porph**, in order to estimate the quenching of the acridinium units in the conjugates, excitation of isoabsorbing solutions of the conjugates, and the **Zn-TPP** and **Acr Benz** models, at 262 nm was performed. The results are shown in Figure 4.35.

a) b)

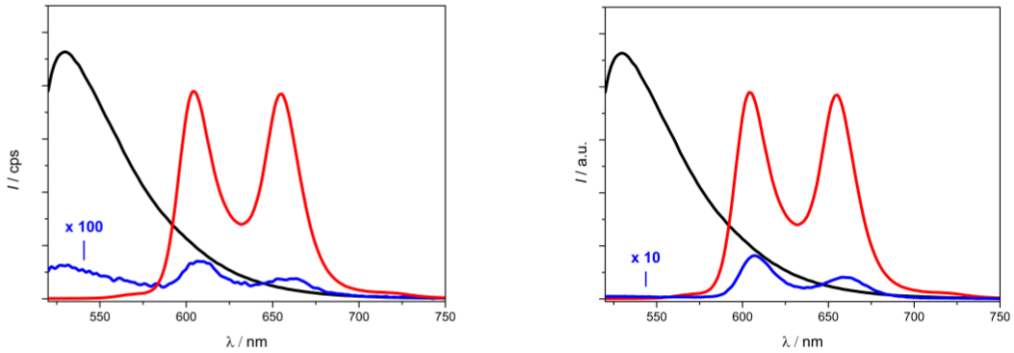

Figure 4.35. a) Uncorrected emission spectra of CH_3CN solutions of **MonoAcr Porph** (blue) and models **Acr Benz** (black) and **Zn-TPP** (red), isoabsorbing at 262 nm (A_{262} = 0.1) λ_{exc} = 262 nm. The blue spectrum has been multiplied by a factor of 100. b) Uncorrected emission spectra of CH_3CN solutions of **Tweezer** (blue) and models **Acr Benz** (black) and **Zn-TPP** (red), isoabsorbing at 262 nm (A_{262} = 0.1) λ_{exc} = 262 nm. The blue spectrum has been multiplied by a factor of 10.

For these two derivatives, the residual porphyrin fluorescence was below 2% of the model **Zn-TPP** emission as well as the acridinium emission presents a quenching higher than 99%. As indicated before, this matches with a fast and efficient photoinduced process, likely an electron transfer, which will be explained below.

Table 4.3. Emission data for conjugates in CH_3CN at room temperature.

		λ_{max} (nm)[a]	ϕ_{em}[b]
MonoAcr Porph	MonoAcr Porph[1]	608, 664	$<1.0\cdot10^{-4}$[e]
Tweezer	Tweezer[1]	608, 662	$<1.0\cdot10^{-4}$[e]

[a]Emission maxima from corrected spectra. [b]Fluorescence quantum yields, measured with reference to **TPP** (*meso*-tetraphenylporphyrin) in aerated toluene as a standard. [e]Upon selective excitation of the Zn-porphyrin at 543 nm, the yield is below the minimum value measurable with steady-state experiments, i.e., $1.0\cdot10^{-4}$.

To analyze the occurrence of a possible energy transfer process in this series, we collected excitation spectrum of the conjugates at 660 nm, where only the emission of the porphyrin component is present, and compared to the absorption spectrum (Figure 4.36). In the excitation spectra of **MonoAcr Porph** and **Tweezer** the absorption bands of the porphyrin are present while the characteristics absorption peaks of the acridinium unit at 262 and 362 nm are lacking. With these data, we can conclude that energy transfer from the acridinium units to the central porphyrin does not occur in the conjugates, probably due to the competition with an ultrafast electron transfer process.

a) b)

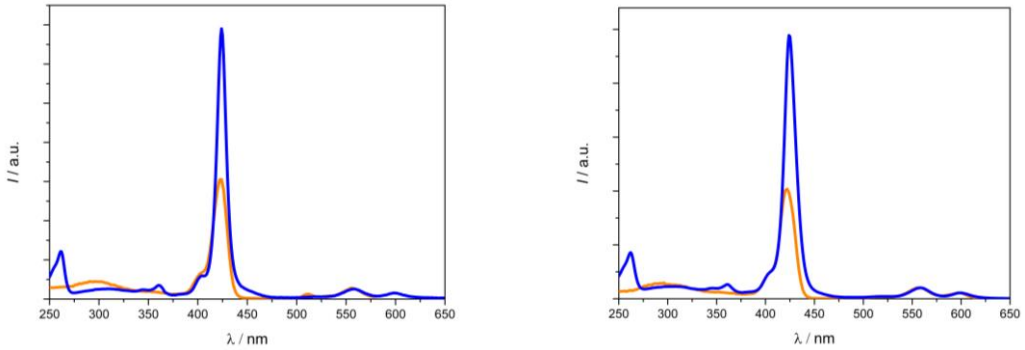

Figure 4.36. Arbitrarily scaled excitation (orange) and absorption (blue) spectra of a) **MonoAcr Porph** and b) **Tweezer** in CH_3CN. λ_{em} = 660 nm.

The emission spectra at 77 K for the **MonoAcr Porph** and **Tweezer** conjugates were hard to detect as well, indicating that the quenching process occurring in these arrays is as efficient as observed before for the **BisAcr** and **TetraAcr Porph**.

As in the case of **BisAcr** and **TetraAcr Porph**, pump-probe transient absorption measurements with femtosecond resolution were performed on the **MonoAcr Porph** and **Tweezer** conjugates, as well as for the models **Zn-TPP** and **Acr Benz** (previously described). The chosen excitation wavelengths were the same, i.e. 560 nm for the selective excitation of the porphyrin and 360 nm, where the acridinium unit is prevalently excited.

Excitation at 560 nm of the **MonoAcr Porph** and **Tweezer** yields the spectra displayed in Figure 4.37. For both, we can observe the same features already seen in the other conjugates. The end-of-pulse spectra of **MonoAcr Porph** and **Tweezer** (Figure 4.37) shows maxima at 470, 530, 628 and 678 nm, as well as bleaching bands at 558 and 598 nm. In the region 620-660 nm an ultrafast signal rise, of the order of the time resolution of the system or below, is observed. These spectra quickly decay, with a lifetime of 0.80 and 1 ps respectively (Figure 4.38a and Figure 4.39a). These spectra can be ascribed to the charge separated state $\mathbf{P^+}$ **-** $\mathbf{Ac^{\cdot}}$ (P: porphyrin, Ac: acridinium). The singlet excited state of the porphyrin in **MonoAcr Porph** and **Tweezer** is thus depopulated in *ca*. 0.36 ps and ≤ 0.30 ps, respectively to yield the charge separated state, which in turns lives 0.80 and 1 ps, respectively. It can be noticed that the decay of the spectra shows a second component, accounting for a very small fraction of the signal (*ca*. 3% and 8%), with a lifetime of *ca*. 20.4 and 19.4 ps, respectively (Figure 4.38b and Figure 4.39b). This second component can be tentatively ascribed, in analogy with the other systems, to a slower charge recombination occurring in a different conformation of the

array, or deriving from another minimum of the first excited singlet potential energy surface.

a) b)

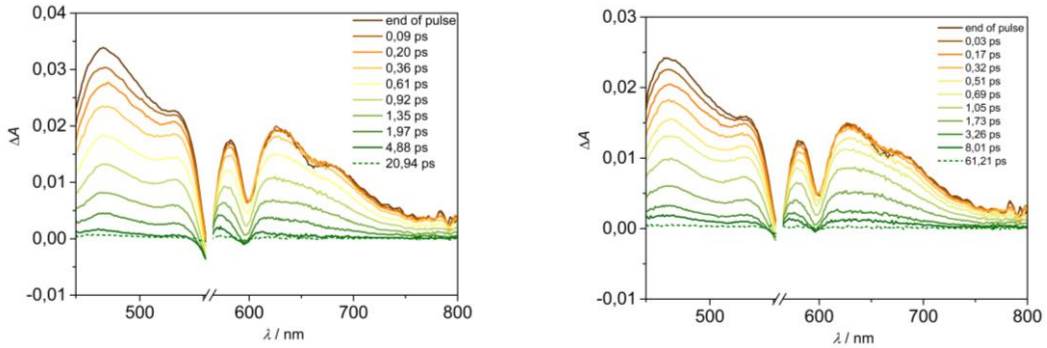

Figure 4.37. Transient absorbance of a) **MonoAcr Porph** and b) **Tweezer** in CH_3CN at different delays. Excitation at 560 nm (A_{560} = 0.2, 0.2 cm optical path, 2 µJ/pulse).

a) b)

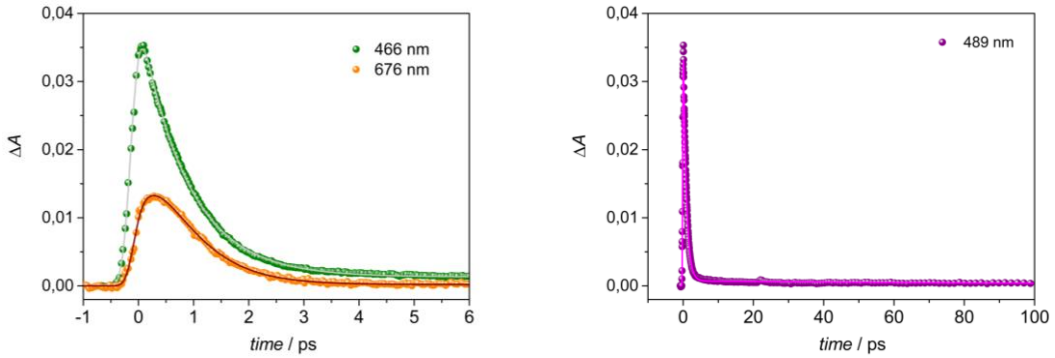

Figure 4.38. Time evolution of Δ*A* at the indicated wavelengths for **MonoAcr Porph** in CH_3CN. Excitation at 560 nm (A_{560} = 0.2, 0.2 cm optical path, 2 µJ/pulse). a) Time scale: 0-6 ps; b) time-scale: 0-100 ps. The fittings are reported as lines.

a) b)

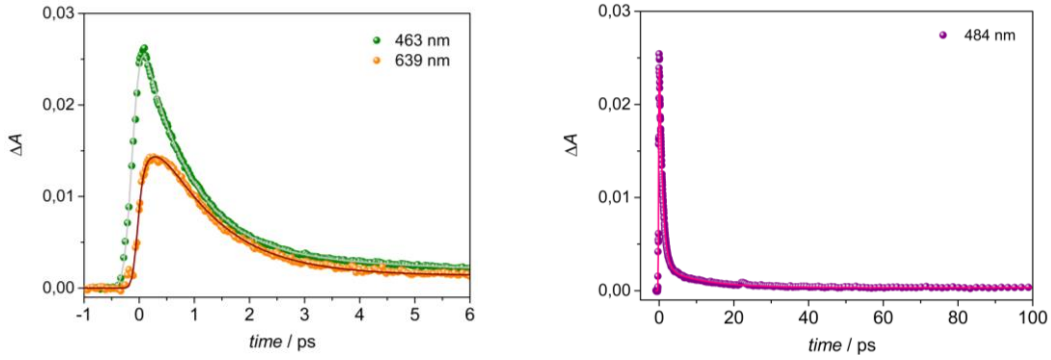

Figure 4.39. Time evolution of Δ*A* at the indicated wavelengths for **Tweezer** in CH_3CN. Excitation at 560 nm (A_{560} = 0.2, 0.2 cm optical path, 2 µJ/pulse). a) Time scale: 0-6 ps; b) time-scale: 0-100 ps. The fittings are reported as lines.

The same experiments were carried out with excitation of 360 nm. The end-of-pulse spectrum of both conjugates (Figure 4.40) does not present any of the spectral features of the singlet excited states absorption of the respective components, but recalls the ones observed upon excitation at 560 nm, with clear features of the charge separated state. A risetime of the order of the time resolution of the system (≤ 0.30 ps) is observed in the region 600-670 nm for **MonoAcr Porph** and all over the spectral range for the **Tweezer**. These spectra evolve quickly, almost disappearing with τ = 0.79 and 1.00 ps for the **MonoAcr Porph** and the **Tweezer**, respectively. A minor component, accounting for *ca*. 5% and 15% of the decay and with a lifetime of 19 and 13 ps, respectively (Figure 4.41b and Figure 4.42b), is detected, in agreement with that observed upon excitation of the porphyrin unit.

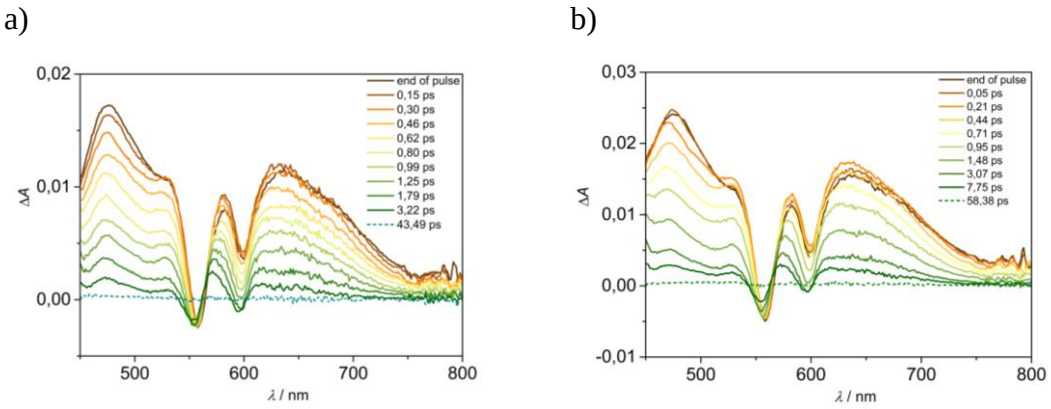

Figure 4.40. Transient absorbance of a) **MonoAcr Porph** and b) **Tweezer** in CH_3CN at different delays. Excitation at 360 nm (A_{360} = 0.2, 0.2 cm optical path, 2 µJ/pulse).

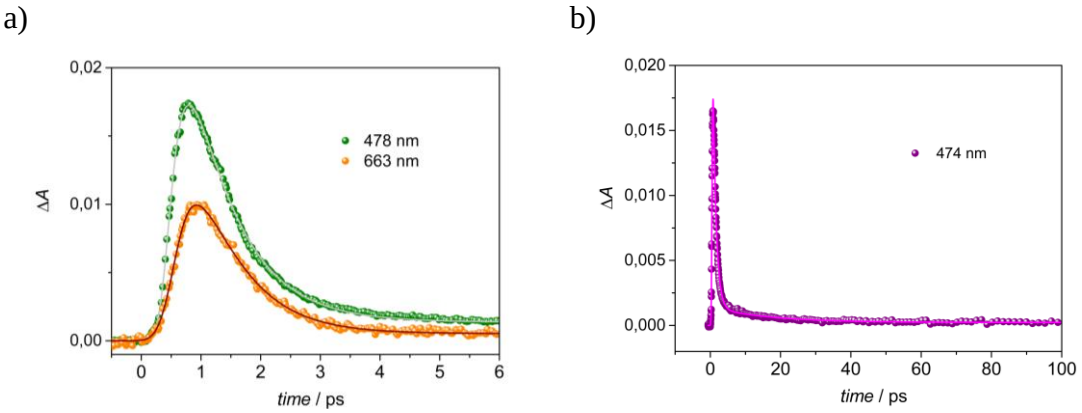

Figure 4.41. Time evolution of Δ*A* at the indicated wavelengths for **MonoAcr Porph** in CH_3CN. Excitation at 360 nm (A_{360} = 0.2, 0.2 cm optical path, 2 µJ/pulse). a) Time scale: 0-6 ps; b) time-scale: 0-100 ps. The fittings are reported as lines.

a) b)

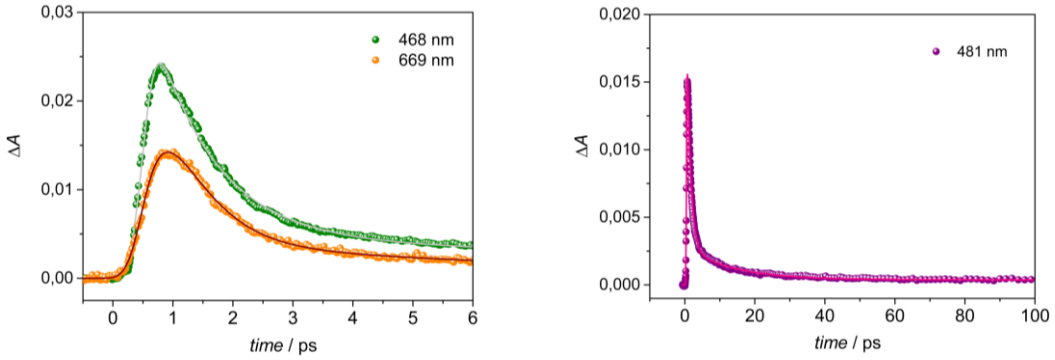

Figure 4.42. Time evolution of Δ*A* at the indicated wavelengths for **Tweezer** in CH_3CN. Excitation at 360 nm (A_{360} = 0.2, 0.2 cm optical path, 2 μJ/pulse). a) Time scale: 0-6 ps; b) time-scale: 0-100 ps. The fittings are reported as lines.

4.3. Conclusions

It can be concluded that acridinium units, when linked to porphyrins, are photoactive moieties that adduce interesting properties to the array. Comparison of the absorption spectra of the conjugates with those of the models led to observe variations in the spectra of the arrays, mainly in the Soret region. Porphyrin and acridinium centered transitions are responsible for the observed red-shift of the Soret and Q-bands of the porphyrin, as indicated by theoretical calculations performed for the **BisAcr Porph** case.

The strong fluorescence quenching observed in all the conjugates for both the porphyrin and the acridinium units is due to an ultrafast photoinduced electron transfer process. Transient absorption analysis showed that a charge separated state is formed, with similar kinetics for all the derivatives of the order of 0.3 ps, and it decays rapidly with a lifetime of *ca*. 1 ps. Besides, an energy transfer process from the acridinium units to the porphyrin core was excluded.

Photodynamic therapy studies with the conjugates presented in this chapter to treat cancer cells are currently ongoing in collaboration with Dr. Arno Wiehe (Biolitec research GmbH, Germany). Furthermore, the **Tweezer** is being tested as a valid host for the complexation of a tetrapyridyl porphyrin guest in collaboration with Prof. Heitz.

4.4. Experimental

Spectroscopic grade CH_3CN was from Merck and used as received.

Absorption spectra were recorded with a Perkin–Elmer Lambda 650 UV-vis spectrophotometer.

Emission spectra were collected with an Edinburgh FLS920 fluorimeter, equipped with a Peltier-cooled Hamamatsu R928 PMT (280–850 nm). The spectra were corrected for the wavelength-dependent phototube response, unless otherwise stated. Fluorescence quantum yields were evaluated from the area of the luminescence spectra, corrected for the photomultiplier response, with reference to *meso*-tetraphenylporphyrin (TPP) in aerated toluene (ϕ_{Fl} = 0.11)[198] for the porphyrin components and to Coumarin 153 in ethanol (ϕ_{Fl} = 0.544)[199] for the acridinium units. Measurements at 77K were performed with the same fluorimeter, making use of Pyrex tubes dipped in liquid nitrogen in a quartz Dewar. Excitation spectra were recorded with the same fluorimeter.

Emission lifetimes in the nanosecond range were determined by using an IBH time-correlated single-photon counting apparatus with a nanoLED excitation source at 465 nm and 368 nm.

Pump-probe transient absorption measurements were performed with an Ultrafast Systems HELIOS (HE-VIS-NIR) femtosecond transient absorption spectrometer by using, as excitation source, a Newport Spectra Physics Solstice-F-1K-230 V laser system, combined with a TOPAS Prime (TPR-TOPAS-F) optical parametric amplifier (pulse width: 100 fs, 1 kHz repetition rate) tuned at 360 nm and 560 nm. The overall time resolution of the system is 300 fs. Air-equilibrated solutions in 0.2 cm optical path cells were analyzed under continuous stirring. To reduce photo-degradation, the pump energy on the sample was reduced to 2 μJ/pulse. Surface Xplorer V4 software from Ultrafast Systems was used for data acquisition and analysis. The 3D data surfaces were corrected for the chirp of the probe pulse prior to analysis.

Estimated errors are 10% on transient absorbance lifetimes, 10% for luminescence lifetimes, 10% for molar absorption coefficients and 10% on quantum yields.

Chapter 5: Methodology

5.1. Absorption Spectra[200]

The absorption of radiant energy is associated to an electronic transition, meaning that the extra-energy of the photon induces the promotion of an electron from an orbital at lower energy to an orbital at a higher energy level. Each molecule has its own characteristic absorption spectrum since the energetic order and separation of the orbitals are unique for each molecule.

Since molecules present vibrational and rotational energy levels for each electronic state, for each single electronic level many transitions are possible to different vibrational and/or rotational energy levels, therefore, the absorption spectra will be constituted by bands of different width (Figure 5.1). The two fundamental characteristics of a band are its position and its intensity. The position of the band is defined by the wavelength of its maximum intensity (λ_{max}) and therefore the energy connected to that electronic transition can be calculated with the Planck equation (1.2).

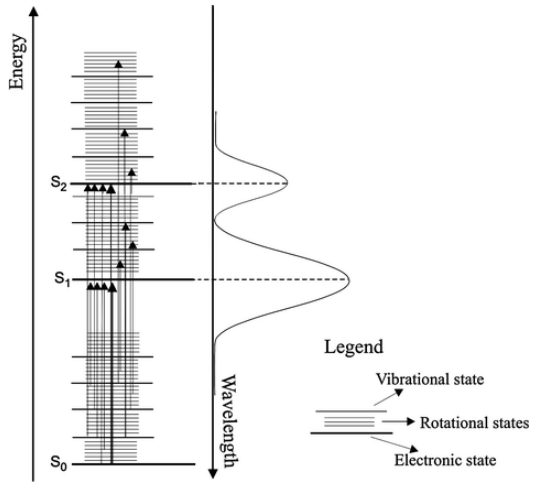

Figure 5.1. Correlation between electronic transitions and absorption spectra in molecules. Reproduced with permission of © 2020 Springer Nature Switzerland AG.[200]

The probability of the absorption determines the intensity of the band. The excitation of a molecule changes the electronic distribution and provokes a dipole moment connected with the transition that is proportional to its probability. The transitions with higher probability that induce higher variations in the dipole moment allow a higher absorption of light. These are the so called *allowed* transitions in opposition to the ones with low probability that are named *forbidden* and they present lower intensity.[1,201,202]

When light travels through the sample, the transmitted radiation will differ from the incident one. The absorbed light is given by the difference between the intensity of the incident light (I_0) and the intensity of the transmitted radiation (I), is expressed in transmittance or in absorbance.

The absorption capacity of a molecule is governed by the Lambert-Beer law (5.1):

$$I = I_0 \cdot 10^{-\varepsilon bc} \tag{5.1}$$

where I is the intensity of transmitted light, I_0 is the intensity of the incident light, ε is the molar absorption coefficient (measured in $M^{-1}cm^{-1}$), b is the path length (cm) and c is the molar concentration of the sample.

Hence, the absorption spectrum of a molecule can be obtained by measuring the absorbance (A) at different wavelengths:

$$A = \log\left(\frac{I_0}{I}\right) = \varepsilon bc \tag{5.2}$$

ε is normally employed as an indicator of the absorption capacity of the molecule, referred to a specific wavelength of absorbed light.

The instrument that we need to measure the transmittance or absorbance of a sample is called spectrophotometer. We can highlight the following components:

- An electromagnetic source of radiation that emits with a constant intensity: it must be stable, long lasting and presents a low noise. Usually two lamps are employed: deuterium arc lamp for UV range and a tungsten filament-halogen lamp for VIS-NIR range.
- Monochromator to a select single wavelength of the incident light.
- Sample holder, usually called cuvette, composed by plastic, glass or quartz with a square section.
- The detector converts the light signal into an electric one: normally modern instruments count with photomultiplier tubes or photodiode detectors.

The Lamber-Beer law is obeyed perfectly only in diluted solutions, and the spectrophotometer is linear in a certain range of A values (usually 0-2). Besides, it is important to calibrate the instrument at 0% (when the incident beam does not reach the detector) and 100% transmittance (the measurement of the blank).

5.2. Emission and excitation spectra[203]

Emission and excitation spectra can be collected through a photoluminescence spectrometer (spectrofluorimeter) that have two optical channels: excitation and emission. The key components of the spectrofluorimeter include: light source, excitation monochromator, sample cell, emission monochromator, detector (photomultiplier), data collection and analysis system. Excitation light sources are usually lasers, LED and lamps. The monochromator can selectively transmit the incident or emitted light in a specific wavelength range. The sample cell is located between the two light channels, set at a 90º angle. The detector measures the intensity of the emitted light at different wavelengths. Finally, the signals are collected and analyzed by the software.

Emission

Emission spectra allow to derive information about the nature and energy of an emitting excited state. To obtain an emission spectrum, the sample is excited at a fixed wavelength (λ_{exc}) at which it is absorbing and by moving the emission monochromator, the intensity of the luminescence, that varies with the emission wavelength (λ_{em}), is measured.

If we record an emission spectrum of a substance by exciting it in its lowest excited single state S_1, the substance can emit from S_1, showing fluorescence emission and/or it can undergo intersystem crossing to T_1 and yield phosphorescence. Therefore, experimentally both fluorescence and phosphorescence spectra can be determined (the latter only in oxygen free solutions or rigid matrices in case of organic molecules). The emission bands always fall at lower energy with respect to the absorption bands (Figure 5.2).

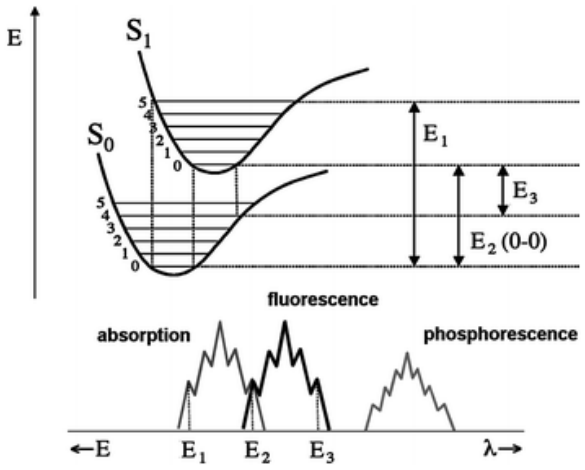

Figure 5.2. Potential energy curves for the ground and excited state of a generic molecule. Reproduced with permission of © 2020 Springer Nature Switzerland AG.[203]

Excitation Spectra

To record an excitation spectrum we need to fix the emission monochromator at a certain wavelength (λ_{em}), in correspondence of the emission band of the sample, while the wavelength selected by the excitation monochromator varies in the spectral interval in which the sample absorbs. The signal will be proportional to the probability that, once the photon is absorbed, the excited state responsible for the emission will be populated. The excitation spectrum is proportional to the absorption one (they present the same spectral shape) if only one luminescent species is present in solution and if the conversion from higher excited states to the one responsible for the emission occurs with unitary efficiency.

Corrections for the emission spectra

A raw emission spectrum requires a correction since the response of the optical and electrical components of the detection system is wavelength dependent. To obtain a correction curve, a calibrated lamp, which emission spectrum is known in details, provided by the manufacturer, is needed. The emission spectrum of the calibrated lamp obtained with the instrument is compared with that of the manufacturer. From this comparison it is possible to obtain a ratio at each wavelength (calibration curve) that has to be multiplied to the sample's raw spectrum to be corrected. It must be remarked that this ratio called correction curve includes the dependency on λ_{em} of both the response on the phototube and the transmission of the monochromator. The photomultiplier response varies with its use, so the correction curve needs be acquired with frequency in order to produce accurate emission spectra.

Determination of luminescence Quantum Yields

To determine if a molecule is a good luminophore, the emission quantum yield is the key parameter to be measured, defined by the following equation (5.3):

$$\phi = \frac{number\ of\ emitted\ photons}{number\ of\ absorbed\ photons} \tag{5.3}$$

In the comparative method, the quantum yield is determined by comparing the emission spectrum of the luminophore with that of a standard recorded under the same instrumental conditions. The comparison is based on the areas underneath the respective emission spectra measured from the baseline. If the same excitation wavelength is used, the unknow luminescence quantum yield can be obtained from the following formula (5.4):

$$\phi = \phi_R \frac{S}{S_R} \frac{A_R}{A} \frac{n^2}{n_R^2} \tag{5.4}$$

where ϕ is the emission quantum yield, S is the area underneath the spectrum for the whole emission wavelength range, A is the absorbance at the excitation wavelength and n is the refraction index of the solvent. The subscript R in the formula denotes the quantities referred to the standard with known quantum yield.

5.3. Time-resolved luminescence techniques[204]

A generic excited state *A can follow the three deactivation pahtways shown in Figure 5.3: (1) photochemical reaction, (2) radiationless deactivation and (3) radiative deactivation.

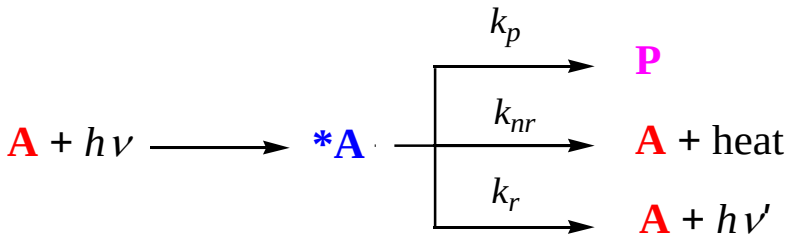

Figure 5.3. The generic excited species *A can decay following three main deactivation paths. Reproduced with permission of © 2020 Springer Nature Switzerland AG.[204]

The luminescence emitted in the radiative deactivation can be characterized by two different types of measurements. The usual one is to measure its intensity as a function of wavelength, obtaining an emission spectrum as explained before. The other way, which requires more sophisticated instrumentation, defines the temporal characteristics of the emission by measuring its intensity as a function of time.

The processes shown in Figure 5.3 are regulated by their monomolecular rate constant (k_p, k_r and k_{nr}). The three processes compete and the value of the constants determine the behavior of the excited state. If it is the case that the processes follow a first-order kinetics, the concentration of the excited state also decays following a first-order kinetics with a lifetime (τ) defined as in (5.5):

$$\tau = \frac{1}{\sum k} = \frac{1}{k_p + k_r + k_{nr}} \tag{5.5}$$

The lifetime τ is the time required to reduce the excited state concentration by and e factor. Simple kinetic treatment of (5.5) leads to the equations (5.6) and (5.7), where $[^*A]/[^*A]_0 = 1/e$ is obtained when $t = \tau$.

$$\frac{d[\,^*A]}{dt} = -(k_p + k_r + k_{nr})[\,^*A] = -\sum k[\,^*A] \tag{5.6}$$

$$[\,^*A] = [\,^*A]_0 \exp\left(-\sum k\, t\right) \tag{5.7}$$

Figure 5.4 represents in a graphical way the decay of the excited state concentration ruled by equation (5.7).

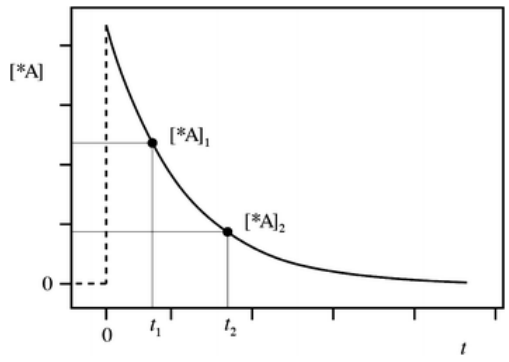

Figure 5.4. Variation of the concentration of the excited species **A* as a function of time. Following an ideally instantaneous excitation, **A* is formed at $t = 0$ (dashed line). Then, the concentration of **A* decays exponentially, in accordance with a first order kinetics (continuous line). After a lifetime $\tau = t_2 - t_1$ the excited state concentration is reduced by an *e* factor ($[*A]_2=[*A]_1/e$). Reproduced with permission of © 2020 Springer Nature Switzerland AG.[204]

Measuring the concentration of an excited sate as function of time leads to the calculation of its lifetime: the time-domain techniques are based on this kind of measurements. These techniques try to rebuild the decay curve by measuring the luminescence emission of the excited state as a function of time since at any time, a direct proportionality exists between the number of emitted photons and the number of excited states present. Hence, considering that $\sum k = 1/\tau$ from (5.5) and substituting the excited state concentration with the emission intensity, equation (5.7) can be rewritten as equation (5.8) or also as in equation (5.9) in logarithmic form:

$$I(t) = I_0 \exp(-t/\tau) \tag{5.8}$$

$$\ln I(t) = \ln I_0 - t/\tau \tag{5.9}$$

Equation (5.9) reveals that that a logarithmic plot of the decay intensity as a function of time give a straight line whose slope is $-1/\tau$.

These equations assume that the excited state decays follow a first-order kinetics. In more complex cases, multi-exponential or non-exponential decays are observed. The lifetimes values depend on temperature, so the latter must always be specified when giving lifetime values.

There are several techniques to measure the lifetime of an excited state using time-domain approaches. Herein, we explain the gated sampling, the streak camera acquisitions and the single photon counting technique, which are employed in this PhD thesis.

5.3.1. Experimental methods for lifetime measurements

Gated sampling[204]

This technique can be operated in a spectrofluorimeter by using a pulsed lamp and using a gated detection. It is based on the following: after the excitation pulse, the sample emission is measured after a delay time t_1 within a time window Δt (gate time) that needs to be short with respect to the sample lifetime. This type of acquisition is carried out by collecting and averaging the signal correspondent to many excitation pulses, thus the signal-to-noise ratio is minimized. In order to measure the lifetime, the measurement is repeated several times where the gate time Δt is shifted towards delay time values (t_2, t_3... t_n) that increase with respect to excitation. The decay curve is obtained by plotting the emission intensity values as a function of the delay time.

Measurements with a streak camera detector

This technique is used in Chapter 2 and 3 for measuring lifetimes in the ps-ns range, for this, femtosecond laser as excitation source is used. As a detector, a streak camera is used, whose description is explained below:

The streak camera device measures the temporal evolution of the intensity of optical pulses. The basic principle is that the incident light generates a spot that is deflected during some short time interval. The moving spot creates a spatial distribution (streak image) reflecting the temporal evolution of the optical power. The most common streak camera is an optoelectronic device where the incident light hits a photocathode placed in a vacuum tube. A high voltage applied in the cathode emits electrons that form a pulsed beam which intensity is linearly dependent on the optical intensity. The beam is deflected by a pair of electrodes and finally, it hits a phosphor screen for generating a visible streak image. Besides, the beam can hit a charge-coupled device (CCD) to generate an electronic signal.[205] From a streak image, both spectral and temporal information on the emitted light can be acquired.

Single Photon Counting[204]

The time correlated single photon counting technique is based on the probability that one "*single*" photon emitted by a luminescent sample could be detected by a highly sensitive photomultiplier. This probability is statistically related with the change in the concentration of the emitting excited state with time by a specific operative procedure.

The parts of a time correlated single photon counting (TCSPC) apparatus are shown in Figure 5.5. It is formed by a pulse light source connected to a light detector (start

photomultiplier: start PMT), an optional (exciting) monochromator, a sample holder, another optional (emitting) monochromator, a second light detector (stop PMT) and an electronic system for the treatment of the photomultiplier's signals. It is similar to an usual instrument for luminescence detection but it differs from:

i. the properties of the exciting light source
ii. the presence of the start PMT
iii. the properties of the stop PMT
iv. an unusual treatment of the PMT signals made by the electronic system.

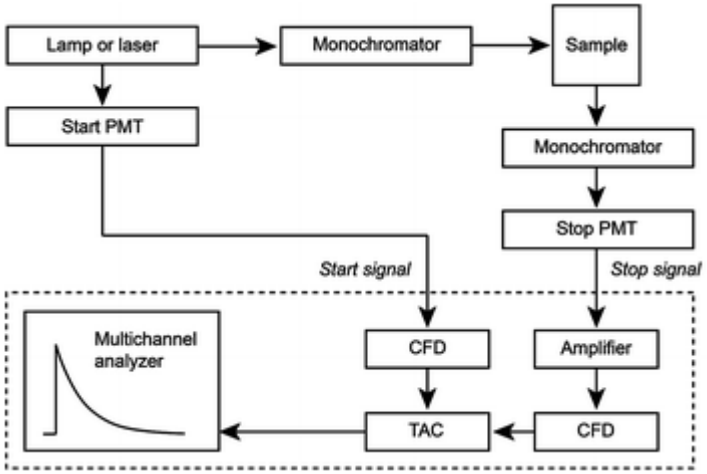

Figure 5.5. Schematic block diagram of a TCSPC counting apparatus. Reproduced with permission of © 2020 Springer Nature Switzerland AG.[204]

The exciting light source is usually a low-pressure lamp that produces light pulses with high repetition rate (frequency 1-100 kHz), short duration (1-5 ns), very low intensity and high stability. Nowadays, small lasers or LEDs are employed with shorter pulse duration.

The star PMT displays electric signals (pulses) having the same frequency of the light source with which it is optically connected. Each pulse starts a time cycle whose duration is selected before and is comprised within two consecutive pulses. The optimum time cycle duration is approximately 5-6 times the emission lifetime of the sample.

The stop PMT displays a pulse when hit by the first photon emitted by the sample, this pulse stops the time cycle initiated by the start signal, then the detector stops until a subsequent start signal begins a new excitation-emission cycle.

The final electronic system (dashed line in Figure 5.5) is formed by two constant fraction discriminators (CFD), a time-to-amplitude-converter (TAC) and a multichannel analyzer (MCA). The two CFD hamper the cycle when one of the two signals do not

reach a threshold value (this reduces dark current effects). The TAC works as a stopwatch by elaborating the signals coming from the start and stop photomultipliers. The TAC measures, within a single excitation-emission cycle, the time difference (Δt at ns scale) between the stop and the start signals. Meaning, the delay between the exciting photons (start signals) and the single photon causing the stop signal. In the end, MCA collects all the time delays from TAC organizing them in a plot showing the number of times that a single photon is seen by the stop PMT at a given Δt.

The apparatus functions as described here:

The lamp emits a light pulse, the start PMT sends an electric signal to the TAC where it starts a time cycle of a selected duration by generating an electric potential which increases linearly with time (Figure 5.6). The electric potential increase can be stopped by two events:

i. the end of the selected time cycle
ii. an electric signal from the stop PMT

In the case of (i) nothing else happens, whereas in the (ii) situation the TAC sends a signal to the MCA that records it as an event occurring at a time defined by the electric voltage at which the TAC has been stopped. Then the TAC, in both cases, is reset to wait for a new start signal beginning another time delay measurement. This procedure is repeated several times and allows the accumulation of a huge number of points in a plot showing the number of emitted photons versus time delay.

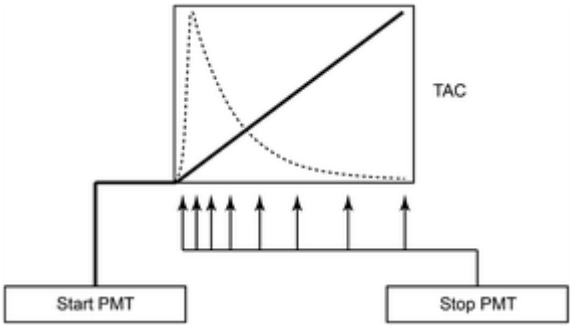

Figure 5.6. Working principle of the time-to-amplitude-converter. Reproduced with permission of © 2020 Springer Nature Switzerland AG.[204]

This technique provides accurate emission decay curves, so the analysis of multiple decays is possible, and it allows the so-called "*deconvolution*", meaning, lifetime measurements in a time range lower than that of the duration of the excitation pulse which

is usually the resolution limit for lifetimes measurements apparatus. When the emission processes occur in a time shorter than or similar to the excitation time, the exciting flash light becomes the determining step of the excitation-emission process and the excitation time width strongly affects the emission lifetime.

The *deconvolution* is a calculation technique that deconvolves the contribution of the exciting light flash from the emission decay curve leaving the pure emission behavior which allows the calculation of the actual emission lifetime. To apply this process, it is needed the time profile of the flash light (Figure 5.7).

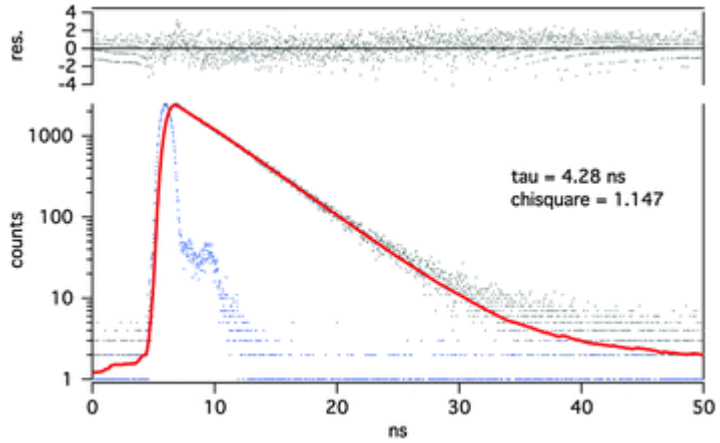

Figure 5.7. Emission lifetime determination by "*deconvolution*" of a fluorescein aqueous solution at pH = 7 at room temperature. The emission is collected at 525 nm. The observed emission decay is gray, the time behavior of the excitation of the laser flash is blue, and the fitting function is red. Reproduced with permission of © 2020 Springer Nature Switzerland AG.[204]

Summarizing, the TCSPC technique allows the measurement of the luminescence emission lifetimes in a temporal range from hundreds of picosecond to tens of microseconds. Short lifetimes are accessible by using deconvolution whereas long lifetimes are measurable by a suitable reduction of the excitation lamp frequency to avoid the presence of two or more excitation pulses within the selected excitation-emission time cycle.[206]

5.4. Transient absorption spectroscopy[207]

The transient absorption method is one of the most useful tools in photophysics and photochemistry. The fundament is to use an intense light pulse with a short time duration to perturb the equilibrium of a system and follow the appearance and the evolution of photochemically formed transients by detecting their electronic absorption.

A ground state molecule, when absorbing a photon, promotes itself to an excited state; from this higher energy state, the molecule can relax back to the ground state through some other intermediate excited state of single or triplet multiplicity or chemically react to form other products. Usually, these intermediates can be observed by detecting their absorption spectra in suitable wavelength windows in the UV-Vis-NIR. Flash photolysis systems with nanosecond resolution permit the detection of triplet states, diradicals and radicals, ions and bimolecular processes controlled by diffusion in solution. Besides, with transient absorption measurements with femtosecond resolution (pump and probe), excited singlet states and unimolecular processes like internal conversion, intersystem crossing, bond dissociation, and proton transfer, charge and energy transfer in singlet or multicomponent systems can be elucidated.

Herein, related with the work done in this PhD thesis, the technique that deals with the femtosecond range will be explained.

5.4.1. Ultrafast transient absorption spectroscopy[207]

Femtochemistry

Is the branch of the physical chemistry that studies phenomena in time intervals in the order of 10^{-12} to 10^{-15} s. It has allowed the detection of the transition state and reaction intermediates for formation-dissociation bonds, and intramolecular electron and proton transfer reactions.

Pump and Probe experiments

“Pump and probe” is a special detection technique used in systems for femto-picosecond transient spectroscopy. It is based on using the same laser source to generate the excitation pulse (pump) and the analysis beam (probe). The path of the probe beam is varied in length by a delay line. The change in the optical path allows the control of the temporal distance between excitation and analysis (Figure 5.8).

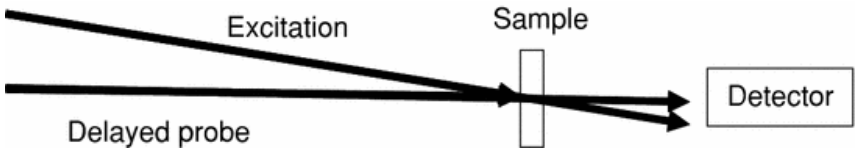

Figure 5.8. Pump beam and analysis beam are overlapped on the sample. Reproduced with permission of © 2020 Springer Nature Switzerland AG.[207]

Figure 5.9 shows the schematic layout of an apparatus to measure the femto-picosecond transient absorption spectra. A Ti:Sapphire femtosecond laser is used as light source. This system comprises a seed laser (modelocked Ti:Sapphire pulsed laser), a pump laser (Q-switched Nd:YFL laser), a stretcher, a Ti:sapphire regenerative amplifier and a compressor. The output is split (usually 50%) into two beams. One, the pump, is converted to the excitation wavelengths by coupling it into a second-harmonic (SHG) or into an optical parametric amplifier (TOPAS in our case, for tunable wavelengths in the region 280-2600 nm). The other beam, the probe, is passed through a computer controlled delay line, and then focused on a crystal plate (usually a sapphire or CaF_2 crystal) in order to generate a white light continuum (WLG, useful range, 450-750 nm sapphire, 350-750 nm CaF_2). The pump beam is passed through a computer controlled optical chopper, and focused on the sample cell. The white light continuum probe beam is collimated and focused into the sample cell, superimposed to the pump beam at an angle of 5º. To minimize the temporal chirp in the spectrum, parabolic mirrors are used to collimate and focus the white light probe beam. After passing through the sample cell, the white continuum is coupled into a 100 µm optical fiber connected to a CCD spectrograph.

With 100-fs pump and probe pulses, the effective time resolution of the ultrafast spectrometer, that is, the rise time of an instantaneous signal is *ca*. 300 fs. The maximum temporal window of the experiment, limited by the optical delay stage dimension, usually ranges from 0–1,000 ps to 0–4,000 ps, in our system is 0-7,000 ps.

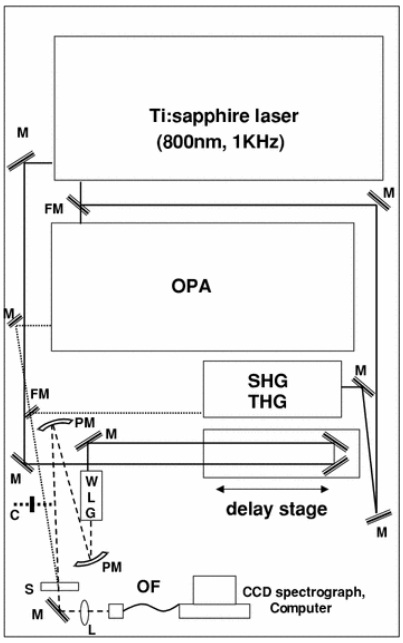

Figure 5.9. Schematic layout of an ultrafast spectroscopy setup. Continuous line, fundamental (800 nm); dashed line white light continuum probe; dotted line pump beam; M mirror; PM parabolic mirror; L lens; OF optical fiber; S sample; C chopper; FM flipping mirror; OPA optical parametric amplifier; WLG white light generator, SHG–THG second harmonic and third harmonic generators. Reproduced with permission of © 2020 Springer Nature Switzerland AG.[207]

Conclusions

In this PhD thesis, several supramolecular systems have been studied from a photophysical point of view. In Chapters 2 and 3, the study of four flexible covalent cages based on porphyrins was carried out. In the monometallated cages, an energy transfer process that sensitizes the free-base emission was found. Their flexibility has been proven for most of them upon addition of Ag(I). Furthermore, their ability to function as guest has been tested for the inclusion of the ethionamide molecule. Eventually, Chapter 4 deals with the photophysical study of acridinium-porphyrin conjugates, from where we can conclude that acridinium units, when linked to porphyrins, induce interesting properties into the arrays. Indeed, it was found that the fluorescence quenching observed in the array was due to an ultrafast photoinduced electron transfer process.

The study of the photophysical properties of different supramolecular systems is of interest since it opens the way to understand their functioning and applications, hence, helping us to comprehend natural processes in which photo-process are involved as well as to better design devices where these properties can play a major role. The cages studied in Chapters 2 and 3 can find application in host-guest systems that can act as molecular recognition or drug delivery systems where the signals can be transduced by spectroscopic changes. Besides, the conjugates presented in Chapter 4 can be used in photodynamic therapy to treat cancer cells, a field where the understanding of photophysics of the photosensitizers is of higher importance for its development.

Ultimately, the exploration of new supramolecular structures that possess interesting photophysical properties is worthwhile to the development of new smart devices with applications than can improve our life’s quality.

Notes

* Laboratoire de Synthèse des Assemblages Moléculaires Multifonctionnels, Institut de Chimie de Strasbourg, CNRS/UMR 7177, Université de Strasbourg, 4, Rue Blaise Pascal, 67000 Strasbourg, France.

** Department of Physical and Chemical Sciences, University of L'Aquila, Via Vetoio (Coppito 1), 67010 L'Aquila, Italy. / CNR Institute of Nanoscience, Via Campi 213/A, 41125 Modena, Italy.

References

[1] N. J. Turro, V. Ramamurthy, J. C. Scaiano, *Photochem. Photobiol.* **2012**, *88*, 1033–1033.

[2] P. Klán, J. Wirz, *Photochemistry of Organic Compounds*, Wiley, New York, **2009**.

[3] N. Armaroli, V. Balzani, *Energy for a Sustainable World from the Oil Age to a Sun-Powered Future*, Wiley-VCH, Weinheim Ch. 11, **2011**.

[4] L. Hammarstrom, S. Hammes-Schiffer, *Acc. Chem. Res.* **2009**, *42*, 1859–1860.

[5] P. Ceroni, V. Balzani, in *Explor. Supramol. Syst. Nanostructures by Photochem. Tech.* (Ed.: P. Ceroni), Springer Netherlands, Dordrecht, **2012**, pp. 1–20.

[6] P. Atkins, J. de Paula, *Atkins Physical Chemistry*, Oxford Universtiy Press, Oxford, **2009**.

[7] F. Cotton, *Chemical Applications of Group Theory*, John Wiely & Sons, Chichester, **1990**.

[8] M. Kasha, *Faraday Soc Discuss* **1950**, *9*, 14–19.

[9] E. Mattia, S. Otto, *Nat. Nanotechnol.* **2015**, *10*, 111–119.

[10] J. M. Lehn, *Angew. Chemie-International Ed.* **2013**, *52*, 2836–2850.

[11] M. W. Ambrogio, C. R. Thomas, Y. L. Zhao, J. I. Zink, J. F. Stoddartt, *Acc. Chem. Res.* **2011**, *44*, 903–913.

[12] B. L. Feringa, *Angew. Chemie - Int. Ed.* **2017**, *56*, 11060–11078.

[13] L. van Dijk, M. J. Tilby, R. Szpera, O. A. Smith, H. A. P. Bunce, S. P. Fletcher, *Nat. Rev. Chem.* **2018**, *2*, DOI 10.1038/s41570-018-0117.

[14] A. P. De Silva, N. D. McClenaghan, *Chem. - A Eur. J.* **2004**, *10*, 574–586.

[15] O. J. G. M. Goor, S. I. S. Hendrikse, P. Y. W. Dankers, E. W. Meijer, *Chem. Soc. Rev.* **2017**, *46*, 6621–6637.

[16] R. Chakrabarty, P. S. Mukherjee, P. J. Stang, *Chem. Rev.* **2011**, *111*, 6810–6918.

[17] P. Ceroni, V. Balzani, in *Explor. Supramol. Syst. Nanostructures by Photochem. Tech. Lect. Chem. Vol 78.* (Ed.: P. Ceroni), Springer, Dordrecht, **2012**, pp. 21–38.

[18] V. Balzani, M. Venturi, A. Credi, *Molecular Devices and Machines*, **2008**.

[19] R. Marcus, *Annu. Rev. Phys. Chem.* **1964**, *15*, 155–196.

[20] F. Scandola, C. Chiorboli, M. Indelli, M. Rampi, in *Balzani V Electron Transf. Chem. Vol 3*, **2001**, p. 337.

[21] V. Balzani, M. T. Indelli, M. Maestri, D. Sandrini, F. Scandola, *J. Phys. Chem.* **1980**, *84*, 852–855.

[22] F. Barigelletti, L. Flamigni, *Chem. Soc. Rev.* **2000**, *29*, 1–12.

[23] G. D. Scholes, *Annu. Rev. Phys. Chem.* **2003**, *54*, 57–87.

[24] G. Stochel, M. Brindell, W. Macyk, Z. Stasika, K. Szacilowski, *Bioinorganic Photochemistry*, Wiley, Chichester, **2009**.

[25] A. Barbieri, B. Ventura, R. Ziessel, *Coord. Chem. Rev.* **2012**, *256*, 1732–1741.

[26] J. M. Park, K. I. Hong, H. Lee, W. D. Jang, *Acc. Chem. Res.* **2021**, *54*, 2249–2260.

[27] S. Jansson, *BBA - Bioenerg.* **1994**, *1184*, 1–19.

[28] V. Balzani, A. Credi, M. Venturi, *ChemSusChem* **2008**, *1*, 26–58.

[29] J. T. Groves, Y. Watanabe, *J. Am. Chem. Soc.* **1988**, *110*, 8443–8452.

[30] D. P. Rillema, J. K. Nagle, L. F. Barringer, T. J. Meyer, *J. Am. Chem. Soc.* **1981**, *103*, 56–62.

[31] S. Fukuzumi, Y. M. Lee, W. Nam, *J. Porphyr. Phthalocyanines* **2020**, *24*, 21–32.

[32] A. Tovmasyan, T. Weitner, H. Sheng, M. Lu, Z. Rajic, D. S. Warner, I. Spasojevic, J. S. Reboucas, L. Benov, I. Batinic-Haberle, *Inorg. Chem.* **2013**, *52*, 5677–5691.

[33] J. Min Park, J. H. Lee, W.-D. Jang, *Coord. Chem. Rev.* **2020**, *407*, 213157.

[34] I. Beletskaya, V. S. Tyurin, A. Y. Tsivadze, R. Guilard, C. Stern, *Chem. Rev.* **2009**, *109*, 1659–1713.

[35] H. Lee, K. I. Hong, W. D. Jang, *Coord. Chem. Rev.* **2018**, *354*, 46–73.

[36] R. van der Weegen, A. J. P. Teunissen, E. W. Meijer, *Chem. – A Eur. J.* **2017**, *23*, 3773–3783.

[37] C. M. Drain, J. T. Hupp, K. S. Suslick, M. R. Wasielewski, X. Chen, *J. Porphyr. Phthalocyanines* **2002**, *6*, 243–258.

[38] Y. Sun, C. Chen, J. Liu, L. Liu, W. Tuo, H. Zhu, S. Lu, X. Li, P. J. Stang, *J. Am. Chem. Soc.* **2020**, *142*, 17903–17907.

[39] S. Ogi, K. Sugiyasu, S. Manna, S. Samitsu, M. Takeuchi, *Nat. Chem.* **2014**, *6*, 188–195.

[40] R. Giovannetti, in *Macro To Nano Spectrosc.* (Ed.: J. Uddin), IntechOpen, Rijeka, **2012**.

[41] J. Mendez-Arroyo, J. Barroso-Flores, A. M. Lifschitz, A. A. Sarjeant, C. L. Stern, C. A. Mirkin, *J. Am. Chem. Soc.* **2014**, *136*, 10340–10348.

[42] J. Li, D. Yim, W.-D. Jang, J. Yoon, *Chem. Soc. Rev.* **2017**, *46*, 2437–2458.

[43] M. Nappa, J. S. Valentine, *J. Am. Chem. Soc.* **1978**, *100*, 5075–5080.

[44] C.-H. Lee, S. Lee, H. Yoon, W.-D. Jang, *Chem. – A Eur. J.* **2011**, *17*, 13898–13903.

[45] C.-H. Lee, H. Yoon, W.-D. Jang, *Chem. – A Eur. J.* **2009**, *15*, 9972–9976.

[46] V. Valderrey, G. Aragay, P. Ballester, *Coord. Chem. Rev.* **2014**, *258–259*, 137–156.

[47] G. McDermott, S. M. Prince, A. A. Freer, A. M. Hawthornthwaite-Lawless, M. Z. Papiz, R. J. Cogdell, N. W. Isaacs, *Nature* **1995**, *374*, 517–521.

[48] J. M. Olson, *Photochem. Photobiol.* **1998**, *67*, 61–75.

[49] R. A. Haycock, A. Yartsev, U. Michelsen, V. Sundstrom, C. Hunter, *Angew. Chemie - Int. Ed.* **2000**, *39*, 3616–3619.

[50] Z. Y. Gu, D. S. Guo, M. Sun, Y. Liu, *J. Org. Chem.* **2010**, *75*, 3600–3607.

[51] W. D. Jang, C. H. Lee, M. S. Choi, M. Osada, *J. Porphyr. Phthalocyanines* **2009**, *13*, 787–793.

[52] Y. H. Jeong, M. Son, H. Yoon, P. Kim, D. H. Lee, D. Kim, W. D. Jang, *Angew. Chemie - Int. Ed.* **2014**, *53*, 6925–6928.

[53] M. Grätzel, *Nature* **2001**, *414*, 338–344.

[54] P. Gao, Z. Yang, J. He, J. Yu, P. Liu, J. Zhu, Z. Ge, J. Ye, *Adv. Sci.* **2018**, *5*, 1700547.

[55] J. Haschke, O. Dupré, M. Boccard, C. Ballif, *Sol. Energy Mater. Sol. Cells* **2018**, *187*, 140–153.

[56] A. Mahmood, J.-Y. Hu, B. Xiao, A. Tang, X. Wang, E. Zhou, *J. Mater. Chem. A* **2018**, *6*, 16769–16797.

[57] W. Zhang, W. Lai, R. Cao, *Chem. Rev.* **2017**, *117*, 3717–3797.

[58] X. Zhou, W. Tang, P. Bi, L. Yan, X. Wang, W.-K. Wong, X. Hao, B. S. Ong, X. Zhu, *J. Mater. Chem. A* **2018**, *6*, 14675–14680.

[59] T. Hasobe, P. V Kamat, M. A. Absalom, Y. Kashiwagi, J. Sly, M. J. Crossley, K. Hosomizu, H. Imahori, S. Fukuzumi, *J. Phys. Chem. B* **2004**, *108*, 12865–12872.

[60] S. S. Lucky, K. C. Soo, Y. Zhang, *Chem. Rev.* **2015**, *115*, 1990–2042.

[61] H. Zhu, H. Wang, B. Shi, L. Shangguan, W. Tong, G. Yu, Z. Mao, F. Huang, *Nat. Commun.* **2019**, *10*, 2412.

[62] W. Fan, P. Huang, X. Chen, *Chem. Soc. Rev.* **2016**, *45*, 6488–6519.

[63] Z. Zhou, J. Song, L. Nie, X. Chen, *Chem. Soc. Rev.* **2016**, *45*, 6597–6626.

[64] S. Xu, X. Zhu, C. Zhang, W. Huang, Y. Zhou, D. Yan, *Nat. Commun.* **2018**, *9*, 2053.

[65] J. Králová, Z. Kejík, T. Bříza, P. Poučková, A. Král, P. Martásek, V. Král, *J. Med. Chem.* **2010**, *53*, 128–138.

[66] M. Vinodh, F. H. Alipour, A. A. Mohamod, T. F. Al-Azemi, *Molecules* **2012**, *17*, 11763–11799.

[67] R. Ideta, F. Tasaka, W.-D. Jang, N. Nishiyama, G.-D. Zhang, A. Harada, Y. Yanagi, Y. Tamaki, T. Aida, K. Kataoka, *Nano Lett.* **2005**, *5*, 2426–2431.

[68] S. Durot, J. Taesch, V. Heitz, *Chem. Rev.* **2014**, *114*, 8542–8578.

[69] R. D. Mukhopadhyay, Y. Kim, J. Koo, K. Kim, *Acc. Chem. Res.* **2018**, *51*, 2730–2738.

[70] J. P. Collin, A. Harriman, V. Heitz, F. Odobel, J. P. Sauvage, *Coord. Chem. Rev.* **1996**, *148*, 63–69.

[71] D. Gust, T. A. Moore, A. L. Moore, *Acc. Chem. Res.* **2001**, *34*, 40–48.

[72] Y. Nakamura, N. Aratani, A. Osuka, *Chem. Soc. Rev.* **2007**, *36*, 831–845.

[73] A. Satake, Y. Kobuke, *Org. Biomol. Chem.* **2007**, *5*, 1679–1691.

[74] N. Aratani, D. Kim, A. Osuka, *Acc. Chem. Res.* **2009**, *42*, 1922–1934.

[75] J. A. Faiz, V. Heitz, J. P. Sauvage, *Chem. Soc. Rev.* **2009**, *38*, 422–442.

[76] D. Gust, T. A. Moore, A. L. Moore, *Acc. Chem. Res.* **2009**, *42*, 1890–1898.

[77] M. R. Wasielewski, *Acc. Chem. Res.* **2009**, *42*, 1910–1921.

[78] A. Takai, M. Chkounda, A. Eggenspiller, C. P. Gros, M. Lachkar, J. M. Barbe, S. Fukuzumi, *J. Am. Chem. Soc.* **2010**, *132*, 4477–4489.

[79] F. L. Jiang, D. Fortin, P. D. Harvey, *Inorg. Chem.* **2010**, *49*, 2614–2623.

[80] Y. Pellegrin, F. Odobel, *Coord. Chem. Rev.* **2011**, *255*, 2578–2593.

[81] H. Imahori, T. Umeyama, K. Kurotobi, Y. Takano, *Chem. Commun.* **2012**, *48*, 4032–4045.

[82] D. M. Guldi, *Chem. Soc. Rev.* **2002**, *31*, 22–36.

[83] M. Beyler, L. Flamigni, V. Heitz, J. P. Sauvage, B. Ventura, *Photochem. Photobiol.* **2014**, *90*, 275–286.

[84] N. Aratani, A. Osuka, H. S. Cho, D. Kim, *J. Photochem. Photobiol. C Photochem. Rev.* **2002**, *3*, 25–52.

[85] D. Kim, A. Osuka, *J. Phys. Chem. A* **2003**, *107*, 8791–8816.

[86] D. Kim, A. Osuka, *Acc. Chem. Res.* **2004**, *37*, 735–745.

[87] M. S. Choi, T. Yamazaki, I. Yamazaki, T. Aida, *Angew. Chemie - Int. Ed.* **2003**, *43*, 150–158.

[88] T. S. Balaban, *Acc. Chem. Res.* **2005**, *38*, 612–623.

[89] L. Flamigni, V. Heitz, J. P. Sauvage, *Struct. Bond.* **2006**, *121*, 217–261.

[90] G. Kodis, Y. Terazono, P. A. Liddell, J. Andréasson, V. Garg, M. Hambourger, T.

A. Moore, A. L. Moore, D. Gust, *J. Am. Chem. Soc.* **2006**, *128*, 1818–1827.

[91] W. S. Li, K. S. Kim, D. L. Jiang, H. Tanaka, T. Kawai, J. H. Kwon, D. Kim, T. Aida, *J. Am. Chem. Soc.* **2006**, *128*, 10527–10532.

[92] M. Kuroki, T. Aida, S. Inoue, *J. Am. Chem. Soc.* **1987**, *109*, 4737–4738.

[93] J. P. Collman, X. M. Zhang, V. J. Lee, E. S. Uffelman, J. I. Brauman, *Science (80-.).* **1993**, *261*, 1404–1411.

[94] K. M. Kadish, K. M. Smith, R. Guilard, *The Porphyrin Handbook*, Academic Press, San Diego, **2012**.

[95] M. C. Feiters, A. E. Rowan, R. J. M. Nolte, *Chem. Soc. Rev.* **2000**, *29*, 375–384.

[96] J. P. Collman, N. K. Devaraj, R. A. Decréau, Y. Yang, Y. L. Yan, W. Ebina, T. A. Eberspacher, C. E. D. Chidsey, *Science (80-.).* **2007**, *315*, 1565–1568.

[97] C. M. Che, V. K. Y. Lo, C. Y. Zhou, J. S. Huang, *Chem. Soc. Rev.* **2011**, *40*, 1950–1975.

[98] D. Intrieri, A. Caselli, E. Gallo, *Eur. J. Inorg. Chem.* **2011**, 5071–5081.

[99] A. Takai, B. Habermeyer, S. Fukuzumi, *Chem. Commun.* **2011**, *47*, 6804–6806.

[100] V. Pradines, G. Pratviel, *Angew. Chemie - Int. Ed.* **2013**, *52*, 2185–2188.

[101] W.-P. To, Y. Liu, T.-C. Lau, C.-M. Che, *Chem. - A Eur. J.* **2013**, *19*, 5654–5664.

[102] Elemans, Bijsterveld, Rowan, Nolte, *Chem. Commun.* **2000**, 2443–2444.

[103] J. F. Lovell, T. W. B. Liu, J. Chen, G. Zheng, *Chem. Rev.* **2010**, *110*, 2839–2857.

[104] M. Ethirajan, Y. Chen, P. Joshi, R. K. Pandey, *Chem. Soc. Rev.* **2011**, *40*, 340–362.

[105] C. M. Lemon, P. J. Brothers, B. Boitrel, *Dalt. Trans.* **2011**, *40*, 6591–6609.

[106] B. Therrien, *Chem. - A Eur. J.* **2013**, *19*, 8378–8386.

[107] L. Grill, M. Dyer, L. Lafferentz, M. Persson, M. V. Peters, S. Hecht, *Nat. Nanotechnol.* **2007**, *2*, 687–691.

[108] M. Koepf, J. A. Wytko, J. P. Bucher, J. Weiss, *J. Am. Chem. Soc.* **2008**, *130*, 9994–10001.

[109] C. M. Drain, A. Varotto, I. Radivojevic, *Chem. Rev.* **2009**, *109*, 1630–1658.

[110] S. Mohnani, D. Bonifazi, *Coord. Chem. Rev.* **2010**, *254*, 2342–2362.

[111] J. Otsuki, *Coord. Chem. Rev.* **2010**, *254*, 2311–2341.

[112] D. Heim, D. Écija, K. Seufert, W. Auwärter, C. Aurisicchio, C. Fabbro, D. Bonifazi, J. V. Barth, *J. Am. Chem. Soc.* **2010**, *132*, 6783–6790.

[113] D. Écija, W. Auwärter, S. Vijayaraghavan, K. Seufert, F. Bischoff, K. Tashiro, J. V. Barth, *Angew. Chemie - Int. Ed.* **2011**, *50*, 3872–3877.

[114] M. Koepf, F. Chérioux, J. A. Wytko, J. Weiss, *Coord. Chem. Rev.* **2012**, *256*, 2872–2892.

[115] C. Iacovita, S. Vijayaraghavan, T. A. Jung, P. Fesser, F. Diederich, M. Enache, M. Stoehr, *Chem. - A Eur. J.* **2012**, *18*, 14610-14613,4.

[116] J. K. Sprafke, D. V Kondratuk, M. Wykes, A. L. Thompson, M. Hoffmann, R. Drevinskas, W. H. Chen, C. K. Yong, J. Karnbratt, J. E. Bullock, M. Malfois, M. R. Wasielewski, B. Albinsson, L. M. Herz, D. Zigmantas, D. Beljonne, H. L. Anderson, *J. Am. Chem. Soc.* **2011**, *133*, 17262–17273.

[117] M. J. Griffith, K. Sunahara, P. Wagner, K. Wagner, G. G. Wallace, D. L. Officer, A. Furube, R. Katoh, S. Mori, A. J. Mozer, *Chem. Commun.* **2012**, *48*, 4145–4162.

[118] J. A. Wytko, R. Ruppert, C. Jeandon, J. Weiss, *Chem. Commun.* **2018**, *54*, 1550–1558.

[119] S. Hong, M. R. Rohman, J. Jia, Y. Kim, D. Moon, Y. H. Ko, E. Lee, K. Kim, *Angew. Chemie-International Ed.* **2015**, *54*, 13241–13244.

[120] C. Yu, H. Long, Y. H. Jin, W. Zhang, *Org. Lett.* **2016**, *18*, 2946–2949.

[121] I. W. Hwang, T. Kamada, T. K. Ahn, D. M. Ko, T. Nakamura, A. Tsuda, A. Osuka, D. Kim, *J. Am. Chem. Soc.* **2004**, *126*, 16187–16198.

[122] L. P. Hernández-Eguía, E. C. Escudero-Adán, I. C. Pintre, B. Ventura, L. Flamigni, P. Ballester, *Chem. - A Eur. J.* **2011**, *17*, 14564–14577.

[123] S. Durot, L. Flamigni, J. Taesch, T. T. Dang, V. Heitz, B. Ventura, *Chem. Eur. J.* **2014**, *20*, 9979–9990.

[124] P. D. Harvey, C. Stern, C. P. Gros, R. Guilard, *Coord. Chem. Rev.* **2007**, *251*, 401–428.

[125] D. Gust, T. A. Moore, A. L. Moore, *Acc. Chem. Res.* **2009**, *42*, 1890–1898.

[126] J. S. Lindsey, D. F. Bocian, *Acc. Chem. Res.* **2011**, *44*, 638–650.

[127] R. Huber, *Angew. Chemie-International Ed. English* **1989**, *28*, 848–869.

[128] J. Deisenhofer, H. Michel, *Angew. Chemie Int. Ed. English* **1989**, *28*, 829–847.

[129] J. Deisenhofer, O. Epp, I. Sinning, H. Michel, *J. Mol. Biol.* **1995**, *246*, 429–457.

[130] M. Z. Papiz, S. M. Prince, T. Howard, R. J. Cogdell, N. W. Isaacs, *J. Mol. Biol.* **2003**, *326*, 1523–1538.

[131] A. W. Roszak, T. D. Howard, J. Southall, A. T. Gardiner, C. J. Law, N. W. Isaacs, R. J. Cogdell, *Science (80-.).* **2003**, *302*, 1969–1972.

[132] Y. Umena, K. Kawakami, J. R. Shen, N. Kamiya, *Nature* **2011**, *473*, 55–60.

[133] J. Pšenčík, S. J. Butcher, R. Tuma, *Struct. Basis Biol. Energy Gener.* **2014**, *39*, 77–

109.

[134] L. Flamigni, B. Ventura, A. I. Oliva, P. Ballester, *Chem. - A Eur. J.* **2008**, *14*, 4214–4224.

[135] A. I. Oliva, B. Ventura, F. Wurthner, A. Camara-Campos, C. A. Hunter, P. Ballester, L. Flamigni, *Dalt. Trans.* **2009**, 4023–4037.

[136] M. Beyler, V. Heitz, J. P. Sauvage, B. Ventura, L. Flamigni, K. Rissanen, *Inorg. Chem.* **2009**, *48*, 8263–8270.

[137] B. Ventura, L. Flamigni, M. Beyler, V. Heitz, J. P. Sauvage, *Chem. - A Eur. J.* **2010**, *16*, 8748–8756.

[138] T. T. Dang, S. Durot, L. Monnereau, V. Heitz, A. Barbieri, B. Ventura, *Dalt. Trans.* **2017**, *46*, 9375–9381.

[139] L. Schoepff, L. Kocher, S. Durot, V. Heitz, *J. Org. Chem.* **2017**, *82*, 5845–5851.

[140] R. Djemili, L. Kocher, S. Durot, A. Peuronen, K. Rissanen, V. Heitz, *Chem. Eur. J.* **2019**, *25*, 1481–1487.

[141] L. Zanetti-Polzi, A. Amadei, R. Djemili, S. Durot, L. Schoepff, V. Heitz, B. Ventura, I. Daidone, *J. Phys. Chem. C* **2019**, *123*, 13094–13103.

[142] D. Sanchez-Resa, L. Schoepff, R. Djemili, S. Durot, V. Heitz, B. Ventura, *J. Porphyr. Phthalocyanines* **2019**, *23*, 841–849.

[143] L. Kocher, S. Durot, V. Heitz, *Chem. Commun.* **2015**, *51*, 13181–13184.

[144] T. Fransson, T. Saue, P. Norman, *J. Chem. Theory Comput.* **2016**, *12*, 2324–2334.

[145] B. Minaev, H. Agren, *Chem. Phys.* **2005**, *315*, 215–239.

[146] K. F. Wong, B. Bagchi, P. J. Rossky, *J. Phys. Chem. A* **2004**, *108*, 5752–5763.

[147] S. Faure, C. Stern, R. Guilard, P. D. Harvey, *J. Am. Chem. Soc.* **2004**, *126*, 1253–1261.

[148] H. Sun Cho, D. H. Jeong, M. C. Yoon, Y. H. Kim, Y. R. Kim, D. Kim, S. C. Jeoung, S. K. Kim, N. Aratani, H. Shinmori, A. Osuka, *J. Phys. Chem. A* **2001**, *105*, 4200–4210.

[149] P. G. Seybold, Gouterma.M, *J. Mol. Spectrosc.* **1969**, *31*, 1–9.

[150] A. Briš, P. Trošelj, D. Margetić, L. Flamigni, B. Ventura, *Chempluschem* **2016**, *81*, 985–994.

[151] T. Főrster, *Discuss. Faraday Soc.* **1959**, *27*, 7–17.

[152] B. W. Van Der Meer, G. Coker III, S. Y. Simon Chen, *In Resonance Energy Transfer: Theory and Data*, Weinheim, **1994**.

[153] T. Nakamura, H. Ube, M. Shionoya, *Angew. Chemie-International Ed.* **2013**, *52*,

12096–12100.

[154] J. M. Lehn, *Acc. Chem. Res.* **1978**, *11*, 49–57.

[155] S. Rieth, K. Hermann, B. Y. Wang, J. D. Badjic, *Chem. Soc. Rev.* **2011**, *40*, 1609–1622.

[156] T. Y. Kim, R. A. S. Vasdev, D. Preston, J. D. Crowley, *Chem. Eur. J.* **2018**, *24*, 14878–14890.

[157] M. Liu, X. Yan, M. Hu, X. Chen, M. Zhang, B. Zheng, X. Hu, S. Shao, F. Huang, *Org. Lett.* **2010**, *12*, 2558–2561.

[158] R. S. Stoll, S. Hecht, *Angew. Chemie - Int. Ed.* **2010**, *49*, 5054–5075.

[159] O. B. Berryman, A. C. Sather, A. Lledo, J. Rebek, *Angew. Chemie-International Ed.* **2011**, *50*, 9400–9403.

[160] E. Busseron, J. Lux, M. Degardin, J. Rebek, *Chem. Commun.* **2013**, *49*, 4842–4844.

[161] M. Han, R. Michel, B. He, Y. S. Chen, D. Stalke, M. John, G. H. Clever, *Angew. Chemie - Int. Ed.* **2013**, *52*, 1319–1323.

[162] N. Kishi, M. Akita, M. Kamiya, S. Hayashi, H. F. Hsu, M. Yoshizawa, *J. Am. Chem. Soc.* **2013**, *135*, 12976–12979.

[163] A. Diaz-Moscoso, F. A. Arroyave, P. Ballester, *Chem. Commun.* **2016**, *52*, 3046–3049.

[164] I. Pochorovski, F. Diederich, *Acc. Chem. Res.* **2014**, *47*, 2096–2105.

[165] S. Stojanovic, D. A. Turner, A. I. Share, A. H. Flood, C. M. Hadad, J. D. Badjic, *Chem. Commun.* **2012**, *48*, 4429–4431.

[166] V. Croue, S. Goeb, G. Szaloki, M. Allain, M. Salle, *Angew. Chemie-International Ed.* **2016**, *55*, 1746–1750.

[167] N. Branda, R. M. Grotzfeld, C. Valdes, J. Rebek, *J. Am. Chem. Soc.* **1995**, *117*, 85–88.

[168] S. Rieth, B. Y. Wang, X. G. Bao, J. D. Badjic, *Org. Lett.* **2009**, *11*, 2495–2498.

[169] N. Kishi, M. Akita, M. Yoshizawa, *Angew. Chemie-International Ed.* **2014**, *53*, 3604–3607.

[170] S. Loffler, J. Lubben, L. Krause, D. Stalke, B. Dittrich, G. H. Clever, *J. Am. Chem. Soc.* **2015**, *137*, 1060–1063.

[171] D. Preston, A. Fox-Charles, W. K. C. Lo, J. D. Crowley, *Chem. Commun.* **2015**, *51*, 9042–9045.

[172] A. Peracchi, A. Mozzarelli, *Biochim. Biophys. Acta-Proteins Proteomics* **2011**,

1814, 922–933.

[173] P. Tompa, *Chem. Rev.* **2014**, *114*, 6715–6732.

[174] D. Ma, G. Hettiarachchi, D. Nguyen, B. Zhang, J. B. Wittenberg, P. Y. Zavalij, V. Briken, L. Isaacs, *Nat. Chem.* **2012**, *4*, 503–510.

[175] K. Bera, S. Maiti, M. Maity, C. Mandal, N. C. Maiti, *ACS Omega* **2018**, *3*, 4602–4619.

[176] L. Zanetti-Polzi, R. Djemili, S. Durot, V. Heitz, I. Daidone, B. Ventura, *Chem. Eur. J.* **2020**, *26*, 17514–17524.

[177] *NCIthesaurus*.

[178] ReactLab TM, E. 1. 1, Jplus Consulting Pty Ltd.

[179] K. M. Kadish, X. Q. Lin, J. Q. Ding, Y. T. Wu, C. Araullo, *Inorg. Chem.* **1986**, *25*, 3236–3242.

[180] O. Horváth, Z. Valicsek, G. Harrach, G. Lendvay, M. A. Fodor, *Coord. Chem. Rev.* **2012**, *256*, 1531–1545.

[181] K. Gleu, A. Schubert, *Ber. Dtsch. Chem. Ges. B* **1940**, 757–761.

[182] B. Singer, G. Maas, *Org. Chemie* **1984**, 1399–1408.

[183] H. P. J. de Rouville, J. Hu, V. Heitz, *Chempluschem* **2021**, *86*, 110–129.

[184] T. Mizutani, K. Wada, S. Kitagawa, *J. Am. Chem. Soc.* **2001**, *123*, 6459–6460.

[185] W. Kenji, T. Mizutani, M. Hideki, K. Susumu, *Chem. - A Eur. J.* **2003**, *9*, 2368–2380.

[186] D. Kim, S. Lee, G. Gao, H. Seok Kang, J. Ko, *J. Organomet. Chem.* **2010**, *695*, 111–119.

[187] A. Chaudhary, S. P. Rath, *Chem. - A Eur. J.* **2012**, *18*, 7404–7417.

[188] M. Tanaka, K. Ohkubo, C. P. Gros, R. Guilard, S. Fukuzumi, *J. Am. Chem. Soc.* **2006**, *128*, 14625–14633.

[189] H. Kotani, K. Ohkubo, M. J. Crossley, S. Fukuzumi, *J. Am. Chem. Soc.* **2011**, *133*, 11092–11095.

[190] A. Edo-Osagie, D. Sánchez-Resa, D. Serillon, E. Bandini, C. Gourlaouen, H. P. J. de Rouville, B. Ventura, V. Heitz, *Comptes Rendus Chim.* **2021**, *24*, DOI 10.5802/crchim.100.

[191] H. Van Willigen, G. Jones, M. S. Farahat, *J. Phys. Chem.* **1996**, *100*, 3312–3316.

[192] J. Fajer, D. C. Borg, A. Forman, D. Dolphin, R. H. Felton, *J. Am. Chem. Soc.* **1970**, *92*, 3451–3459.

[193] S. Fukuzumi, K. Ohkubo, T. Suenobu, K. Kato, M. Fujitsuka, O. Ito, *J. Am. Chem.*

Soc. **2001**, *123*, 8459–8467.

[194] K. Ohkubo, K. Suga, K. Morikawa, S. Fukuzumi, *J. Am. Chem. Soc.* **2003**, *125*, 12850–12859.

[195] M. Tanaka, K. Ohkubo, C. P. Gros, R. Guilard, S. Fukuzumi, *ECS Trans.* **2019**, *2*, 167–176.

[196] R. A. Marcus, *Angew. Chemie-International Ed. English* **1993**, *32*, 1111–1121.

[197] B. Ventura, L. Flamigni, G. Marconi, F. Lodato, D. L. Officer, *New J. Chem.* **2008**, *32*, 166–178.

[198] P. G. Seybold, M. Gouterman, *J. Mol. Spectrosc.* **1969**, *31*, 1–13.

[199] K. Rurack, M. Spieles, *Anal. Chem.* **2011**, *83*, 1232–1242.

[200] N. Zaccheroni, in *Explor. Supramol. Syst. Nanostructures by Photochem. Tech.* (Ed.: P. Ceroni), Springer Netherlands, Dordrecht, **2012**, pp. 39–66.

[201] P. Suppan, *Chemistry and Light*, Royal Soc Chem, Cambridge, **1994**.

[202] A. Gilbert, J. Baggot, *Essential of Molecular Photochemistry*, Blakwell, Oxford, **1991**.

[203] L. Prodi, A. Credi, in *Explor. Supramol. Syst. Nanostructures by Photochem. Tech.* (Ed.: P. Ceroni), Springer Netherlands, Dordrecht, **2012**, pp. 97–129.

[204] A. Juris, M. Maestri, in *Explor. Supramol. Syst. Nanostructures by Photochem. Tech.* (Ed.: P. Ceroni), Springer Netherlands, Dordrecht, **2012**, pp. 167–184.

[205] R. Paschotta, *Encyclopedia of Laser Physics and Technology*, Wile, Weinheim, Germany, **2008**.

[206] J. Lakowicz, *Principles of Fluorescence Spectroscopy*, Springer, New York, **2006**.

[207] S. Monti, C. Chiorboli, in *Explor. Supramol. Syst. Nanostructures by Photochem. Tech.* (Ed.: P. Ceroni), Springer Netherlands, Dordrecht, **2012**, pp. 185–207.

Acknowledgments

I would like to thank Dr. Barbara Ventura for your kind and very patient supervision and for allowing me to perform my PhD thesis at ISOF-CNR. As well to the rest of the members of PHEEL unit for the support and help in the different techniques: A. Barbieri, A. Venturini, E. Bandini, I. Manet, N. Armaroli and Francesco Manoli. To the funding of the H2020-MSCA-ITN-2017-765297 project "NOAH" and the rest of the consortium.

En particular, quiero agradecer a Filippo Monti por la ayuda en el laboratorio y las charlas.

Regarding the scientific work, I want to acknowledge Prof. Heitz's group and Ami Edo-Osagie for the synthesis of the different compounds studied in this thesis as well as Prof. Daidone's group for the computational work.

Muchas gracias a Santiago por el tiempo muerto y vivo desde que nos conocimos, por los paseos y las bajonas.

A Alba, con efecto presente y retroactivo, por todo. No sólo por el consuelo en el doctorado sino por lo afortunado que me siento de habernos encontrado en Ciudad Real, atrevernos con Tarragona y espero que algún sitio más en el futuro. No sé qué hubiera sido de mí sin compartir sueños y aspiraciones contigo. Muchísimas gracias por mantenerme a flote en las horas bajas, bajísimas, por reconocerme cuando yo no podía. Y por la diversión, siempre.

A mis amigas de Valdepeñas por permitirme volver siempre y hacerme sentir igual de bien en cada vuelta. A Miriam de la Torre Maroto, con todos los apellidos, por los interminables audios y su también interminable apoyo y comprensión.

Finalmente, a mi familia Sánchez Resa: María, Antonio y Ana por mantener una casa a la que llamar hogar y por no desistir nunca. Por el apoyo en todas las etapas y cambios, consejos y aprendizajes. Gracias a vosotros soy y me mantengo.